Structure of Grain Boundaries in Hexagonal Materials

Thesis submitted in accordance with the requirements of the University of Liverpool for the degree of Doctor in Philosophy by

Franck SARRAZIT

May 1998

ABSTRACT

The work presented in this thesis describes experimental and theoretical aspects associated with the structure of grain boundaries in hexagonal materials. It has been found useful to classify grain boundaries as low-angle, special or general on the basis of their structure. High-angle grain boundaries were investigated in tungsten carbide (WC) using conventional electron microscopy techniques, and three examples characteristic of the interfaces observed in this material were studied extensively. Three-dimensionally periodic patterns are proposed as plausible reference configurations, and the Burgers vectors of observed interfacial dislocations were predicted using a theory developed recently. The comparison of experimental observations with theoretical predictions proved to be difficult as contrast simulation techniques require further development for analysis to be completed confidently.

Another part of this work involves the characterisation of high-angle grain boundaries in zinc oxide (ZnO) using circuit mapping. Two boundaries displayed structural features characteristic of the "special" category, however, one boundary presented features which did not conform to this model. It is proposed that the latter observation shows a structural transition from the special to a more general type.

Material fluxes involved in defect interactions were considered using the topological framework described in this work. A general expression was derived for the total flux arising which allows the behaviour of line-defects to be studied in complex interfacial processes.

Cette thèse est dediée à mes parents

Table of Contents

PREFACE

This thesis describes research carried out in the Department of Materials Science and Engineering under the supervision of Professor R.C.Pond at The University of Liverpool between October 1994 and October 1997. The work is original and has not been submitted for a degree at any other university. Where necessary, the work of others has been freely drawn upon and duly referenced. A list of the references used can be found at the end of each chapter.

Some parts of the work described in this thesis have been published as follows:

"Diffusive Fluxes Associated with Interfacial Defect Motion and Interaction"

R.C.Pond and F.Sarrazit, *Interface Science*, Vol. **4**, Numbers 1, 2, p99 1996

"High-Resolution Electron Microscopy of ZnO Grain Boundaries in Bicrystals Obtained by the Solid Phase Intergrowth Process"

A.N. Kiselev, F.Sarrazit, E.A. Stepansov, E. Olsson, T.Claeson, V.I., Bondarenko, R.C. Pond and N.A. Kiselev, *Philosophical Magazine A*, Vol. **76**, N°3, p633-655 (1997)

"Structure Transition in a ZnO Grain boundary"

F.Sarrazit, R.C. Pond and N.A. Kiselev, *Philosophical Magazine Letters*, in press

"Grain Boundary Structure in Hexagonal Materials"

F.Sarrazit, I. MacLaren, M.Aindow and R.C. Pond, *Transactions of the Materials Society*, (D.A.Smith symposium) , 1998, in press.

ACKNOWLEDGMENTS

I would like to thank Professor R.C.Pond for his constant encouragement and invaluable guidance throughout this work. Thanks are also due to Dr M.Aindow and Dr. G.Nouet, from the Universities of Birmingham and Caen respectively, for providing the materials studied and for useful discussions. Dr I.MacLaren and Mr Wang (University of Birmingham) are also acknowledged for their interest in this project.

I would also like to thank all my friends at this University (Sue, Mark, Simon, Glyn, Tim, Dan, Hameed and others) for their friendship. Finally, I would like to thank Claire and my family for their love and constant encouragement during the last three years.

Chapter 1

Introduction

I.1 Introduction

It has long been recognised that the control of properties or improvement in performance can be achieved by controlling microstructure in materials. Grain boundaries are important elements of the microstructure of most engineering metallic and ceramic materials and are known to exert a profound influence on their properties. In some instances, it is the average response of the grain boundaries which determines the material's behaviour [1], however, in other cases, the overall performance is best described by the properties of individual grain boundaries [2]. With regards to performance, the presence of grain boundaries may have beneficial or detrimental effects on material properties. For example, grain boundaries may act as barriers to slip propagation at low temperature , yet their part in processes such as creep at high temperature [3], may lead to catastrophic failures. The understanding of the role played by grain boundaries is fundamental to the control of properties, and their study has been an exciting subject of research for over a century. It is now well accepted that a microscopic description of the boundary is useful to determine or predict macroscopic properties, and both theoretical and experimental advances have been made which have extended our knowledge of grain boundary structures. Early observations of grain boundaries using electron microscopy techniques revealed the presence of defects at grain boundaries, and it is now well established that their motion, multiplication or interaction for example, provide mechanisms for processes which affect properties dramatically. The motion of interfacial line-defects, for example, causes deformation of polycrystalline materials which may also involve a diffusional flux [4]. The latter can be described by an equation expressed in terms of the topological parameters which characterise the defects, namely their Burgers vectors and step heights, the defect velocity and the concentration of each atomic species in the two adjacent crystals [5]. This approach provides a framework for the study of the motion and interaction of individual defects in more complex interfacial processes [6].

Several models and descriptions of grain boundaries evolved over the years to account for experimental observations, and it was found useful to classify grain boundaries as low-angle, special or general on the basis of their structure [7]. In the following, the term special refers to boundaries with misorientations close to singular values and which are capable of sustaining localised line defects. Low angle grain boundaries can be described by arrays of crystal dislocations embedded in otherwise perfect crystal, whereas in the special category, interfaces may contain defects other than crystal dislocations. The latter type of grain boundary has been shown to exhibit distinct physical and chemical properties, especially in cubic materials. Some of the properties accounted for include lower energy [8], less susceptibility to impurity or solute segregation for example [9], [10]. The vast majority of grain boundaries, however, belong to the general class, and is by far the least understood due primarily to difficulties associated with observation of their structure. For example, high resolution microscopy techniques require the electron beam direction to be parallel to low-index directions in both crystals simultaneously and for the interface to be edge-on. This is usually incompatible with the crystallography of general grain boundaries.

The range of materials in which interfacial features have been investigated to date represents a small fraction of the total diversity, with the majority of the research having been carried out in materials belonging to the cubic class. The CSL and O-lattice models were found to be useful geometrical constructs for the identification of both reference orientations and dislocation arrangements, however, there is considerable evidence that their application to materials outside the cubic system is limited. Since non-cubic materials are being increasingly used in new applications, a more detailed knowledge of interfacial structures in these materials is therefore required.

I.2 Structure of this Thesis

The main objective of this work is to investigate the atomic structure of grain boundaries in material exhibiting hexagonal symmetry. The first part involved the identification of structural features in zinc oxide (ZnO) grain boundaries using a topological analysis developed by Pond [11], consistent with the topological theory of defects. ZnO materials are often used as varistors for the protection of electrical circuits in modern equipment and there is compelling evidence that grain boundaries play an important role in the formation of conduction barriers as described by other workers [12]. Bicrystals of ZnO used in this work were grown by solid-phase intergrowth (SPI) [13], a unique technique developed at The Russian Institute of Crystallography. The high resolution observations of the ZnO grain boundaries presented in this work were undertaken by the Russian group, and observations were interpreted in Liverpool. Unfortunately, it was not possible to obtain ZnO bicrystals for high-resolution microscopy work to be carried out in Liverpool.

The second part of this investigation consisted of characterising interfacial defects observed in high-angle grain boundaries in tungsten carbide (WC) using both conventional electron microscopy (CTEM) and the topological theory mentioned above. Previous work by Hagege [13] and Benjdir [14] revealed that characterisation of grain boundaries in this technologically important material was challenging, and WC material was obtained from the University of Caen for further investigation. Results from these experimental investigations are presented in this work.

Grain boundaries in α-alumina were also investigated but none of the boundaries examined showed resolvable dislocation structures. Some of the work associated with the understanding of this result is presented in the results section

This thesis is divided in eight chapters, which develop the ideas presented in this introduction. Chapter 2 is a critical review of theoretical and experimental studies of grain boundaries in hexagonal materials. In the first section of this chapter, the main concepts and geometrical models relevant to this study are briefly discussed (e.g. CSL, O-lattice). A section reviewing published observations of grain boundaries in selected

hexagonal materials is then presented. Chapter 3 introduces the concepts behind the topological analysis of interfaces. The different applications of the technique (i.e. *a posteriori* or *a priori*) are presented, and examples of both approaches are given. Using the framework developed by Pond [11], expressions for the diffusional fluxes associated with defect motion were derived and several examples illustrating this new approach are presented. Finally, the diffusive flux associated with two interactive defects was considered as an introduction to more general situations, and a general expression was derived.

Chapter 4 is a brief review of electron microscopical techniques used in the study of interfaces. Chapter 5 is a short account of analytical techniques used for the calculation of crystallographic parameters in the hexagonal system. The experimental methods used throughout this work are also discussed. Both experimental and theoretical results are given in Chapter 6, and discussed in chapter 7. Finally, the main conclusions drawn from this work are summarised in chapter 8.

REFERENCES

1 E.O. Hall, *Proc. Phys. Soc*, **64**, p747 (1951)

2 D.A. Smith and C.S. Nichols, Mater.Sci.Eng A, **166**, 29 (1993)

3 A.F.Cocks and M.F. Ashby, *Metal Science*, **16**, p.465 (1982)

4 J.W. Christian, *The Theory of Transformations in Metals and Alloys*, (Pergamon Press, Oxford, 1975)

5 J.P. Hirth and R.C.Pond, *Acta mater*, **44**, p4749 (1996)

6 R.C.Pond and F.Sarrazit, *Interface Science*, **4**, p99 (1996)

7 D.A Smith, *Interface Science*, **4**, p11 (1996).

8 P.J.Goodhew, *Grain Boundary Structure and Kinetics* (ASM Materials science seminar, p155), (1979).

9 A.P.Sutton and R.W. Balluffi, *Interfaces in Crystalline Materials* (Oxford University Press, Oxford), 1995.

10 E.D. Hondros and D. MacLean, *Phil.Mag* , **29**, 771 (1974).

11 R.C. Pond , *Interface Science*, **2**, p299 (1995)

12 E.Olsson and G.L.Dunlop, *J.appl.Phys*, **66**, 3666 (1989).

13 Stepantsov E.A., USSR Patent N 1116100 cL C30B33100, *Bull.Isobretenii*, **36**, p77 (1986)

Chapter 2

Review of Theoretical and Experimental Studies of Interfaces in Hexagonal Materials

Overview

Grain boundaries (GB's) are the interfaces between neighbouring crystals which differ in orientation. The structure of such interfaces has been an exciting subject of research for over a century, since it was apparent that their nature would exert some influence over the macroscopic properties exhibited by most metallic or ceramic materials. The earliest developments in this field simply regarded grain boundaries as adjacent grains held together by an amorphous cement layer [1]. This theory provided little or no structural information and persisted until it was realised that such interfaces possessed an ordered structure. Hargreaves and Hill [2] recognised this fact and proposed the transition lattice model which related for the first time the crystalline state of the abutting grains to the properties of the grain boundary. Following this idea, Burgers [3] and Bragg [4] gave one of the most successful descriptions of interfacial structures by representing low-angle GB's by means of periodic arrays of dislocations accommodating the misorientation between the constituent crystals. Although this approach failed to describe large-angle GBs, modelling in terms of discrete dislocations in order to deduce the properties exhibited by a grain boundary contributed to the advances subsequently made in this field.

The concept of the CSL, a purely geometrical tool for the characterisation of GB's, evolved from various experimental studies which showed that "special" GB's, characterised by specific relative orientations between the grains, displayed improved physical and chemical properties compared with "general" interfaces. Some of the properties accounted for include lower energy, greater resistance to grain boundary sliding, less susceptibility to impurity or solute segregation, and led to CSL's often being taken as reference structures. This model, applied in conjunction with another geometrical construction called the O-lattice, successfully characterised many interfacial dislocation arrangements observed in cubic materials

but failed, in many instances, to give an adequate description of interfacial structures in materials exhibiting non-cubic symmetry.

This chapter reviews some of the aspects cited above in more detail and presents alternative descriptions of interfacial structures . The experimental study of grain boundary structures in a range of materials exhibiting hexagonal symmetry is also briefly reviewed.

II.1 Dislocation Models Of Low-Angle Grain Boundaries

II.1.1 Bragg and Burgers Model

In 1940, Bragg and Burgers proposed a new model for the structure of GB's in which a periodic array of crystal dislocations was used to describe the misorientation between the grains constituting the boundary. Fig 2.1 is a schematic illustration of a symmetrical low-angle tilt boundary in a simple cubic lattice with lattice parameter b according to this model. Two crystals, denoted λ and μ, have been rotated with respect to each other by an angle θ about an axis describing the misorientation.

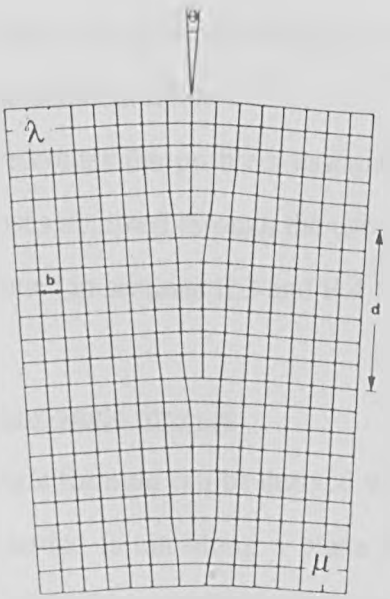

Fig 2.1: Schematic illustration of the dislocation model due to Bragg and Burgers of a symmetrical low-angle tilt boundary in a simple cubic lattice (After ref4)

As seen from this figure, the boundary consists of a periodic array of equally spaced edge dislocations (d represents the distance between each dislocation) with Burgers vector **b** . For small values of θ, the misorientation angle, which may be regarded as a net rotation resulting from the superposition of strain fields associated with each dislocation in the boundary, is given by $\theta = |b|/d$. These widely-spaced crystal dislocations, referred to as *primary* by some authors, are thought to accommodate any difference between the actual crystallographic parameters of the interface and those of an optimal structure, which in this case is the perfect crystal. It is now well established that primary dislocations are characterised by Burgers vectors equal to crystal lattice vectors. Evidence supporting this dislocation model was first obtained by Read and Shockley [5] who calculated the theoretical energy of a boundary composed of dislocations as a function of the misorientation between the grains, and obtained good agreement with experimental measurement of grain boundary energy . However, the most direct evidence for the presence of dislocations in grain boundaries came with the first observations by transmission electron microscopy (TEM) in aluminium by Hirch [6]. Despite the acceptance of this theory, it was recognised that such a description of GB's would lose its significance for values of $\theta \geq 15^{o}$ (WT Read [7]) (characterising high-angle GB's according to the Brandon [8] criterion) at which dislocations would become so closely spaced as to lose their characteristic elastic displacement fields.

An approach which overcomes the problem associated with the structure of high-angle grain boundaries was obtained through the use of the coincident site lattice and O-lattice concepts presented in sections II.3 and II.4.

II.1.2 Frank's low-angle formula

Frank's low-angle formula can be derived with reference to Figs 2.2 (a) and (b). First, a reference lattice is cut along a plane ZZ' which divides it into two lattices, λ and μ (Fig 2.2(a)). Next, lattice λ and μ are rotated by an angle $+\theta/2$ and $-\theta/2$ respectively about an axis **r** pointing into the page and passing through the

lattice point O (Fig.2.2 (b)). These two misoriented lattices are then juxtaposed to form a boundary as described in section II.3 and a probe vector **v** lying in the interface may be defined. Generally, **v** makes an angle α with **r** and Frank showed that the Burgers vector magnitude was given by

$$| \mathbf{B} | = | \mathbf{v} | 2 \sin (\theta /2) \sin \alpha , \qquad (2.1)$$

in the direction $(\mathbf{v} \times \mathbf{r})$.

As $$\mathbf{v} \times \mathbf{r} = | \mathbf{v} | \sin \alpha , \qquad (2.2)$$

We have $$| \mathbf{B} | = 2 \sin (\theta /2) (\mathbf{v} \times \mathbf{r}) . \qquad (2.3)$$

Expression (2.3) is known as Frank 's formula.

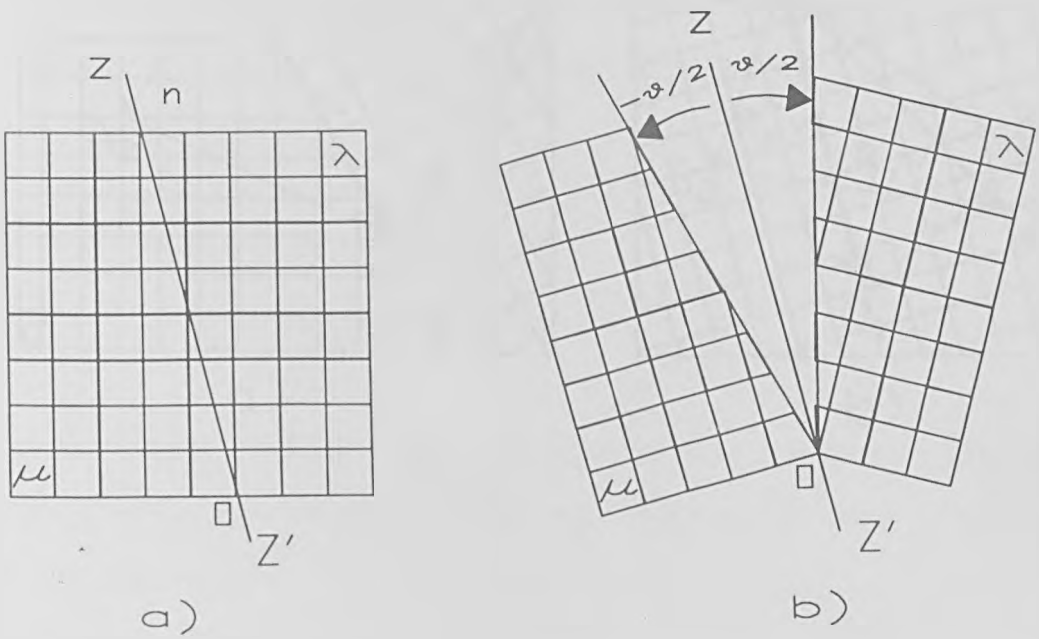

Fig 2.2: Derivation of Frank's low-angle formula. (a) The reference lattice is divided into two lattices λ and μ and (b) λ and μ are rotated by +θ/2 and -θ/2 respectively.

II.1.3 The Frank-Bilby equation

Frank [9] derived an expression giving the net dislocation content required to make two misoriented lattices fit together at an interface. This result, later generalised by Bilby and Bullough [10] to account for heterophase boundaries, is derived in this section using the Burgers circuit construction proposed by Christian [11]. Consider two lattices, λ and μ, meeting at an interface characterised by its normal **n** (see Fig 2.3 a). In Frank's treatment, it is assumed that lattices λ and μ have been obtained from some reference lattice by pure rotations represented by R_λ and R_μ respectively. When R_μ acts on one of the reference lattice vectors, its components are transformed into components of a vector in lattice μ (the same applies to R_λ).

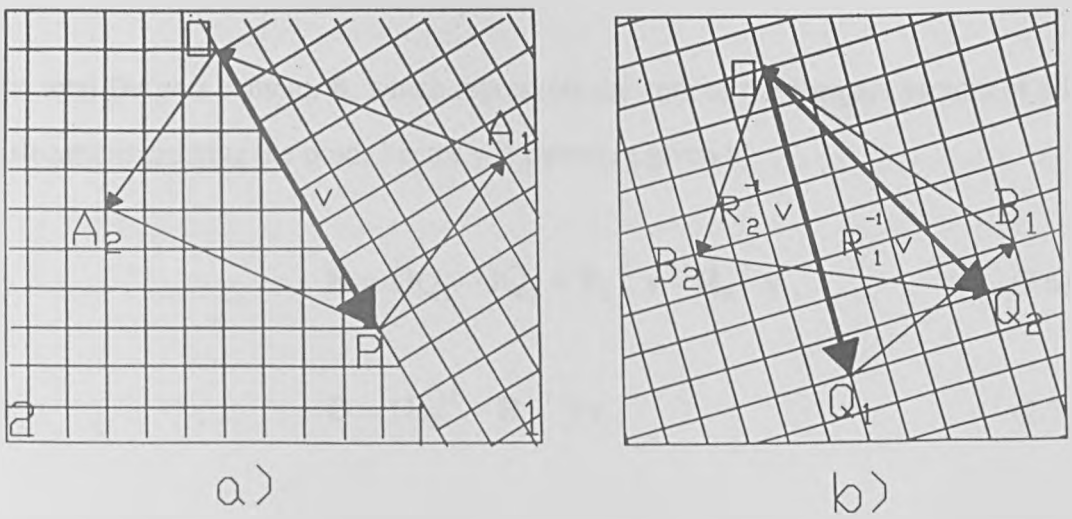

Fig 2.3: Determination of the net Burgers vector content of a grain boundary, crossed by a probe vector **v**. (a) Burgers circuit construction and (b) mapping in the reference crystal.

Consider now a probe vector **v** lying in the interface and joining points common to both crystals (Fig 2.3(b)). This can always be achieved to any degree of accuracy provided the probe vector **v** is sufficiently large. A closed right-handed circuit PA_1OA_2P encircling the interface can then be constructed as depicted in Fig 2.3(a). This circuit becomes $Q_1B_1OB_2Q_2$ when mapped into the reference crystal depicted in Fig 2.3(b), and the closure failure Q_2Q_1 representing the dislocation content of the interface can be re-written as $OQ_1 - OQ_2$. Mathematically, $Q_1B_1OB_2Q_2$ is obtained by applying the inverse transformations $\mathbf{R}_\lambda^{-1}$ and $\mathbf{R}_\mu^{-1}$ to the segments PA_1O in lattice λ, and OA_2P in lattice μ respectively. This gives the following equations

$$PA_1O = \mathbf{R}_\lambda^{-1}\,\mathbf{v} = OQ_1 \quad , \tag{2.4}$$

and

$$OA_2P = \mathbf{R}_\mu^{-1}\,\mathbf{v} = OQ_2 \quad . \tag{2.5}$$

The total Burgers content, **B**, which represents the sum of the Burgers vectors of all dislocations crossing the probe vector **v** is therefore given by

$$\mathbf{B} = OQ_1 - OQ_2 = \mathbf{R}_\lambda^{-1}\,\mathbf{v} - \mathbf{R}_B^{-1}\,\mathbf{v} \ , \tag{2.6}$$

or

$$\mathbf{B} = (\mathbf{R}_\lambda^{-1} - \mathbf{R}_\mu^{-1})\,\mathbf{v} \ , \tag{2.7}$$

expressed in the coordinate frame of the reference lattice. It might sometimes be convenient to choose one of the lattices λ or μ as the reference lattice, in which case equation (2.7) becomes

$$\mathbf{B}_\lambda = (\mathbf{I} - \mathbf{R}^{-1})\,\mathbf{v} \ , \tag{2.8}$$

if λ is selected as the reference lattice

and $$\mathbf{B}_{\mu} = (\mathbf{R} - \mathbf{I})\,\mathbf{v}\,, \tag{2.9}$$

if the reference lattice is taken as μ (I represents the identity matrix and $R = R_{\mu}R_{\lambda}^{-1}$). Equation (2.8), derived for grain boundaries in 1950, was later generalised to heterophase boundaries by Bilby to include any kind of transformations P. Equation (2.9) therefore becomes

$$\mathbf{B}_{\lambda} = (\mathbf{I} - \mathbf{P}^{-1})\,\mathbf{v}\,, \tag{2.10}$$

and is known as the Frank-Bilby equation.

It must be noted that equation (2.10) does not specify the distribution of the net Burgers vector content in the interface whereas the approach developed by Bollmann "quantisises" B into discrete Burgers vectors. Clearly, the closure failure Q_2Q_1 in Fig.2.3(b) is directly dependent upon the choice of the transformation **P** in equation (2.10). Thus, the dislocation description of a particular interface given by this model is not unique. The best representation must therefore be chosen between several possibilities and the latter does not necessarily correspond to the smallest Burgers content description .

II.2 The CSL and DSC Models

The CSL theory is based on the assumption that interfacial atoms occupying sites common to both crystal lattices are in regions of "good atomic fit". The principles underlying this theory, which are valid at any angle of misorientation, are briefly explained here with reference to high-angle interfaces. Consider two identical interpenetrating crystal lattices which are free to take up any orientation with respect to each other. Two lattice sites (one from each lattice) are arbitrarily chosen and brought into coincidence to act as origin in any further re-orientation of

the lattices. At special relative orientations, and due to the periodicity exhibited by the lattices, an infinite number of lattice sites coincide and form an array known as the coincidence site lattice (see figure 2.4) . A grain boundary can be constructed by passing a plane through the interpenetrating crystals and removing all the lattice sites from one crystal on one side of the boundary plane and from the second crystal on the other side. The volume ratio of the primitive unit cell of the CSL to that of the crystal lattice is described by the parameter Σ. The latter may also be defined as the reciprocal of the fraction of sites which are in coincidence. A low value of Σ therefore implies a large density of coincidence sites and vice versa.

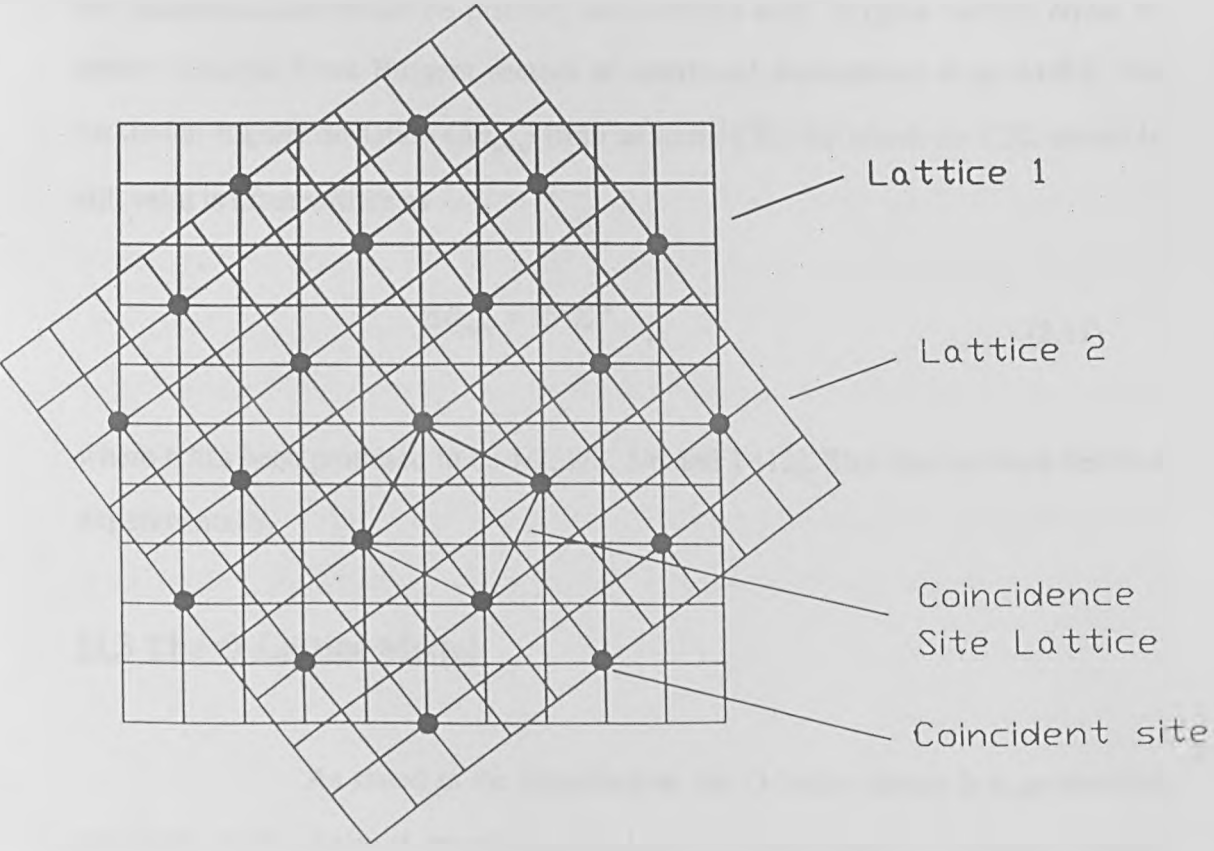

Fig.2.4 : Representation of a Σ =5 CSL (36.87°/[100])

Although all grain boundaries could in theory be represented by exact CSL relationships, Σ would, in some cases, take high values of little physical significance. Such boundaries are therefore best described by small angular deviations from low-Σ configurations, accommodated by a network of dislocations allowing the crystal to conserve the minimum energy pattern over most of the boundary surface. These dislocations are often referred to as *secondary* dislocations (SGBD's) and have Burgers vectors equal to vectors of the *displacement shift complete* (DSC) lattice. The DSC lattice defines all the possible displacements of one lattice relative to the other which locally conserve the periodicity and property of the exact CSL. The Burgers vectors of SGBD's usually correspond to the shortest translations of the appropriate DSC lattice (note that in the low-angle case, dislocations accommodating the misorientation would be primary dislocations with Burgers vectors equal to lattice vectors). Since Burgers vectors of interfacial dislocations scale with Σ, the maximum angular deviation ($\Delta\theta_{max}$) from an exact CSL for which the CSL model is still valid is often written as

$$\Delta\theta_{max} = 15^{\circ}\Sigma^{-n} \quad , \qquad (2.11)$$

where n has been proposed to be 1/2, 2/3, 5/6 and 1 [12]. This has not been verified experimentally.

II.3 The O-Lattice Model

As stated in the introduction, the O-lattice theory is a geometrical approach to the study of interfaces developed by Bollmann [13] which, like the coincidence site lattice model, associates periodic structures observed in some boundaries with optimum configurations exhibiting low energy. This approach can be regarded as a generalisation of the CSL model to include the coincidence of additional points in space which have the same internal cell coordinates in the two

interpenetrating crystal lattices. Such coincidences, which may be equivalent points, lines or planes are referred to as O-elements and define the so-called O-lattice. In general, O-lines occur for rotations, O-planes for shears and O-points for other homogeneous transformations [14]. The O-elements are thought to represent regions of exact match between the interpenetrating lattices and act as origins with respect to which the latter are interrelated. Once the O-element configuration has been calculated, each element is enclosed by a Wigner-Seitz cell (constructed by bisecting the vectors joining the O-elements) and the path of the boundary selected as to pass as close as possible to O-elements. The lines of intersection between the boundary plane and this cell structure are thought to represent positions of worst matching which may be interpreted in terms of lines of interfacial dislocations to which the correct Burgers vector can be attributed. Whereas the CSL only exists at specific orientation between the crystals, the O-lattice is "continuous" and can be defined at any angle of misorientation. It is not within the scope of this section to give an extensive description of this theory as this is well documented elsewhere (see Bollmann for example), but we shall derive the basic expression from which the dislocation content of an interface can be analysed.

Consider two arbitrarily oriented crystal lattices, λ and μ, which have been allowed to interpenetrate (λ and μ need not be of the same nature). Let us now consider a general transformation **S** which transforms lattice λ into lattice μ. A point defined by a vector **y** in lattice μ is then generated from a point defined by a vector **x** in lattice λ according to

$$\mathbf{y} = \mathbf{S}\,\mathbf{x} \ . \qquad (2.12)$$

If a translation vector **u** can be found such that **x**+**u** coincides with **y** (see Fig 2.5), then the point defined by **y** is an O-point $\mathbf{x}^{(o)}$.

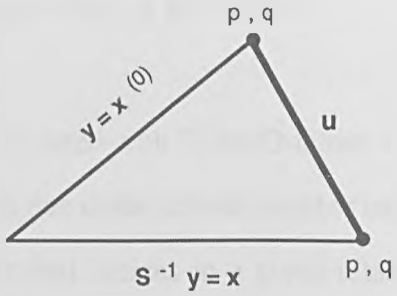

Fig 2.5: Diagram illustrating the definition of an O-point with internal coordinates equal to (p,q)

From the above, one can write the following system of equations

$$\mathbf{y} = \mathbf{x}^{(o)} , \qquad (2.13)$$

$$\mathbf{y} = \mathbf{x} + \mathbf{u} , \qquad (2.14)$$

$$\mathbf{y} = \mathbf{S}\,\mathbf{x} <=> \mathbf{I}\,\mathbf{x} = \mathbf{S}^{-1}\,\mathbf{y} = \mathbf{S}^{-1}\mathbf{x}^{(o)} . \qquad (2.15)$$

This set of equation can be re-written as

$$\mathbf{u} = \mathbf{y} - \mathbf{x} , \qquad (2.16)$$

$$\mathbf{u} = \mathbf{I}\,\mathbf{x}^{(o)} - \mathbf{S}^{-1}\,\mathbf{x}^{(o)} , \qquad (2.17)$$

$$\mathbf{u} = (\mathbf{I} - \mathbf{S}^{-1})\,\mathbf{x}^{(o)} . \qquad (2.18)$$

The O-lattice is then defined by three basis vectors given by:

$$\mathbf{x}^{(o)} = (\mathbf{I} - \mathbf{S}^{-1})^{-1}\,\mathbf{u} , \qquad (2.19)$$

Or

$$\mathbf{x}^{(o)} = \mathbf{T}^{-1}\,\mathbf{u} \qquad (2.20)$$

When a cell wall is intercepted, the discontinuity is equal to **u** which in fact represents the Burgers vector of the dislocation, $\mathbf{b}^{(L)}$ (the subscript L indicating a crystal dislocation). Thus equation (2.19) can be written as

$$\mathbf{b}^{(L)} = \mathbf{u} = (\mathbf{I} - \mathbf{S}^{-1}) \mathbf{x}^{(o)} \qquad (2.21)$$

Depending on the rank associated with T, the O-lattice may be a point, line or plane lattice. It must be noted that due to the infinite number of choices for the deformation S which relates the two crystal lattices in a given relative orientation, there is an infinite number of possible O-lattices from which "the most significant" one must be chosen. Equation (2.21) is a general expression for a boundary containing crystal dislocations and defined in one of the perfect crystal lattices. At high-angle of misorientation, the procedure described above remains the same except that crystal lattices λ and μ are replaced by two DSC lattices and the angular deviation of the crystal lattices is replaced by the deviation from the coincident orientation. The two DSC lattices are related by $\mathbf{S'S}^{-1} = \mathbf{A}$, where $\mathbf{S'}$ is the transformation producing an orientation close to a coincidence, and an 02 lattice (composed of 02-elements) is constructed between them [15]. In this instance, the general expression given in (2.19) becomes

$$\mathbf{x}^{(o2)} = (\mathbf{I} - \mathbf{A}^{-1})^{-1} \mathbf{d}^{(sc)} . \qquad (2.22)$$

II.4 The Coincidence Model in Non-Cubic Structures

As mentioned in the introduction , the adaptation of the CSL model to the study of GB's in non-cubic materials failed to provide a successful description of such interfacial structures in many instances (see section II.4.2). This section describes the main modifications brought to the original CSL model for analysis of materials exhibiting hexagonal symmetry as this is of particular interest in this work, and highlights the limitations of this approach.

II.4.1 The CCSL model

As discussed in section II.3, the characterisation of interfacial dislocations using the "O-Lattice" theory is based on the existence of a coincidence site lattice. Indeed, the DSC lattice, whose shortest vectors represent possible Burgers vector of such dislocations, is directly linked to the existence of a CSL. In hexagonal materials, the three-dimensional coincident site lattice depends on the c/a ratio and only exists for rotations about the [0001] axis or when the ratio $(c/a)^2$ is a rational fraction [16]. For most materials this ratio takes irrational values , and constraint is normally applied to the C-axis so that $(c/a)^2$ is forced to a rational value describing a true CSL. The coincidence site lattice obtained in this way is referred to as a constrained CSL and is abbreviated CCSL. CCSL's corresponding to c/a ratios close to those of most hexagonal metals have been tabulated by several authors (references [16] and [17] for example).

Following this approach, interfacial dislocations are characterised using a modified approach of the O-lattice which takes into account the constraint discussed above. This approach is described in detail elsewhere ([18] for example).

II.4.2 Physical significance of the CSL model and alternative approaches

As stated earlier, exceptional grain boundary properties exhibited at special orientations associated with low Σ CSL's mostly accounted for the choice of such configurations as reference structures. However, several limitations may be identified. For example, atomic relaxation at grain boundaries may invalidate the concept on which the CSL is based and in some cases, it is difficult to identify a coincidence site in a complicated pattern, or the existence of an infinity of orientations for which no coincident site lattice exist. In addition, small variations in the c/a ratio affect the dislocation pattern predicted by this method, as discussed by Shin and King [19]. The CSL model may therefore be useful in some cases but seems to contain disadvantages and questionable hypotheses. Its only physical

significance appears to be the periodic structure exhibited by a boundary which is parallel to a rational plane of the CSL [20] . Pond [21] proposed an alternative approach to the characterisation of interfacial defects separating energetically degenerate regions of interfaces. This method does not contain any hypotheses and is completely consistent with the topological theory of defects. The only requirement needed to characterise interfacial discontinuities is the full symmetry and relative orientation of the crystals constituting the interface.Pond indicated that the symmetry reduction resulting from the creation of a bicrystal (by bonding together appropriately prepared surfaces on the two constituent crystals) can lead to the formation of interfacial defects which can be predicted or characterised topologically by means of a general expression. This topological approach to the study of interfacial defects is presented in detail in the following chapter.

II.5 Experimental Studies Of Grain Boundary Structures In Materials Exhibiting Hexagonal Symmetry.

Hexagonal materials are increasingly being used in technologically important applications and a considerable amount of literature concerning the study of interfacial features in such materials is now available. The vast majority of these studies uses the CCSL and O-lattice models described earlier, and the review presented below discusses the suitability of this approach for the characterisation of low and high angle grain boundaries.

II.5.1- Low-angle grain boundaries

MacLaren and Aindow [22] studied the structure of low-angle grain boundaries in high-purity zinc (Zn) by means of the O-lattice model described in II.3. One of the boundaries presented consisted of a hexagonal network of near-screw dislocation segments with Burgers vectors found to be consistent with perfect

crystal dislocations. Although the morphology of this network seemed to be consistent with that calculated using Bollmann's approach, a significant discrepancy was found between the spacing of observed and predicted features. It is therefore unlikely that the approach adopted resulted in the correct identification of the Burgers vectors of the observed dislocations. A possible reason for this could be the large uncertainty associated with rotation axis measurements as reported by the authors. Other workers presented a study of a low-angle grain boundary in zinc consisting of a stepped arrangement of dislocations [23]. Again, this network of dislocations was compared with that predicted by the O-lattice approach, and a relatively good match was claimed. However, no comparison between measured and predicted line directions was indicated and, based on MacLaren's work, one has to be sceptical about the validity of this result.

Lay, Delavignette and Vicens [24] studied several low-angle grain boundaries in deformed tungsten carbide (WC). Although the vast majority of the boundaries investigated were represented by very low angles of rotation (close to 1°), more complex interfaces associated with higher misorientation angles were also observed. Most of the defects observed in the subgrain boundaries were perfect dislocations and were successfully characterised using transmission electron microscopy. However, the second class of observed boundaries consisted of more complex arrangements of interfacial dislocations and the O-lattice approach adopted here did not allow the correct Burgers vectors of the defects to be identified.

The approach used in the experimental studies presented above is characteristic of the methodology adopted by most workers in this field and often leads to similar inconsistencies in the reported results. Although a good match between the morphologies of calculated and experimentally observed dislocation networks is claimed, calculated line directions and dislocation spacings, for example, cannot be matched to experimental ones. These significant discrepancies suggest an incorrect characterisation of interfacial defects and reflect the difficulties associated with this method.

The characterisation of interfacial defects in high angle grain boundaries requires the identification of plausible reference structures from which the experimental boundary deviates. Experimental evidence suggests that periodic structures corresponding to special orientations are suitable references and the CCSL model is therefore used extensively for such identifications. The section below presents examples of such studies and reviews the usefulness of the CCSL/O-lattice approach for the identification of interfacial defects in high-angle boundaries.

II.5.2 High angle grain boundaries

Vicens et al [25] analysed the structure of high-angle grain boundaries in tungsten carbide using HREM and showed that the most frequent orientations were close to $\Sigma=2$ (approximating the exact value of c/a= 0.976 to be 1). Two $\Sigma=2$ boundaries were analysed and interfacial defects were observed in both cases. The deviation from the exact coincidence was calculated to be 5^0 but no attempt was made to match these experimental observations and measurements to calculated configurations. MacLaren [26] investigated the possible reference structure adopted by high-angle grain boundaries in pure titanium. One of the boundaries analysed was found to have a mixed tilt-twist character and consisted of a well-defined array of dislocations. However, no suitable CCSL's could be found close to the experimental orientation and an alternative approach considering a 2-D periodicity in the boundary plane was investigated. A list of the possible Burgers vectors associated with the observed interfacial dislocations was established using Pond's topological approach and the morphology of the network was predicted using the O2-lattice algorithm described in II.3. A "morphological" match was obtained but a significant discrepancy was found between experimentally-measured and predicted line directions. Again, this inconstancy might suggest an incorrect identification of the topological parameters describing this boundary.

Chen and King [27] studied several high-angle grain boundaries with orientations close to the $(01\bar{1}2)$ twin in zinc. Two of the selected boundaries contained a network

of dislocations and the O-lattice approach described in II.4 was used to characterise these defects. Whereas the morphology of the first network seemed to match that predicted using a Σ=13 CCSL reference structure, no solution was found for the second dislocation arrangement. Unfortunately, no comparison between the spacing of calculated and predicted individual dislocations making up the Σ=13 boundary was presented and it is therefore impossible to comment on the choice of this CCSL as a possible reference structure adopted by this boundary.

Lay and Nouet [28] investigated the structure of grain boundaries with orientations close to the $(\bar{0}112)$ in magnesium. These boundaries contained several networks of dislocations and various CCSL's were considered as possible reference structures for this system. Whereas the choice of a specific CCSL did not seem to affect the predicted line directions of the observed dislocations, their spacing appeared to be significantly altered. Unfortunately, the identification of any plausible reference structures was not carried out by calculating the deviation from the ideal twin orientation and hence any conclusions reached seem to be questionable, as indicated by MacLaren [26]. Twin boundaries were also studied in a range a hexagonal-close-packed metals by Antonopoulos and co-workers [29], and Komninou et al [30]. Although several dislocation networks were observed in cadmium and titanium twins, the latter were not characterised topologically. Grimmer, Bonnet, Lartigue and Priester [31] studied 133 grain boundaries in α-alumina using the O2-lattice algorithm presented in II.4. The analysis of a twin containing three sets of dislocations allowed three CCSL's to be identified as possible reference structures for this system. The determination of the Burgers vectors associated with those dislocations was then attempted using both invisibility criteria and image simulation but the contrast displayed was very similar in each case. It followed that the identification of a specific CCSL as reference structure was impossible using this approach.

Based on the arguments presented above it emerges that the use of the CCSL and O-lattice models for the characterisation of high-angle grain boundaries is often

problematic and often leads to discrepancies between experimental and predicted measurements. A indicated in II.4.1, the mathematical formulation of the CCSL approach contains some misrepresentations which may result in inconsistencies between experimental observations and theory. The method developed by Pond[21], which does not contain hypotheses and is consistent with the topological theory of defects, was successfully used by Braisaz et al [32], for the characterisation of twin boundaries in zinc and titanium using high resolution electron microscopy (HREM) . Having successfully identified several interfacial defects, the authors were then able to discuss possible interaction mechanisms between them. This study demonstrates the suitability of thes method for such purposes since, unlike the conventional CCSL/O-lattice models, experimental results are fully consistent with observations. This approach was therefore preferred for the characterisation of grain boundaries in ZnO presented in this work.

References

1 Rosenhain, W., *Metall. Suplt. Engineer*, **1**, 2 (1925)

2 Hargreaves, F., Hills, R.J., *J. Inst. Met.*, **41**, p257 (1929)

3 Burgers, J.M., *Proc.K.Ned.Akad.Wet.*, **42**, p293 (1939)

4 Bragg, W.L., *Proc.Phys.Soc.*, **52**, p54 (1940)

5 Read, W.T., Shockley, W., *Phys.Rev.*, **78**, p275 (1950)

6 Hirsch, P.B., Howie, A., Nicholson, R.B, Pashley, D.W, Whelan, M.J, *Electron Microscopy of Thin Crystals* (Butterworth, Sevenoaks) (1965).

7 Read, W.T., *Dislocations in Crystals* (MacGraw-Hill, New York, 1953)

8 Brandon, D.G., *Acta.Metall.*, **14**, p1479 (1966)

9 Frank, F.C., in *Symposim on The Plastic Deformation of Crystalline Solids*, Pittsburgh, Pa., Office of Naval Research, p150 (1950)

10 Bilby, B.A, Bullough, R., *Proc.Phys.Soc.*, **69B**, p1276 (1956)

11 Christian, J.W, *The Theory of Transformations in Metals and Alloys* (Oxford; Pergamon Press, 1975)

12 Smith, D.A., *Interface Science* , **4**, p11 (1997).

13 Bollmann, W., *Crystal Defects and Crystalline Interfaces* (Berlin:Springer- Verlag, 1970)

14 Pond R.C., Smith D.A., *Can.Met.Quat.* **13**, p39 (1974).

15 Warrington D.H., Bollmann W., *Phil.Mag A.*, **25** p771 (1972)

16 Bonnet, R., Cousineau, E., Warrington, D.H, *Acta Cryst.*, **A37**, p184 (1981)

17 Chen, F.R., King, A.H., *Acta Cryst.*, **B43**, p416 (1987)

18 MacLaren, I., Aindow, M., *Phil.Mag.Let.*, **76**, 1, p25 (1997)

19 Shin, K., King, A.H., *Phil.Mag.*, **A63**, p1023 (1991)

20 Sutton., A.P., *Inst.Metals Revs.*, **29**, p377 (1984)

21 Pond, R.C., *Dislocations and Properties of Real Materials* (edited by M.Loretto, Institute of Metals, London, p71) (1985)

22 MacLaren, I., Aindow, M., *Script.Metall.Mater.*, **29**, p 811 (1993)

23 King, A.H., Chen, F.R., *Mater.Sci.Eng.*, **81**, p51 (1986)

24 Lay, S., Delavignette, P., Vincens, J., *Phys.Stat.Sol.*, **A90**, p53 (1985)

25 Vincens, J., Laurent-Pinson, E., Chermant, J-L., Nouet., G., *J.Phys* (Paris), **49 C5**, p271 (1988)

26 MacLaren, I., PhD Thesis, *University of Birmingham* (1993)

27 Chen, F.R., King, A.H., *Phil.Mag.*, **A57**, p431 (1988a)

28 Lay, S., Nouet, G., *Act.Metall.Mater.*, **41**, p1511 (1993)

29 Antonopoulos, J.G., Karakostas, TH., Kominou, Ph., Delavignette, P., *Acta Metall.*, **36**, p2493 (1988)

30 Komninou, PH., Polychroniadis, E., Antonopoulos, J.G., Karakostas, TH., Delavignette, P., *J.Phys.* (Paris) **51 C1**, p215 (1990)

31 Grimmer, H., Bonnet, R., Lartigue, S., Priester, L., *Phil.Mag A.*, **A61**, p493 (1990)

32 Braisaz, T., PhD Thesis, *Universite de Caen* (France), 1996

Chapter 3

Topological Characterisation of Interfacial Defects and Associated Diffusive Fluxes

Overview

Interfacial defects have been successfully characterised in a wide range of materials exhibiting cubic symmetry using geometrical constructs such as those presented in chapter 2. As discussed earlier, the adaptation of such techniques to the study of defects in non-cubic materials introduces hypotheses of questionable physical significance. The method presented here does not contain such hypotheses and is completely consistent with the topological theory of defects. Indeed, the only requirement needed to characterise discontinuities is the full symmetry and relative orientation of the crystals constituting the interface . This approach may be applied *a-priori* to predict the nature of the defects that may arise in a given interface or *a-posteriori* to characterise observed discontinuities.

The techniques commonly used to characterise defects in single crystals are first discussed and the crystallographic origin of interfacial defects is briefly introduced. The topological theory is then presented together with examples of its application in various interfaces. The third part of this chapter uses the framework described above to derive diffusive fluxes associated with interfacial line-defect motion and examples are used to illustrate defect motion in grain and interphase boundaries. The interaction between individual defects in situations involving grain boundaries is then considered and a general expression for the interaction of two dislocations is derived for the first time.

III-1 Conventional Methods For Defect Characterisation In Single Crystals

III.1.1 Volterra's approach

This is an imaginary procedure facilitating the visualisation of line defects, in which a cut is made inside the body of an object, e.g. a hollow rubber tube [1], followed by displacements carried out on one face of the cut with respect to the other (see Fig.3.1). If those displacements are restricted to symmetry operations, the

two surfaces may then be brought back together in proper registry by the addition or removal of extra material. The above procedure introduces a line defect known as a dislocation, disclination or dispiration depending on whether the symmetry operation relating the cut surfaces is a translation, proper rotation or proper screw-rotation respectively (see Fig 3.1). These operations are referred to as admissible.

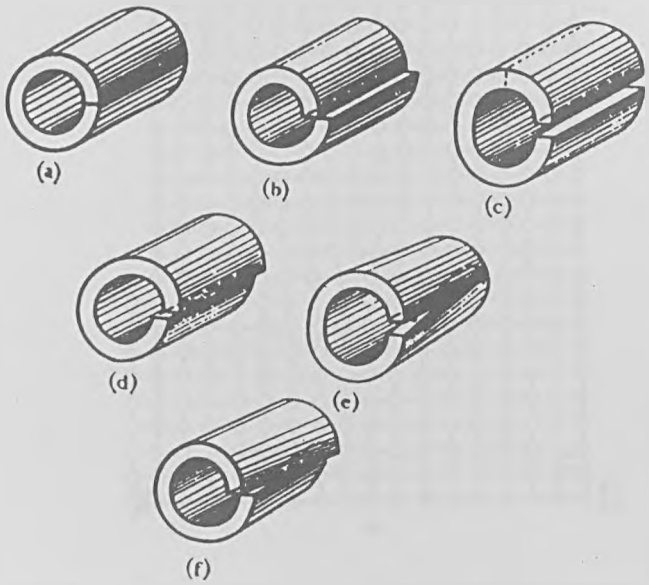

Fig. 3.1: A schematic illustration of line discontinuities in a hollow circular cylinder. (a) initial cut, (b) and (c) edge dislocations, (d) screw dislocation, (e) and (f) disclinations ; (After ref. [1])

III.1.2 Characterisation by construction of a Burgers circuit

This method was developed by Frank [2] in the 1950's for the characterisation of defects in single crystals and is illustrated in Fig. 3.2.(a and b). This analysis is carried out graphically by constructing a closed circuit around some kind of defect, in this case a simple dislocation, and subsequently mapping it into a reference space which is often taken as the perfect crystal. By convention, the defect is assigned a line direction, ξ, and the circuit is constructed in a right-handed sense with respect to ξ (Fig. 3.2.a). When the crystal contains a dislocation, the mapping process fails and the closure failure characterises the defect . By convention, the Burgers vector of the defect is equal to the displacement from the finish (F) to the start (S) of the circuit (Fig

3.2.b) and the line direction of the defect ξ is pointing into the page. Although Frank only dealt with translation symmetry, it is possible to generalise the method by including all the symmetries exhibited by the crystal. The latter consideration forms the basis of the method used in this work for the characterisation of interfacial line defects explained in section III.3.

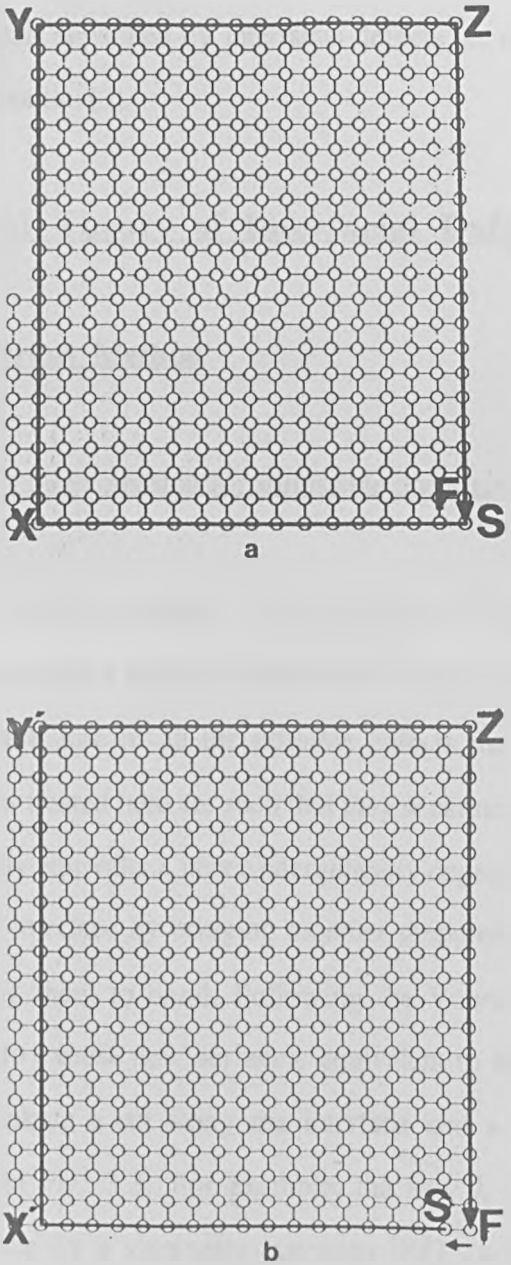

Fig. 3.2: Illustration of the charactrisation of a dislocation in a single crystal. (a) A Burgers circuit, PQRSP, is constructed around the defect. (b) The circuit is mapped into the perfect crystal. (after ref.[2])

III-2 Crystallographic Origin of Interfacial Defects

Imagine two component crystals referred to as being black (μ) and white (λ), and exhibiting the symmetry operations contained in their respective space groups. A bicrystal may then be formed by bringing together surfaces that have been appropriately prepared on both the λ and μ crystals. This process generally reduces the symmetry initially present in the component crystals and leads to the coexistence of several variant bicrystals separated by interfacial defects, as stipulated in the principle of symmetry compensation [3].

III.3 Topological Theory of Interfacial Defects

III.3.1 A-Priori Method

a) General expression for admissible line discontinuities

In this section, the formation of interfacial line-defects is visualised schematically and a general mathematical expression, derived by Pond [4], is used to predict the nature of all the possible defects that may be encountered in interfaces. The defects treated here are such that they separate interfacial structures that are crystallographically equivalent, hence energetically degenerate. Fig 3.3a shows the formation of such an interface by bringing together prepared surfaces on the λ and μ crystals, and allowing them to bond. Following the Volterra approach described in III.1.1 it is possible to expose new surfaces, equivalent to initial ones, on both the λ and μ crystals by making a cut along the interface and adding or removing extra material as depicted in Fig. 3.3. For example, the new λ surface in Fig. 3.3(b) is related to the initial one by a symmetry operation $\mathcal{W}(\lambda)$ which could be a rotation, translation, mirror-glide. and is therefore crystallographically equivalent to it. If the same procedure is carried out on the μ crystal, the new interface is energetically degenerate with the initial one. In the Volterra procedure, the operation which brings

the two surfaces together is the operation characterising the defect and is always a symmetry operation belonging to the single crystal. For an interface, the operation that brings the new μ surface onto the new λ surface is the inverse of the black operation, followed by the white one, as shown schematically in Fig. 3.4 for operations which are displacements only.

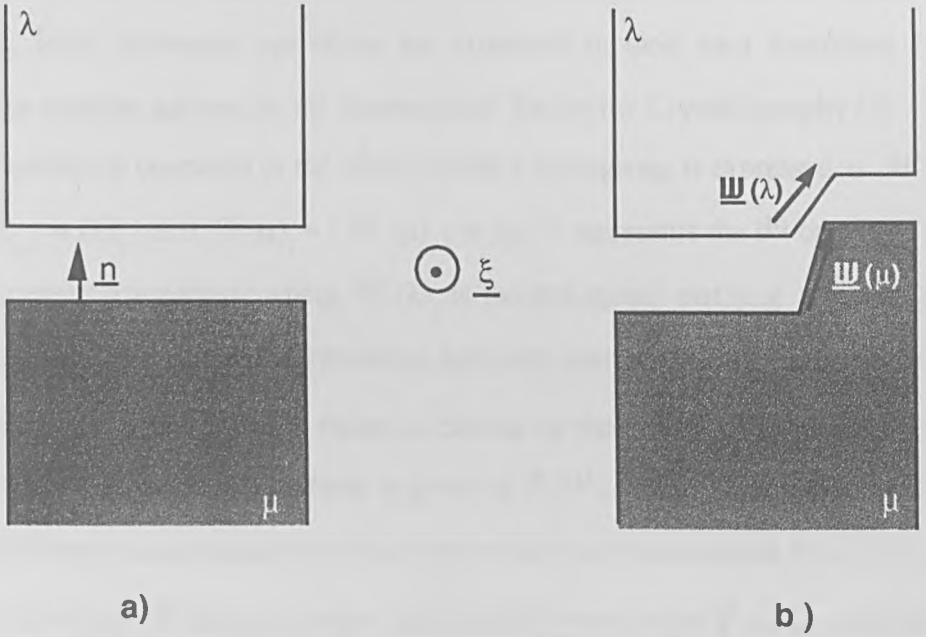

Fig 3.3: (a) Initial surfaces to be joined together and (b) new surfaces exposed on the white and black crystals related to the initial ones by symmetry operations expressed as W(λ) and W(μ) respectively.

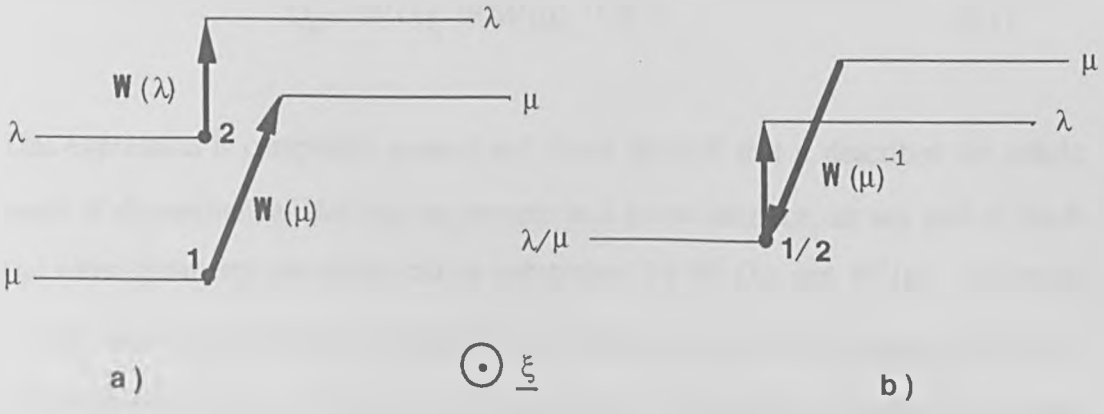

Fig 3.4 : Formation of a bicrystal; (a) the initial surfaces to be brought together (locations 1 and 2 represent equivalent points) and (b) the operation that brings the new black surface onto the new white is the inverse of the μ operation followed by the white one.

Thus, the total operation consists of a proper combination of symmetry operations, one from each crystal. In order to be able to predict the nature of all the line-defects that can be introduced into an interface, Pond's treatment identifies the various surfaces which can be created on each of the component crystals by expressing the combined operation discussed above mathematically. First, the relative orientation of the two crystals is specified by the operation $\mathcal{P}$ (**P**, **p**) where **P** is the matrix relating the black and white coordinate frames and **p** represents the relative position of the two crystals. Next, symmetry operations are expressed in their own coordinate frames using the notation adopted in the International Tables for Crystallography [5] . Thus, the j^{th} symmetry operation of the white crystal's spacegroup is expressed as $\mathcal{W}(\lambda)_j$ = (**W** $(\lambda)_j$; **w** $(\lambda)_j$) and $\mathcal{W}(\mu)_i$ = (**W** $(\mu)_i$; **w** $(\mu)_i$) represents the i^{th} operation of the black crystal's spacegroup; where $\mathcal{W}(\lambda)_j$ is the orthogonal part (e.g. rotation, mirror or inversion) and **w** $(\lambda)_j$ is the translation part (and similarly for the black crystal). By convention the white crystal's frame is chosen as the reference space and a black operation re-expressed in this frame is given by $\mathcal{P}\,\mathcal{W}(\mu)_i\,\mathcal{P}^{-1}$. Let the operation that brings the new black surface onto the new white one be designated by $Q_{ij}=(Q_{ij},q_{ij})$. The inverse of the i^{th} black symmetry operation followed by the j^{th} white operation will therefore be given by:

$$Q_{ij} = \mathcal{W}(\lambda)_j\ \mathcal{P}\,\mathcal{W}(\mu)_i^{-1}\,\mathcal{P}^{-1} \quad . \qquad (3.1)$$

This expression is completely general and Pond showed that it described the whole range of discontinuities that may be present in a given interface, as any pair of black and white symmetry operations can be substituted for $\mathcal{W}(\lambda)_j$ and $\mathcal{W}(\mu)_i$. The range of admissible interfacial defects depends upon the extent to which symmetry has been broken when forming the bicrystal. The lesser the symmetries in common the greater is the range of admissible defects.

III.3.2 Catalogue of Interfacial Defects

As explained in the previous section , the general formulation given in (3.1) may lead to a very large variety of admissible defects for a given interface. The various possibilities have been investigated in detail by Hirth and Pond [6] who showed that the latter could be grouped into three distinct categories. Category one is associated with various types of dislocations whereas categories 2 and 3 contain more complex defects, rarely observed experimentally .

Category 1: Dislocations

a) Crystal dislocations

Crystal dislocations are defects that can also arise in interfaces. This corresponds to the substitution of translation operations (characterised by $\mathbf{t}(\lambda)$ and $\mathbf{t}(\mu)$ in the white and black crystals respectively) into equation (1); e.g. $\mathcal{W}(\lambda)_j = (\mathbf{I}, \mathbf{t}(\lambda)_j)$ with $\mathcal{W}(\mu)_i$ taken as the identity $\mathcal{W}(\mu)_i = (\mathbf{I}, 0)$ or vice versa. In this particular case we have $Q_{ij} = (\mathbf{I}, \mathbf{t}(\lambda)_j)$ or $Q_{ij} = (\mathbf{I}, \mathbf{P}\ \mathbf{t}(\mu)_i)$ and the defect is either a white crystal dislocation with Burgers vector $\mathbf{b}_{ij} = \mathbf{t}(\lambda)_j$ or a black one with a Burgers vector equal to $\mathbf{P}\ \mathbf{t}(\mu)_i$. Dislocations of this type are often observed in low-angle grain boundaries (see chapter 2).

b) Interfacial dislocations

- Class 1: Broken-translation symmetry

Interfacial dislocations are confined to the interface and are predicted by substituting a white translation operation ($\mathcal{W}(\lambda)_j = (\mathbf{I}, \mathbf{t}(\lambda)_j)$) and a black one ($\mathcal{W}(\mu)_i = (\mathbf{I}, \mathbf{t}(\mu)_i)$) into equation (3.1). Dislocations of this type have Burgers vectors equal to

$$\mathbf{q}_{ij} = \mathbf{b}_{ij} = \mathbf{t}(\lambda)_j - \mathbf{P}\,\mathbf{t}(\mu)_i , \qquad (3.2)$$

and belong to the class of "broken-translation symmetry" [6]. An example of such defects are DSC - type dislocations (see chapter 2).

Fig 3.3 (b) is a schematic representation of the formation of such dislocations. The black and white surfaces to be bonded exhibit different surface steps and this results in the introduction of a dislocation of the type described above. Note that the unique interfacial unit normal is taken to point into the white crystal and that the defect is characterised by operations which relate the crystal surfaces on its left to those on its right when looking along ξ and into the white crystal, which is consistent with the RH/FS convention.

- Class 2 : Frustrated translation symmetry

In this class, dislocations may arise due to "frustrated symmetry" and are present when screw-rotation or mirror-glide planes in the two crystals forming the interface are aligned but have different displacements, **w**, associated with them. The black and white symmetry operations described above are expressed as $\mathcal{W}(\lambda)_j = (\mathbf{W}(\lambda)_j ; \mathbf{w}(\lambda)_j)$ and $\mathcal{W}(\mu)_i = (\mathbf{W}(\mu)_i ; \mathbf{w}(\mu)_i)$ where $\mathcal{W}(\lambda)_j = \mathbf{P}\,\mathbf{W}(\mu)_i^{-1}\,\mathbf{P}^{-1}$ due to the alignment of the symmetry elements. These dislocations have Burgers vectors defined as

$$\mathbf{b}_{ij} = \mathbf{w}(\lambda)_j - \mathbf{P}\,\mathbf{w}(\mu)_i + (\mathbf{w}(\lambda)_j - \mathbf{I})\,\mathbf{p}. \qquad (3.3)$$

Fig 3.5 is a schematic representation of the formation of such defects where the two surface features on either side of the defect are free surface demi-steps [6].

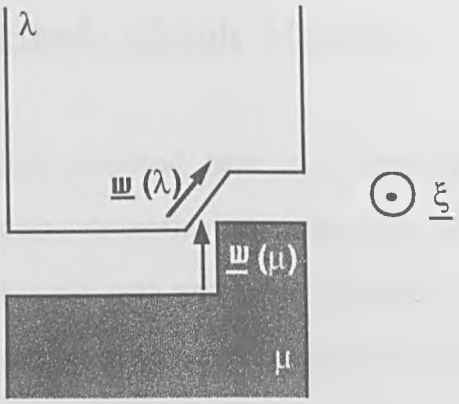

Fig. 3.5: formation of defects belonging to the class of frustrated translation symmetry

- Class 3: "Broken-coincident symmetry"

Class 3 dislocations are a special case of the "frustrated translation symmetry" described above where the black and white symmetry operations are aligned and identical but the value of the associated displacement **p** breaks the coincident point symmetry [6]. These dislocations are characterised by Burgers vectors given by

$$\mathbf{b}_{ij} = (\mathbf{w}(\lambda)_j - \mathbf{I})\, \mathbf{p} , \qquad (3.4)$$

and are referred to as belonging to the class of "broken-coincident symmetry".

Categories 2 and 3 : Interfacial disclinations and dispirations

These types of defects belong to distinct categories and arise when Q_{ij} is either a proper rotation (disclinations) or a proper screw-rotation (dispirations). These defects, although rarely observed, have been investigated by Hirth and Pond [6] who gave several examples of their occurrence. The reader is therefore referred to this reference for more details.

III.4 *A-Posteriori* Method- Circuit Mapping

The *a-posteriori* method described here is a graphical approach to the characterisation of crystal/interfacial discontinuities based on the earlier work by Frank [2]. Whereas Frank dealt exclusively with translation symmetry, the present method includes all the symmetries found in crystal spacegroups. The basics of the theory are first set out for single crystals and a detailed explanation of its application to the study of interfacial defects is subsequently given.

III.4.1 Circuit mapping in faulted single crystals

Imagine a material containing a dislocation or any other type of line-defect around which a right-handed circuit, linking sites related by symmetry operations is constructed. It is possible to express such a circuit mathematically in order to show the equivalence of the method with the *a-priori* approach described earlier. This is done by introducing an imaginary observer who is transported on an excursion through the faulted material in such a way that the steps constituting his journey correspond to the circuit constructed around the defect. In other words, the observer is only allowed to make displacements which correspond to the symmetry operations found in the spacegroup of the crystal. It is also convenient to consider the observer as having "special features" so that, for example, he cannot see the strain associated with the defect and always sees the material in his immediate environment as being perfect. His motions being restricted to symmetry operations, everytime the observer reaches a new site (atomic or not), the environment looks unchanged. As in Frank's treatment, once his journey is completed, it is mapped into some reference space. The operation which transports the observer from the final point of his journey to the starting point is then the operation characterising the defect. The dichromatic complex is a construction often chosen as the reference space in which the circuit is

mapped, as it contains the symmetry exhibited by both crystals. The dichromatic complex is obtained by allowing the two crystal structures to interpenetrate. The whole sequence of operations making up the journey are written down mathematically by expressing individual stages as $\mathcal{W}_1$, $\mathcal{W}_2$, $\mathcal{W}_3$, ...,$\mathcal{W}_i$ and the overall operation is then defined as C(**C**,**c**) where **C** is the orthogonal part and **c** the translation part. . Imagine now that the observer starts his excursion in a specific orientation from a point S defined with respect to a chosen origin by the vector **s**. If, during the course of his journey, the next operation in the sequence (e.g. a translation) , the i^{th} say, acts on the observer at his present location, the latter displacement is represented by $\mathcal{W}_i$=(**I**,t). However, when the next operation in the sequence does not act through the observer's current location but through some other point r_i, the i^{th} operation is written as

$$\mathcal{W}_i^* = (\mathbf{I}, r_i)\, \mathcal{W}i\, (\mathbf{I}, r_i)^{-1} \quad . \tag{3.5}$$

The complete journey is therefore mathematically written as:

$$C(\mathbf{C}, \mathbf{c}) = \mathcal{W}^*_n \ldots\ldots \mathcal{W}^*_3 \; \mathcal{W}^*_2 \; \mathcal{W}^*_1 \quad . \tag{3.6}$$

When $C = (\mathbf{I}, \mathbf{0}) = 0$, the circuit is closed and several examples of such situations have been illustrated by Hirth and Pond [6].

The meaning of the circuit operator C is that when it acts upon the observer's starting location, it takes him directly to the finishing point of his excursion. Moreover, in order to be consistent with the RF/FS convention, C^{-1} is the operation which characterises the defect and relates the observer's final status to his starting position and orientation.

III.4.2 Circuit mapping to characterise interfacial dislocations

The method described in III.4.1 for the analysis of discontinuities in single crystals can be extended to interfacial defects by considering a right-handed circuit through both the crystals constituting the bicrystal (see Fig 3.6). The circuit now comprises two segments, one white and one black, which represent the observer's journey in the λ and μ crystals respectively. The sequence of operations in the white crystal, from the starting point S to a point X in vicinity of the interface, is represented by the operator $C(\lambda)$ and similarly, $C(\mu)$ represents the observer's journey in the black crystal from a point Y to the location represented by Z. The latter becomes $\mathbf{P}\,C(\mu)\,\mathbf{P}^{-1}$ when re-expressed in the white reference frame.

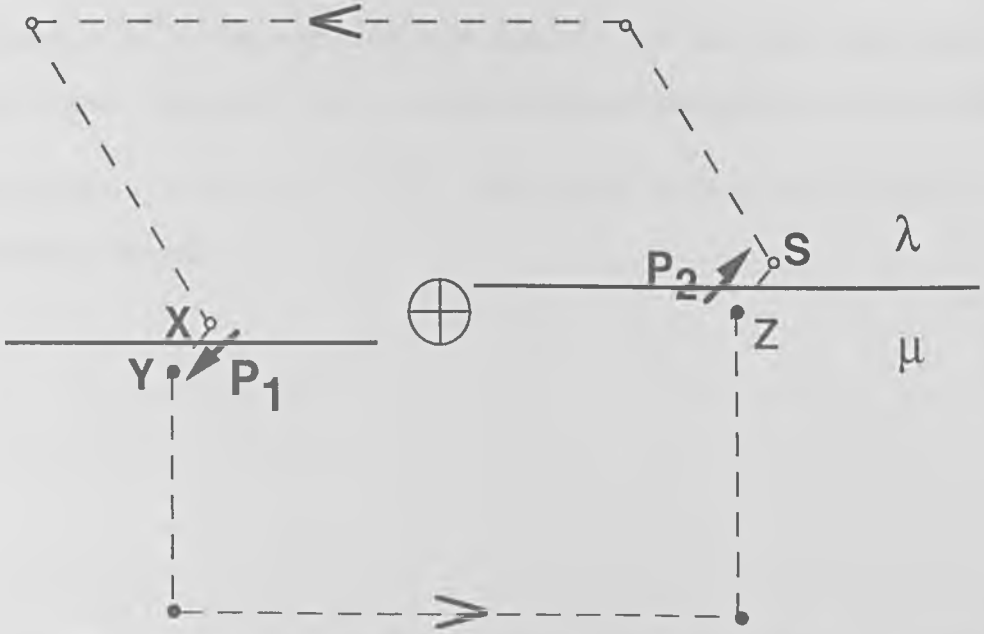

Fig 3.6: Schematic illustration of the circuit mapping technique adapted to bicrystals.

The observer starts his excursion from a point S and pursues his journey through the white crystal by successive white symmetry operations until he reaches X. At this point, he crosses the interface by a displacement represented by $(\mathbf{I},\mathbf{p}_1)$ which takes him to Y in the black crystal. The sequence of operations in this crystal takes him to Z where he experiences a displacement defined by $(\mathbf{I}, \mathbf{p}_2)$ across the interface which

closes the circuit. If the defect in question separates identical structures, the displacement $(\mathbf{I}, \mathbf{p}_2)$ is simply $(\mathbf{I}, \mathbf{p}_1)^{-1}$. The total circuit is now mapped into a reference space and if the dichromatic complex is chosen, the circuit operation as the form:

$$\mathbf{C}(\lambda, \mu) = (\mathbf{I}, \mathbf{p}_2)\, \mathbf{P}\, C(\mu)\, \mathbf{P}^{-1}\, (\mathbf{I}, \mathbf{p}_1)\, C(\lambda), \qquad (3.7)$$

for the simple case described above, and $\mathbf{C}(\lambda, \mu)^{-1}$ characterises the defect. This method is now illustrated by considering an interfacial defect in a coherent interface between fcc and hcp crystals (see Fig 3.7). The fcc material is taken to be white (λ) and the hcp black (μ), and these are separted by an interface with the following parallel directions; $(111)^{\lambda}$ // $(0001)^{\mu}$ and $\langle 1\bar{1}0\rangle^{\lambda}$ // $\langle 2\bar{1}\bar{1}0\rangle^{\mu}$.The vectors $\mathbf{t}(\lambda)$ and $\mathbf{t}(\mu)$ indicated in Fig 3.7 characterise the steps associated with the defect in the white and black crystals respectively, and the circuit indicated characterises a defect with a Burgers vector equal to $\mathbf{b}=1/6\,[11\bar{2}]$. The various symbols used in Fig 3.7 are explained in appendix 1)

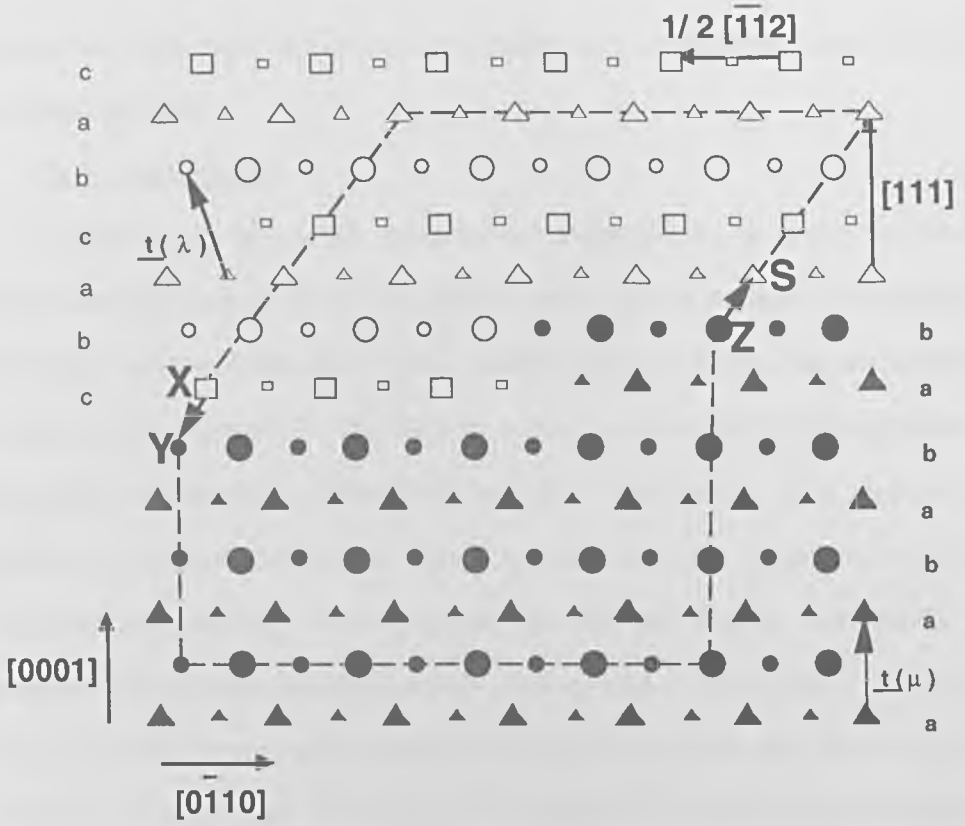

Fig 3.7: Construction of a circuit around an interfacial defect in a fcc:hcp interface.(after ref[7]).

Additional fcc:hcp interfaces can be created by terminating the fcc crystal by an a,b or c plane, although those terminations are all crystallographically equivalent. This can lead to the existence of a whole range of topologically distinct defects which were created and characterised by the author of this thesis. The presenrtation of these results is not within the scope of this work and the latter can be found elsewhere [6].

III.5 Diffusion Fluxes Associated With Interfacial Defects

As stated in the introduction (chapter 1), there is compelling evidence that defects present at interfaces mediate interfacial processes. In processes such as high-temperature deformation [8], source/sink action [9], and phase transformation [10] , the deformation of polycrystalline materials caused by the motion of interfacial defects may involve a flux of material [11]. In this work, these deformational and diffusional aspects are modelled in terms of the topological properties of the moving defects using

the framework developed by Pond and co-workers and examples are used to illustrate the method (see III.3).

III.5.1 Step heights

Interfacial line-defects are characterised topologically by both their Burgers vector, **b**, and their step height, h. The Burgers vector of a dislocation is invariant with line-direction and the orientation of the interface plane, whereas the step height is invariant in a given plane [7]. The Burgers vector is associated with deformation but both **b** and h are relevant to diffusion fluxes. On a free surface of a single crystal, denoted by its outward pointing unit normal **n**, a step can arise as depicted in Fig 3.8. As indicated schematically on this figure, the adjacent regions are related by a translation vector of the crystal (**I**,**t**) which is not parallel to the surface. The height of the step is given by h=**n**.**t**, and its motion would lead to crystal growth or evaporation of material involving a flux. The step may be imagined to result from the emergence of a dislocation with Burgers vector **b**=**t** onto the surface as indicated. Note that step heights are scalar quantities which may imply positive or negative values (the step illustrated in Fig 3.8 is negative).

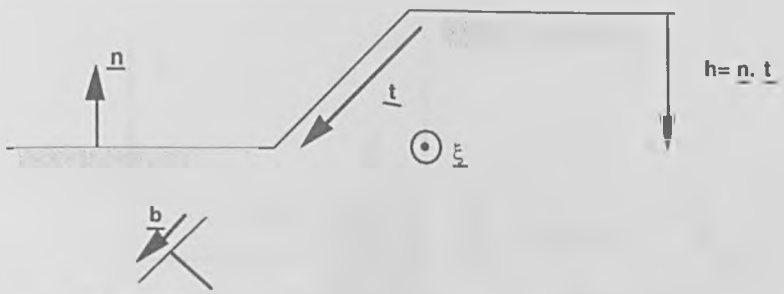

Fig 3.8: Schematic illustration of a surface step showing the definition of **t**,**n** and h; the step could be formed by emergence at the surface of a crystal dislocation with **t**=**b**.

When considering interfacial dislocations, a unique interfacial unit normal **n** is taken to point into the white crystal as illustrated in Fig 3.9 . The step heights associated with the two surfaces to be joined are given by $h(\lambda)=\mathbf{n}.\mathbf{t}(\lambda)$ and $h(\mu)=\mathbf{n}.\mathbf{P}\mathbf{t}(\mu)$ for the white and black crystals respectively, expressed in the white frame (λ).

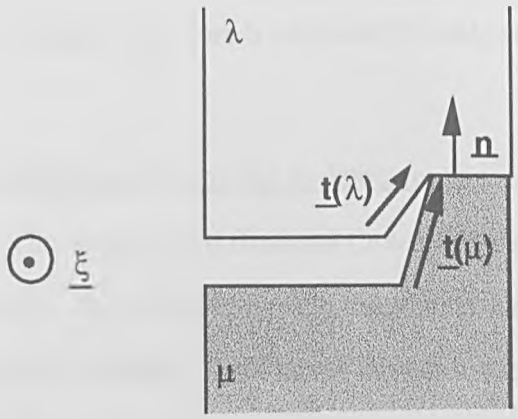

Fig 3.9: Schematic illustration of non-complementary steps

Joining the two surfaces depicted in Fig 3.9 so that the interfacial structures are identical on either side of these perturbations (degenerate interface) introduces a dislocation characterised by **b**, given by equation (3.2). The magnitude of the normal component of **b**, designated b_z, is equal to the difference between the two step heights, i.e. $h(\lambda)$-$h(\mu)$. Hirth and Pond [6] showed that it is useful to define an overlap step height, representing the extent of material overlap normal to the interface when the adjacent crystals are placed together to bond the surfaces, as depicted schematically in Fig 3.10.

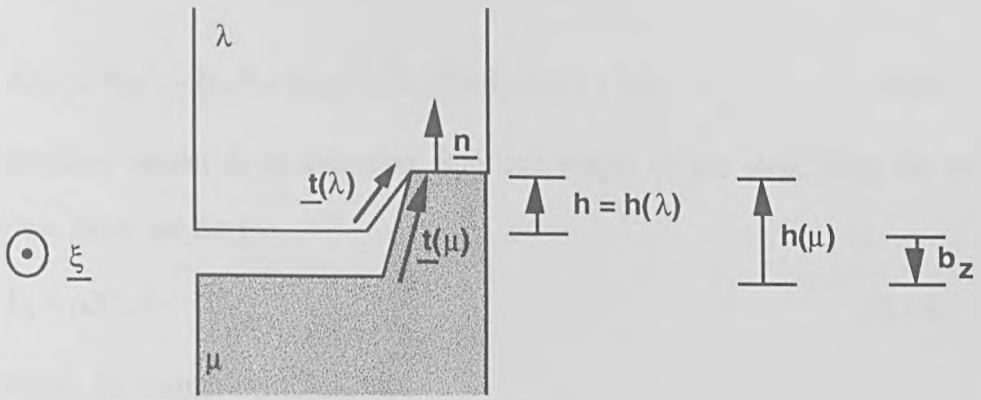

Fig 3.10: Schematic illustration of misfitting steps on juxtaposed black and white crystals to show the definition of b_z and the "overlap" step height, h .

For such an overlap to exist $h(\lambda)$ and $h(\mu)$ must have the same sign; the magnitude and sign of h is then that of the smaller of the two surface steps. Both steps in Fig 3.10 are

positive and $h(\lambda)<h(\mu)$; therefore $h = h(\lambda) = \mathbf{n}.\mathbf{t}(\lambda) = h(\mu) + b_z$. Note that b_z is antiparallel to **n**.

III.5.2 Diffusional fluxes due to defect motion

The analysis of diffusional fluxes associated with defect motion can be facilitated formally by considering the interfacial defect as comprising separate dislocation and step character. To illustrate the latter, the motion of a defect which has no component of **b** parallel to the interface is now considered (see Fig 3.11). In the case illustrated in Fig 3.11, $h = h(\lambda)$ is positive, and b_Z is negative since it is anti parallel to **n**. For an advance of the defect by δy, Hirth and Pond [6] showed that the volume change associated with the step portion for unit length of defect is

$$\delta V = h\delta y \qquad (3.8)$$

The (λ) crystal is assumed to comprise atomic species A, B, C... with X_A^{λ}, X_B^{λ}, X_C^{λ}... atoms of A, B, C... per unit volume respectively, and similarly for the (μ) crystal. The change in the number of A atoms in the volume swept is

$$\Delta N_A = N_A^{\lambda} - N_A^{\mu} = (X_A^{\lambda} - X_A^{\mu})h\delta y = \Delta X_A\, h\delta y \quad . \qquad (3.9)$$

For a diffusion current I_A in atoms/sec into unit length of the step, with the step velocity $v = dy/dt$, we have

$$I_A = \Delta X_A\, hv \quad , \qquad (3.10)$$

and similarly, for components B, C etc.

For the dislocation part, the flux is produced by the normal component b_z, which is negative for the example of Fig. 3.11(c). Hence the volume of (μ) removed by dislocation motion per unit length is

$$\delta V = b_z\, \delta y \quad . \qquad (3.11)$$

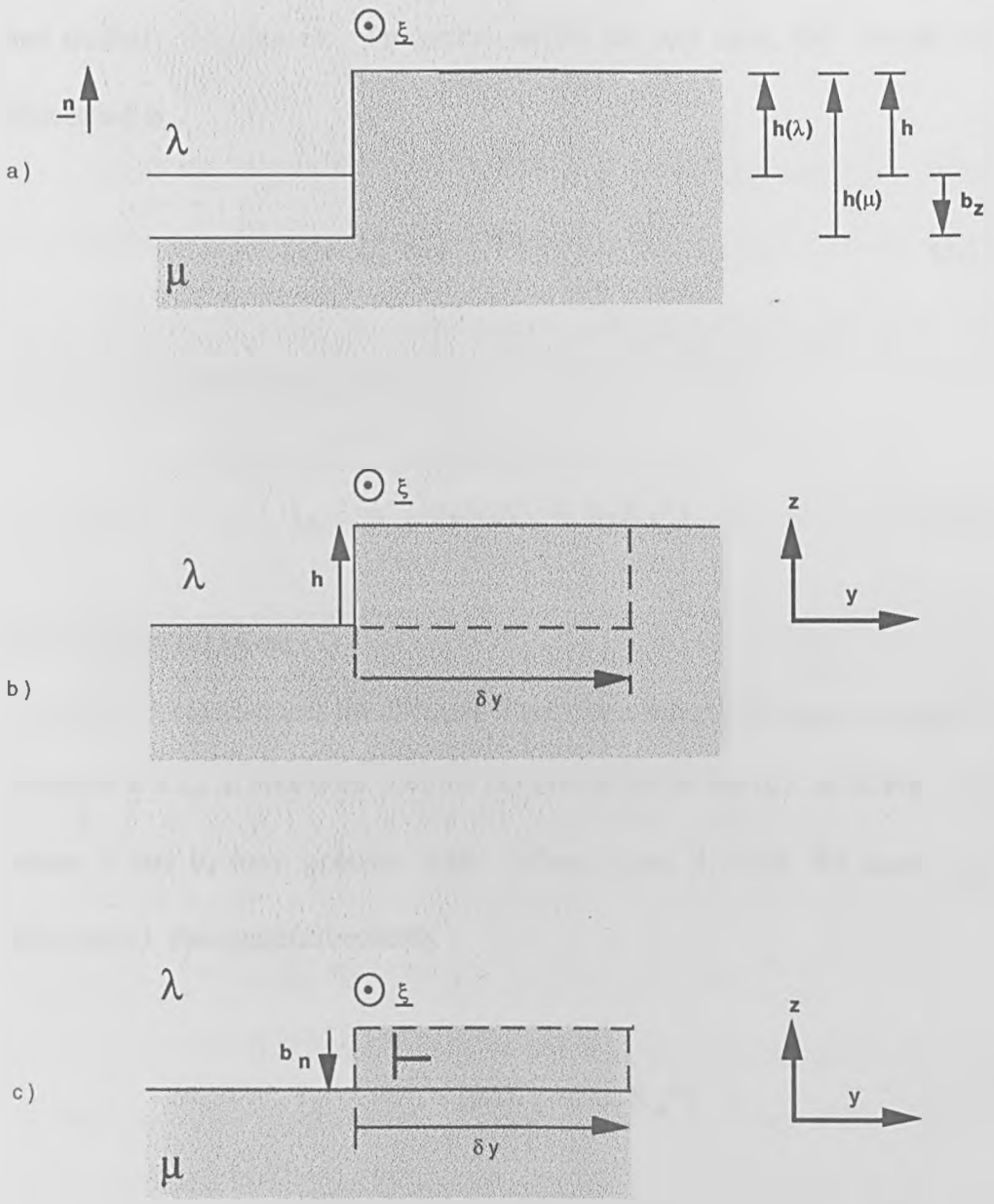

Fig 3.11: (a) Schematic illustration of the step and dislocation components of an interfacial line-defect with no component of b parallel to the interface, (b) volume of material to be transformed from black to white by motion of the step portion by δy , (c) volume of black material to be evaporated by motion of the dislocation portion by δy.

In this case no (λ) phase is created so

$$\Delta N_A = X_A^{\mu} b_z \delta y \quad , \tag{3.12}$$

and similarly for ΔN_B etc. Proceeding as for the step case, the current into the dislocation is

$$I_A = X_A^{\mu} b_z v, \tag{3.13}$$

and the total current into the defect is

$$I_A = v[h\Delta X_A + b_Z X_A{}^{\mu}] \quad , \tag{3.14}$$

and similarly for I_B etc.

Equation (3.14) describes the diffusive fluxes for a defect moving to the right (i.e. the direction $\mathbf{n} \times \xi$) in interfaces with the (λ) crystal above the (μ), as in Fig. 3.11, and where h and b_z have opposite signs. When h and b_z have the same sign (i.e. $h(\lambda)>h(\mu)$), the equation becomes

$$I_A = v[h\Delta X_A + b_Z X_A{}^{\lambda}] \quad , \tag{3.15}$$

and similarly for I_B etc. The senses of the fluxes embodied in equations (3.14) and (3.15) in terms of λ/μ material removal and transformation are summarised in Table 1. The symbol $X_A{}^{\lambda/\mu}$ is used to represent the concentration in a general expression of equation (3.14), and reference to Table 1 enables the appropriate concentration to be identified. When the two steps have opposite signs, no overlap exists (i.e. h = 0), and the flux of A is given by

$$I_A = v[h(\lambda)X_A^{\lambda} - h(\mu)X_A^{\mu}] \quad , \qquad (3.16)$$

and similarly for I_B etc.

We note that expressions (3.14), (3.15) and (3.16) for material fluxes to moving interfacial defects are independent of ξ. However, if the interface plane changes, i.e. **n** changes, then both h and b_z, and hence the flux associated with movement may change.

Table 1.Material fluxes and transformation associated with defect motion parallel to **n** x ξ

h	b_z	Dislocation Portion	Step Portion
+	-	μ removal	$\mu \rightarrow \lambda$
+	+	λ addition	$\mu \rightarrow \lambda$
-	+	μ addition	$\lambda \rightarrow \mu$
-	-	λ removal	$\lambda \rightarrow \mu$

III.5.3 Diffusional fluxes for interfacial defects in grain boundaries

In this section, the flux theory derived above is applied to interfacial defects in grain boundaries and the implications of expression 3.14 are then discussed. The flux arising due to the motion of dislocations in the bulk of single crytals is first presented and the case involving grain boundaries is then considered.

a) Dislocation motion in single crystals

Consider unit length of a straight dislocation moving in the bulk of a single crystal with a velocity **v**. If the Burgers vector, **b**, is inclined to the plane of movement defined by the line direction, ξ, and **v**, a flux of material will be associated with the motion. If the component of **b** perpendicular to this plane of motion is b_z then the atomic flux of species A per unit length of dislocation is given by:

$$I_A = vb_z X_A \quad , \tag{3.17}$$

where X_A is the number of A atoms per unit volume, and similarly for other species present, B, C etc. This result is consistent with expectations as dislocations only climb when their **b** includes a component which does not lie in the plane defined by ξ and **v**.

b) Interfacial defect motion in grain boundaries.

ΔX being zero for all species in grain boundaries, expression (3.14) can therefore be simplified . The step contribution to the flux is always zero because the chemical composition and density of the two grains are identical and its motion does not require a material flux. As a result, equation (3.14) has exactly the same form as equation (3.17) and grain boundary dislocations therefore move by glide if **b** has no normal component, b_z. These conclusions are valid irrespective of whether a defect has step character or not and schematic illustrations of defects which would move by glide and climb respectively are presented in Fig 3.12 (a) and Fig 3.12 (b), inthe case of boundaries between face-centred cubic (f.c.c) crystals for simplicity.

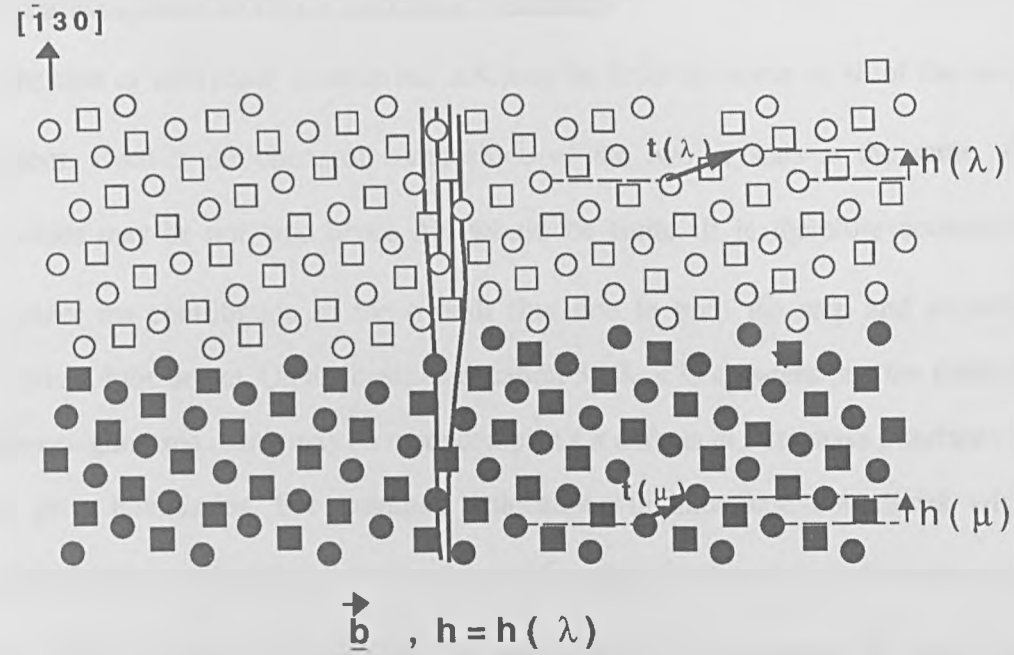

(a)

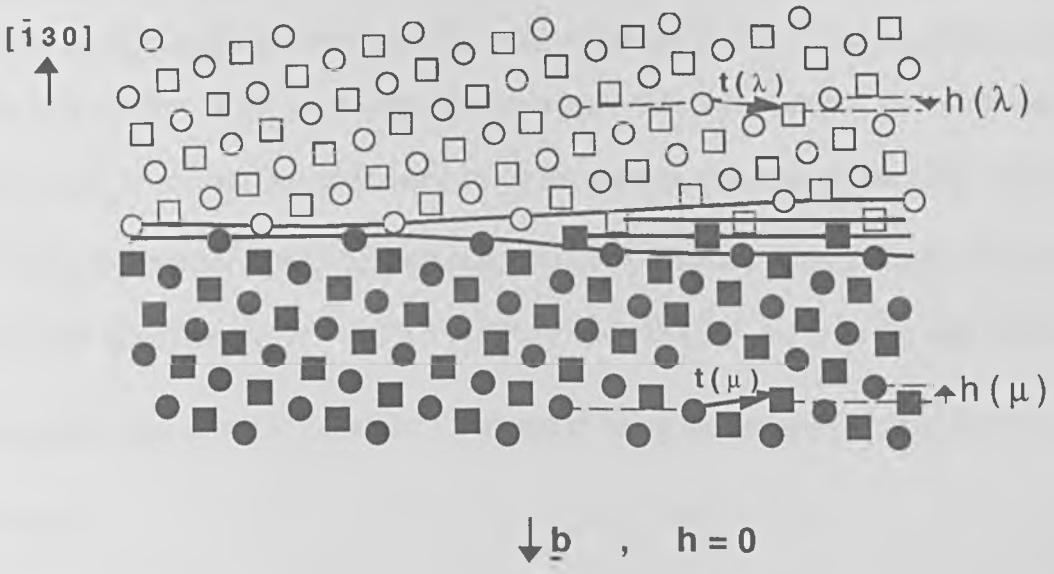

(b)

Fig 3.12: (a) Schematic illustration of glissile edge dislocation in a symmetric $(\bar{1}30)$ tilt boundary between fcc crystals; b=1/10 [310], $h(\lambda)=h(\mu)=h=2d_{(\bar{1}30)}$; (b) a sessile dislocation in the same type of interface; b=1/10 [130], $h(\lambda)=-d_{(\bar{1}30)}$, $h(\mu)=d_{(\bar{1}30)}$, h=0.

c) Interfacial defect motion in interphase boundaries

In the case of interphase boundaries, ΔX may be finite for some or all of the species present. Even if the chemical composition of the two crystals is the same, their densities may be not, and hence ΔX would be finite. It is therefore necessary to consider the contribution to the overall flux due to both the step and dislocation portions of the defect. On the basis of equation 3.13, it is apparent that the distinction between glide and climb may be more complex for defects in interphase interfaces than for grain boundaries. For example, dislocations in interphase boundaries with **b** parallel to the interfacial plane will not move by glide if $h\neq 0$ and Δx is finite for any of the species present. Conversely, a defect with a component b_z may move conservatively if $h\neq 0$ and the interface is an invariant plane, with the adjacent crystals having the same chemical composition.These points are discussed below with respect to the fcc:hcp martensitic transformation system depicted in Fig 3.7 (see appendix one for a description of the crystallography associated with this system). For simplicity, the λ and μ crystals are considered to be monatomic materials of the same atomic species, but more complex chemical structures could also be treated. If the two crystals have the same density, $X^{\lambda} = 4\Omega^{\lambda} = X^{\mu} = 2\Omega^{\mu}$, where $\Omega^{\lambda} = (a^{\lambda})^{-3}$ and a^{λ} is the cubic lattice parameter, and $\Omega^{\mu} = \{(3^{1/2}/2)(a^{\mu})2c^{\mu}\}^{-1}$, a^{μ} and c^{μ} being the hexagonal parameters; thus $\Delta X = 0$.

During martensitic transformation, interfacial defects are thought to move along the interface and according to the formulation presented here, these would be expected to exhibit non-zero overlap step heights h, and non-zero **b** in order that transformation and deformation occur simultaneously. However, such transformations are diffusionless and the present formulation should therefore predict this result for the combined step/dislocation motion. First, a defect with normal component **b** equal to b_z and a step height h is considered to move along an interface where the crystals are

related by an invariant-plane strain. If the interfacial area per atom of species A is designated g_A, the conservation of matter requires that the number of A atoms in corresponding volumes of the λ and μ crystals must be equal; i.e.,

$$h(\lambda)g_A\ X_A^{\lambda}=h(\mu)g_A\ X_A^{\mu} \quad . \tag{3.18}$$

Expression 3.18 provides a second relationship between h(λ) and h(μ) and we therefore have the following set of equations

$$h(\lambda)\text{-}h(\mu)=b_z \text{ (see II.5.1)} \tag{3.19}$$

and, from equation 3.18),

$$h(\lambda)\ X_A^{\lambda}=h(\mu)\ X_A^{\mu}. \tag{3.20}$$

Thus, for the case depicted in Fig 3.11, where h=h(l) , and combining equations 3.19 and 3.20, we have

$$b_z = \frac{h\Delta X_A}{X_A^{\mu}} \tag{3.21}$$

and substituting of this value for b_z into expression 3.14 yields $I_A=0$, and similarly for other species if present. Thus, in the special circumstance of an invariant-plane-strain, the fluxes due to the step and dislocation terms in equation 3.14 are equal and opposite so that the total diffusive flux for the combined step/dislocation is zero. The defect illustrated in Fig 3.13 depicts the situation where the density of the l and m crystals are identical. It is clear from this diagram that h(λ)=h(μ) and therefore b_z =0. However, the "overlap" step h defined earlier is equal to $2d_{(111)}$ (see Fig 3.13).On substitution of this value for b_z into expression (3.14), we find that I_A=0 . Because the step and dislocation terms in equation (3.15) are identically zero, the resulting total flux is also zero.

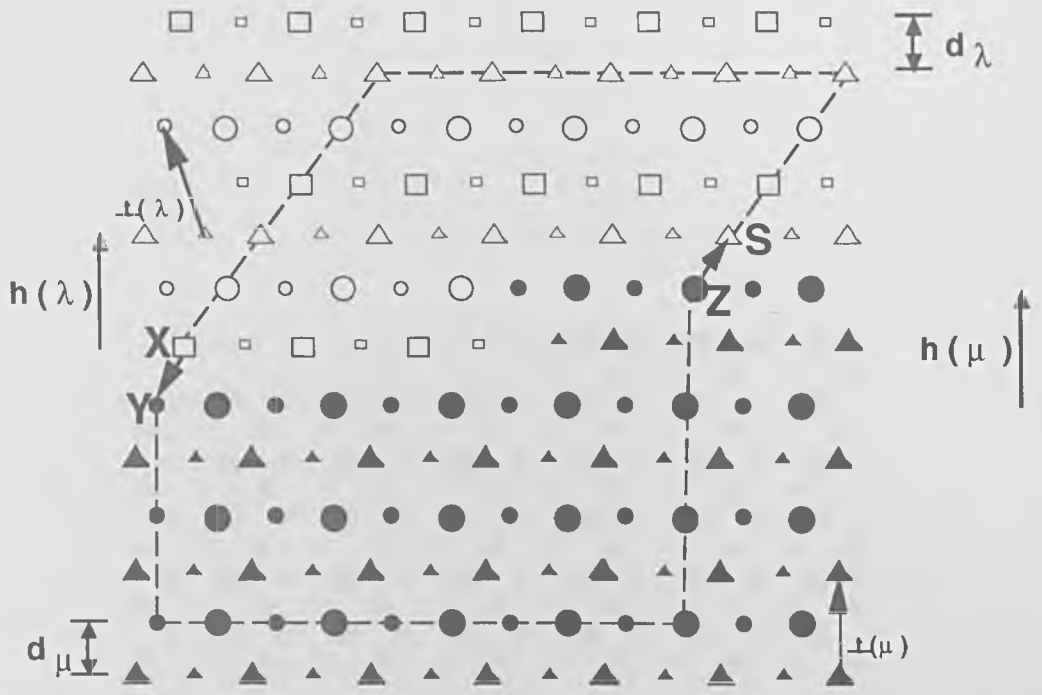

Fig 3.13: Illustration of the step heights h(λ) and h(μ) for the defect illustrated in Fig 3.7

The defect depicted in Fig 3.14 is similar to that in Fig 3.13 except that the density of the black crystal has been doubled by halving the spacing of the $(0002)^{\mu}$ planes, i.e., $X_A^{\mu} = 2\ d_{(111)}$ and hence $\Delta X = -\ X_A^{\lambda}$. The normal component of this change is that **b** now has a (positive) normal component, $b_z = d_{(111)}$, and the overlap step height is reduced to $h = d_{(111)}$. Substituting these values into equation (3.16) for the present case yields

$$I_A = v\left(h\Delta X_A + b_z X_A^{\lambda}\right) = v\left(-d_{(111)}X_A^{\lambda} + d_{(111)}X_A^{\lambda}\right) = 0 \qquad (3.22)$$

as required. Thus, motion of defects like that in Fig 3.14 would cause simultaneous diffusionless transformation and a shape change including components parallel and perpendicular to the interface.

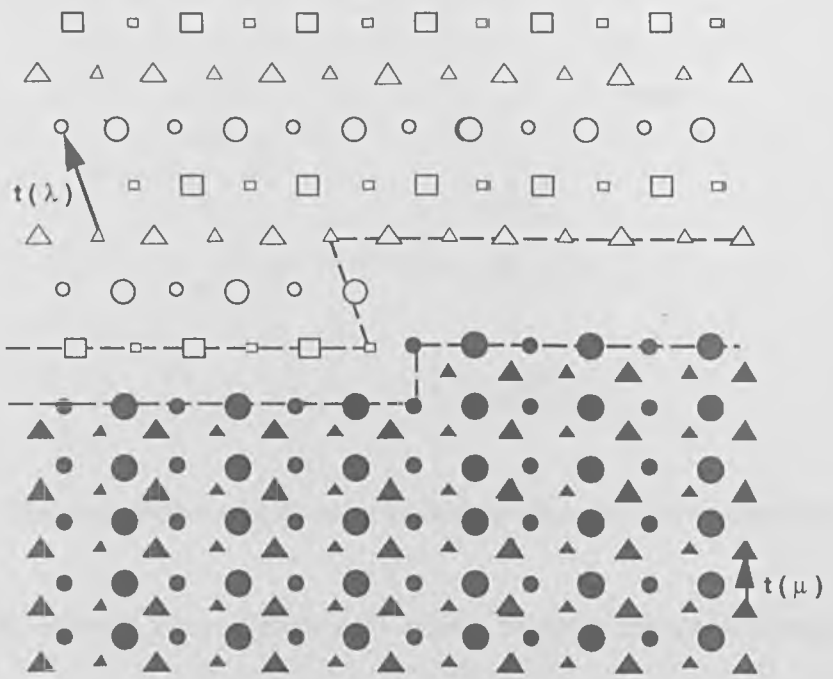

Fig 3.14 : Schematic illustration similar to Fig 3.12(a) except that the black crystal has had its density doubled by halving the value C^{μ}.

III.6 Defect Interactions

It is now well established that defect interactions provide mechanisms for processes which affect material properties dramatically. Several defects may be interacting in complex processes and this section only treats the diffusive flux associated with two interacting defects as an introduction to more general situations .

III.6.1 Interaction of two straight defects

Imagine two straight interfacial defects, α and β, with topological parameters expressed as $\mathbf{b}^{\alpha} = [\, b_x^{\alpha}, b_y^{\alpha}, b_z^{\alpha} \,]$, h^{α} and $\mathbf{b}^{\beta} = [\, b_x^{\beta}, b_y^{\beta}, b_z^{\beta} \,]$, h^{β} , as depicted in Fig 3.15. Let us also consider the total amount of material N_A etc., associated with interactive defect motion rather than the fluxes I_A etc. defined by expression (3.14).

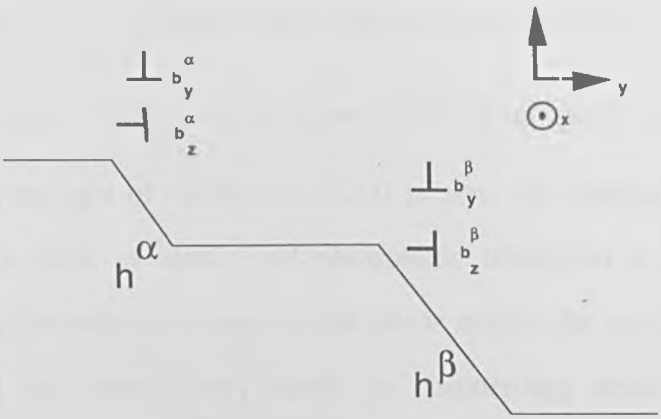

Fig 3.15: Schematic illustration of the two interfacial defects, a and b, before interaction

Let defect α undergo a lateral motion y^{α} which involves interactive motion through defect β, for which the lateral motion is y^{β}. Now steps can move through each other without fluxes arising in addition to those associated with their lateral motion, and similarly for dislocations. However, the dislocation component of α has to climb up (or down) the step component of β and vice-versa. Thus, the total number of A atoms required in the interaction per unit length of the dislocations is given by

$$N_A = \left(h^{\alpha}\, y^{\alpha} + h^{\beta}\, y^{\beta}\right) \Delta X_A + \left(b_z^{\alpha}\, y^{\alpha} + b_z^{\beta}\, y^{\beta}\right) X_A^{\lambda/\mu} + \left(\, b_y^{\beta}\, h^{\alpha} - b_y^{\alpha}\, h^{\beta}\right) X_A^{\lambda/\mu}, \tag{3.23}$$

and similarly for the other species present N_B, N_C etc. The first term on the right of equation (3.23) represents the flux due to the lateral motion of the α and β steps. The second term represents the climb of the α and β dislocations due to their lateral motion. The third term represents the climb of the α dislocation up (or down) the β step, and similarly for the β dislocation and the α step. Note that the sign of the two terms in this bracket is opposite, because, whereas the α defect moves left-to-right

with respect to the β, the β defect moves right-to-left with respect to α. Again, for grain boundaries, this equation is simplied as $\Delta X=0$ for all species present and hence the first term on the right of expression (3.23) is zero. Of course, other aspects of defect interaction, such as elastic and electrostatic interaction would need to be considered for a comprehensive analysis but this is outside the scope of this section. Equation (3.23) has proved very useful in charaterising defect interactions in martensite formation for example [7].

References

1 Volterra, V., *Ann.Sci.Ecole Normale Superieure Paris* **24** (1907) p401.

2 Frank F.C., *Phil. Mag.A*, **42**, p809 (1951).

3 Shubnikov A.V., Koptsik V.A., *Symmetry in Science and Art* (Plenum, New York) 1977.

4 Pond R.C, in *Dislocations and properties of Real Materials*, Ed. M.H.Loretto (Inst. of Metals, London,1985), p71.

5 Hahn, T., Ed. *International Tables for Crystallography* (Reidel, Dordrecht, 1983).

6 Hirth J.P, Pond R.C, *Metall Mater Trans A*, **25**, p.1885 (1994).

7 Pond R.C., Sarrazit F., *Interface Science*, **4**, p99 (1996).

8 G.R.Kegg, C.A.P. Horton, and J.M.Silcock, *Phil Mag*, **17**, p1041 (1973).

9 A.H.King and D.A.Smith, *Metal.Sci.*, **14**, p57 (1980).

10 G.C. Weatherly, Acta. Met., **19**, p181 (1971).

11 J.W.Christian, *The Theory of Transformations in Metals and Alloys* (Pergamon Press, Oxford), 1975.

Chapter 4

Transmission Electron Microscopy Study of Interfaces

Overview

Transmission electron microscopy provides invaluable contrast and diffraction information which facilitates the characterisation of interfacial structures and has consequently been used extensively in this field. However, the interpretation of such information relies on theories of electron diffraction and treatments which have been found useful are well documented in a number of textbooks for example Hirsch et al. [1]. It is not within the scope of this chapter to give an extensive description of such treatments, however, a background knowledge of the processes involved as well as the parameters which affect the image contrast is provided.

Electron diffraction from a bicrystal can be considerably more complex than diffraction from single crystals and usually requires relatively simple diffracting conditions to be set up experimentally in order to interpret the observed contrast quantitatively. The second part of this chapter reviews the most common contrast effects associated with such imaging conditions and computer simulated images are used to illustrate their main characteristics.

IV.1 The Kinematical Theory Of Electron Diffraction

The kinematical theory of electron diffraction is based on the assumption that the interaction between the crystal and the electrons is weak so that only a small number of incident electrons are thought to be scattered into the diffracted beam. As further scattering of diffracted electrons is neglected, the intensity of the main beam is therefore assumed to be constant as it propagates through the crystal . This theory has the advantage of being relatively simple and has found some successful applications in very thin crystals. However, the assumptions discussed above are rather poor for the analysis of thicker crystals where appreciable interaction between incident and diffracted beams does arise. The dynamical theory overcomes these limitations and is therefore preferred for the analysis of most electron micrographs.

IV.2 The Two-Beam Dynamical Theory

IV.2.1 Basic equations in a perfect crystal

As discussed in the previous section, electron images of materials are normally interpreted in terms of the dynamical theory as the latter accurately describes the diffraction process taking place in the specimen. This treatment accounts for the interaction between scattered and transmitted electrons as well as absorption effects. The simplest form of the dynamical theory considers the amplitudes of only two electron waves T(z) and S(z) corresponding to the transmitted and scattered beams respectively (z representing the depth into the crystal in a direction parallel to the incident beam). As electrons from the diffracted beam may be scattered back into the transmitted one, a "dynamic exchange" results from the coupling of those two beams as they propagate into the crystal. An approximation, in which this exchange is assumed to take place within a narrow column taken through the crystal in the z direction, is used to describe this phenomenon; no exchange between the beams in adjacent columns is considered. Under such conditions, the coupling in an element dz, at a depth z in a small column of unfaulted material of thickness t (see Fig.4.1), is described by a pair of differential equations known as the Howie-Whelan equations and given below.

$$\frac{d\,T(z)}{d\,z} = \frac{i\,\pi}{\xi_0}\,T(z) + \frac{i\,\pi}{\xi_g}\,S(z)\exp(2\pi i s z), \qquad (4.1)$$

and

$$\frac{d\,S(z)}{d\,z} = \frac{i\,\pi}{\xi_0}\,S(z) + \frac{i\,\pi}{\xi_g}\,T(z)\exp(-2\pi i s z), \qquad (4.2)$$

where s is a measure of the deviation from the exact Bragg angle (known as the excitation error), ξ_g is the extinction distance for the diffracting vector **g**, ξ_0 represents the mean refractive index, **g** is the operating diffraction vector and the

terms exp (2πisz) describe a phase factor arising from the scattering process. The subscripts 'g' and 'o' apply to the diffracted and transmitted waves respectively .

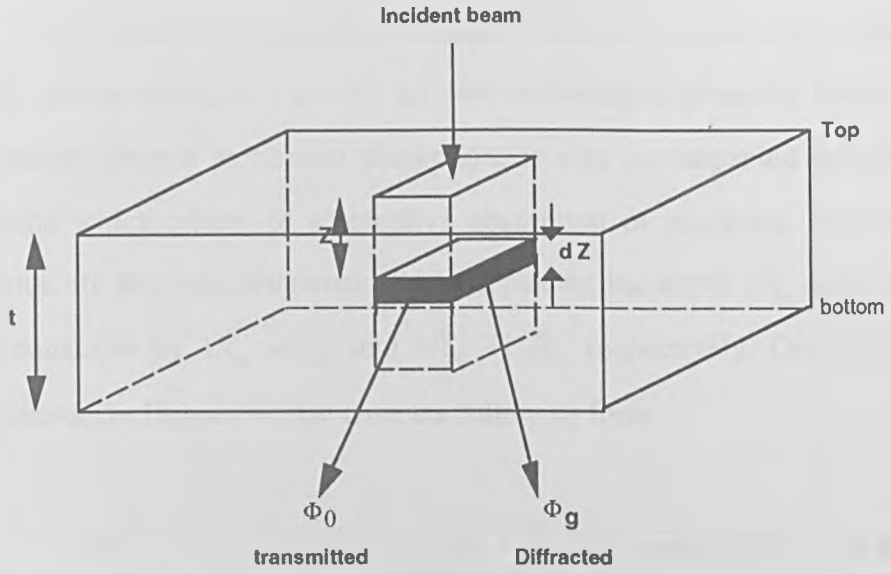

Fig 4.1: Schematic illustration of the column approximation .

IV.2.2 Basic equations in a faulted material

In a column containing a dislocation, equations 4.1 and 4.2 are modified to introduce a phase factor $2\pi\mathbf{g}.\mathbf{R}$ (z) corresponding to the local bending of atomic planes caused by the strain field of the defect. **R**(z) is the displacement field associated with the discontinuity and in the case of dislocations the latter varies continuously throughout the crystal. The Howie-Whelan equations are therefore given by the following expressions

$$\frac{d\,T(z)}{d\,z} = \frac{i\pi}{\xi_0}\,T(z) + \frac{i\pi}{\xi_g}\,S(z)\exp\left(2\pi i s z + 2\pi i\,\mathbf{g}.\mathbf{R}(z)\right), \quad (4.3)$$

and

$$\frac{d\,S(z)}{d\,z} = \frac{i\pi}{\xi_0}\,S(z) + \frac{i\pi}{\xi_g}\,T(z)\exp\left(-2\pi i s z - 2\pi i\,\mathbf{g}.\mathbf{R}(z)\right) \quad (4.4)$$

From the comparison of equations 4.1 with 4.3 (and 4.2 with 4.4), it emerges that the introduction of a defect alters the equation describing the perfect crystal by the term **g.R**(z) in both the transmitted and diffracted beam amplitudes. This aspect forms the

basis of the so-called **g.b** invisibility criterion and the latter will be described further in section IV.3.

IV.2.3 Absorption of electrons

As electrons propagate through the crystal, an overall decrease in intensity corresponding to a loss by inelastic scattering is generally observed. This phenomenon, known as normal absorption, is also accompanied by anomalous absorption which relates to a selective absorption of electrons. Both types of absorption are allowed mathematically by replacing the terms $1/\xi_g$ and $1/\xi_0$ in the above equations by $1/\xi_g + i/\xi_g'$ and $1/\xi_0 + i/\xi_0'$ respectively. On making these substitutions, the Howie-Whelan have the following form

$$\frac{d\,T(z)}{d\,z} = i\pi\left(\frac{1}{\xi_0}+\frac{i}{\xi_0'}\right) T(z) + i\pi\left(\frac{1}{\xi_g}+\frac{i}{\xi_g'}\right) S(z)\exp\left(2\pi i s z + 2\pi i \mathbf{g}.\mathbf{R}(z)\right) \tag{4.5}$$

and

$$\frac{d\,T(z)}{d\,z} = i\pi\left(\frac{1}{\xi_0}+\frac{i}{\xi_0'}\right) S(z) + i\pi\left(\frac{1}{\xi_g}+\frac{i}{\xi_g'}\right) T(z)\exp\left(-2\pi i s z - 2\pi i \mathbf{g}.\mathbf{R}(z)\right) \tag{4.6}$$

where ξ_0 and ξ_g' are the parameters introduced to take account of absorption effects. Another set of equations, used for contrast calculations, may be obtained by multiplying the complex wave amplitudes S(z) and T(z) by suitable factors as follows

$$T'(z) = T(z)\exp\left(-\frac{\pi i z}{\xi_0}\right) \tag{4.7}$$

$$S'(z) = S(z)\exp\left(2\pi i z - \frac{\pi i z}{\xi_0} + 2\pi i \mathbf{g}.\mathbf{R}(z)\right) \tag{4.8}$$

This substitution leads to another pair of differential equations related to the original ones by a phase factor which depend on z ; these are

$$\frac{d\,T'(z)}{d\,z} = \left(\frac{-\pi}{\xi_0'}\right) T'(z) + \pi i \left(\frac{1}{\xi_g} + \frac{i}{\xi_g'}\right) S'(z), \tag{4.9}$$

and

$$\frac{d\,S'(z)}{d\,z} = \pi i \left(\frac{1}{\xi_g} + \frac{i}{\xi_g'}\right) T'(z) + S'(z) \left(\frac{-\pi}{\xi_0'} + 2\pi i s + 2\pi i \frac{d(\mathbf{g}.\mathbf{R}(z))}{dz}\right) \tag{4.10}$$

The strain field of the defect enters equation (4.10) as **g**. d**R**(z)/dz and represents the local bending of crystal planes discussed earlier [1]. Finally, equations 4.9 and 4.10 may be re-expressed in a unit of length equal to ξ_g/π by substituting the variable z for another variable Z (where $Z=\frac{z\pi}{\xi_g}$), which gives

$$\frac{d\,T'(Z)}{d\,Z} = \left(\frac{-\xi_g}{\xi_0'}\right) T'(Z) + \left(i - \frac{\xi_g}{\xi_g'}\right) S'(Z), \tag{4.11}$$

and,

$$\frac{d\,S'(Z)}{d\,Z} = \left(i - \frac{\xi_g}{\xi_g'}\right) T'(Z) + S'(Z) \left(\frac{-\xi_g}{\xi_0'} + 2is\xi_g + 2\pi i \frac{d(\mathbf{g}.\mathbf{R}(Z))}{dZ}\right) \tag{4.12}$$

Equations 4.11 and 4.12 are now in the form used for contrast simulations [2]

The term $\frac{\xi_g}{\xi_0'}$ denotes the apparent absorption mentioned earlier whereas $\frac{\xi_g}{\xi_g'}$ represents the anomalous absorption $\mathcal{A}$. The dimensionless term $s\xi_g$ represents a measure of the deviation from the Bragg angle and is denoted w. d(**g**.**R** (Z))/dZ is designated $\mathbf{B}_g'(Z)$ and correponds to an increase in the excitation s due to the presence of a defect. It should be noted that the substitution of T' (z) and S' (z) for T(z) and S(z) respectively, introduces a phase difference which can be neglected in contrast computer simulation as one is interested in the intensity of the electron waves at the bottom of each column, not in their amplitudes.

IV.3 The "g.b = 0" Criterion for Grain Boundaries

The so called "**g.b** = 0" technique has been widely used for the determination of Burgers vectors associated with the observation of dislocations in single crystals. Provided that only two beams are excited the Howie-Whelan equations defined in 4.12 imply that dislocations vanish when $\mathbf{B}_g'(z) = 0$. In elastically isotropic materials this condition is satisfied when **g.b** = 0 for screw dislocations, and when **g.b** and **g.b** x **u** = 0 for edge dislocations; **u** being a unit vector parallel to the dislocation line and **b** the Burgers vector of the defect. However, the above is not always true in anisotropic materials and the method may therefore not be reliable for identification of Burgers vectors in such materials. Another limitation to the use of this technique is associated with its rather poor resolution when dislocations having Burgers vectors of small magnitude have to be imaged (Pond [3]). As explained in Chapter 2, interfacial dislocations are often non-crystal dislocations whose Burgers vectors are usually small and the method should therefore be used with caution for the reasons given above. A matching technique, based on the theoretical simulation of micrographs from the integration of equations is therefore the preferred technique for the identification of interfacial defects.

IV.4 Weak-Beam-Dark-Field Imaging

In weak-beam-dark-field mode, the specimen is tilted so that a high-order diffraction spot is excited (e.g. 3**g**, 4**g**) and a dark-field image is then taken with an operating reflection such as -**g** for which the parameter s is fairly large. Under such conditions, the width of the defect is narrower and better resolution is therefore achieved. Under dynamical diffracting conditions and disregarding absorption effects, the diffracted and transmitted beam intensities are given by

$$I_g(z) = \frac{1}{1+w^2} \sin^2\left(\frac{\pi z}{\xi^{eff}}\right), \qquad (4.13)$$

and

$$I_0(z) = \left(1 - I_g(z)\right) \qquad (4.14)$$

respectively, where Z is the thickness down a column in the diffracting grain, ξ^{eff} is the effective extinction distance (periodicity with which the two bloch waves beat together), and w is the deviation parameter defined earlier.

The effective exctinction distance is given by $\xi^{eff} = \frac{\xi_g}{\left(1+s^2\,\xi_g^2\right)^{1/2}}$ and decreases as s increases. Since the width of a dislocation is related to approximatively ξ^{eff} / 3, using large values of s results in a narrower image of most defects.

Fig.4.2 illustrates the main steps followed to obtain a weak beam image.

IV.5 Experimental Imaging Conditions

As stated earlier, electron diffraction from a bicrystal can be very complicated due to the relative crystallographic orientation of the constituent crystals. On crossing the interface, each of the beams excited in the upper crystal may give rise to further beams in the lower grain and these are coupled to an extent which depends upon the crystallographic relationship between the constituent crystals. A detailed interpretation of the micrograph may therefore be difficult unless relatively simple diffraction conditions are set up experimentally. Pond [4] reviewed the main diffracting conditions that have been found useful in the study of interfacial structures and these are briefly discussed below.

Fig 4.2: Schematic illustration of the weak beam dark field technique.

IV.5.1 Two-beam diffraction in one grain

The simplest imaging condition that may be set up experimentally consists in orientating the specimen so that one grain is set into a strong two-beam condition (generally using a low-order reflection) while negligible diffraction is maintained in the other grain. Either the upper (λ) or lower (μ) crystal may be oriented for strong diffraction (see Fig.4.3 (a) and (b)) and each situation generally leads to a different contrast. In what follows, the grain first irradiated by the incident beam is referred to as upper, and beam $\mathbf{g}_{\lambda/\mu}$ designates the diffracted beam having $\mathbf{g}_{\lambda/\mu}$ as its reciprocal lattice vector . The "two-beam in one grain" mode is often selected to determine the topology of interfacial contours but should be used with care for quantitative contrast analysis as weak beams are inevitably excited in the "non-diffracting" grain and these may interact with the operating reflection in the

diffracting crystal. Humble and Forwood [5] identified this problem and recommended the use of the simultaneous two-beam diffraction to overcome this issue.

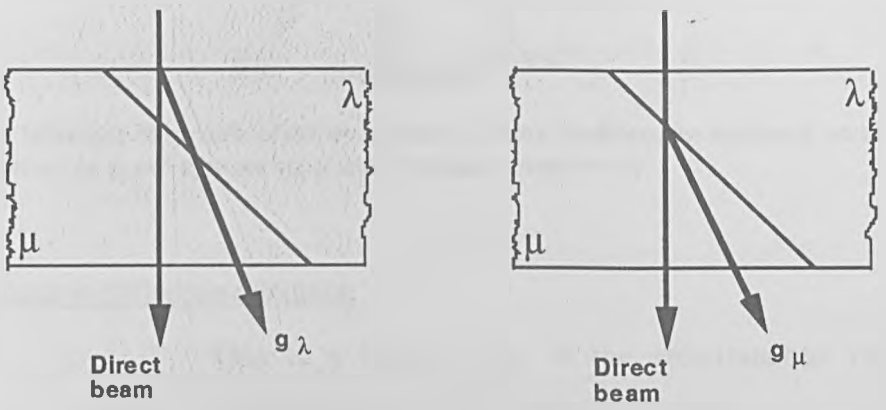

Fig 4.3: Schematic illustration of the 2-beam diffraction mode; (a) the upper crystal λ is diffracting and in (b) the lower one is orientated for strong diffraction.

IV.5.2 Simultaneous two-beam diffraction

This mode is set up by tilting the specimen so that a two-beam diffraction is obtained in one grain using a reflection $\mathbf{g}_\lambda$, and subsequently tilting around an axis parallel $\mathbf{g}_\lambda$ until a two-beam condition, represented by the diffracting vector $\mathbf{g}_\mu$, in the other grain is satisfied (see Fig. 4.4). Best contrast is obtained by choosing diffraction vectors which are orthogonal . Forwood and Humble [6] showed that the main contrast features of images obtained in this mode are governed by strong beams and that weakly coupled beams have little influence. This makes this technique very useful and contrast analysis is generally carried out by comparison with theoretically simulated images.

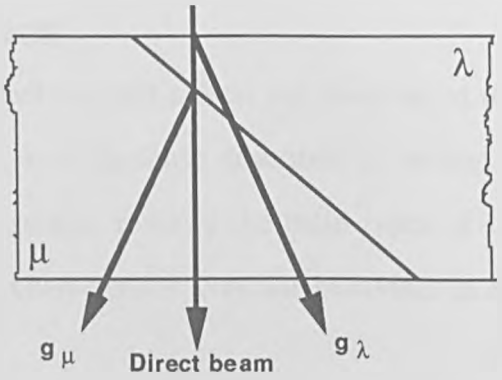

Fig 4.4: Schematic illustration of the simultaneous 2-beam condition; the reciprocal vectors excited are represented by $\mathbf{g}_\lambda$ and $\mathbf{g}_\mu$ in the upper and lower grains respectively.

IV.5.3 Same **g** diffraction condition

This is a special case of the simultaneous two-beam diffraction condition discussed above in which the sets of diffracting planes have identical spacings and orientation in the two crystals (see Fig. 4.5) i.e. $\mathbf{g}_\lambda = \mathbf{g}_\mu$. The lattices of the adjacent crystals are then referred to as being correlated. The diffracted beams $\mathbf{g}_\lambda$ and $\mathbf{g}_\mu$ propagate in parallel directions and any offset of the diffracting planes at the interface can be detected.

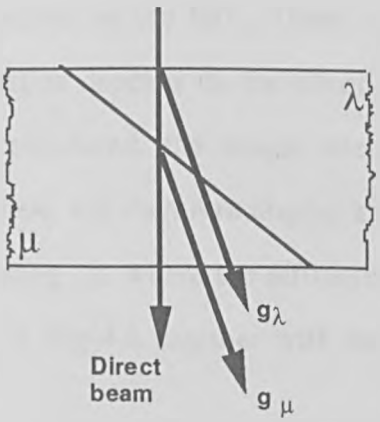

Fig 4.5: Schematic illustration of the simultaneous 2-beam diffraction condition in the case where the lattices of the adjacent grains are correlated.

IV.6 Contrast Effects

Some distinct contrast effects are observed at interfaces where special diffraction conditions, such as those described in section IV.5.3, operate in the adjacent grains. This section reviews the main types of fringes arising at grain boundaries and their characteristic contrast behaviour is illustrated by computer simulated images.

IV.6.1 Thickness fringes

Thickness fringes are commonly observed at grain boundaries inclined to the specimen surface in which one of the constituent grains is diffracting strongly while negligible diffraction is maintained in the other crystal. Under such conditions, the "non-diffracting" grain can be regarded as an amorphous absorber and the bicrystal is therefore effectively a wedge-shaped crystal.

It is clear from equation (4.14) that the diffracted intensity becomes zero for z=0 whereas, as z increases, it oscillates sinusoidally between zero and a maximum value which depends w. Consequently, the bright field (BF) image consists of a set of dark fringes (corresponding to I_0 (z)=0) which run parallel to the intersection of the boundary with the surface of the foil . These connect regions of equivalent thickness and their separation depends on the effective extinction distance. When absorption effects are considered, the fringe intensity becomes damped with increased thickness and these will therefore display a stronger contrast away from the grain which is diffracting i.e. where the diffracting grain is the thinnest. The simulated image shown in Fig 4.6 together with the associated intensity profile illustrates this behaviour .

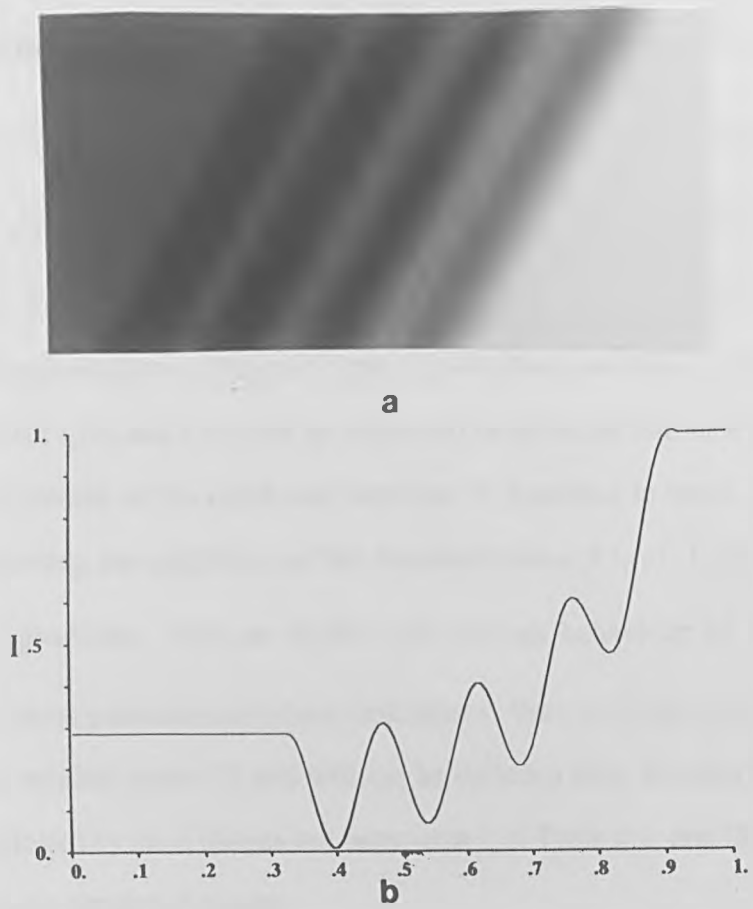

Fig 4.6: (a)Simulated image showing the decrease in thickness fringes intensity away from the diffracting crystal (λ) . (b) Corresponding intensity profile.

IV.6.2 Δ w fringes

Δ w fringes (also called δ fringes) arise at interfaces imaged under the diffracting conditions described in section IV.5.3 and for which the deviation parameter w is different in the two adjacent crystals. Let w be designated by $w_\lambda = s_\lambda \xi_{g\lambda}$ in the upper crystal and similarly $w_\mu = s_\mu \xi_{g\mu}$ in the lower grain. The difference Δw is therefore given by $\Delta w = w_\lambda - w_\mu = s_\lambda \xi_{g\lambda} - s_\mu \xi_{g\mu}$ and will be non-zero if either the extinction distances associated with $\mathbf{g}_\lambda$ and $\mathbf{g}_\mu$ or the excitation errors s_λ and s_μ are different. In other words, Δw is non-zero if either $\xi_{g\lambda} \neq \xi_{g\mu}$ (with $s_\lambda \mathbf{g}_\lambda = s_\mu \mathbf{g}_\mu \neq 0$) or $\xi_{g\lambda} = \xi_{g\mu}$ (with $s_\lambda \mathbf{g}_\lambda \neq s_\mu \mathbf{g}_\mu$).

The contrast exhibited by Δw fringes has been extensively studied by Amelincks [7] in relatively thick specimens for the simple symmetrical case corresponding to $s_\lambda \mathbf{g}_\lambda = -s_\mu \mathbf{g}_\mu$. It was shown that both the diffracted and transmitted beam intensities can be written as the sum of three terms $I_1(z)$, $I_2(z)$ and $I_3(z)$ which have either dominant or neglectable expressions at various depths z into the specimen. For instance, the expressions for $I_1(z)$ and $I_2(z)$ can be neglected close to the entrance surface of the foil and the contrast at this depth can therefore be described in terms of $I_3(z)$ alone. Hence, by plotting the amplitudes of the dominant terms of $I_1(z)$, $I_2(z)$ and $I_3(z)$ as a function of positions , one can deduce the contrast behaviour of Δw fringes by studying extreme positions and phase differences. Details of the calculations can be found in the original paper [7] and will not be included here. However, the principal features exhibited by such fringes are summarised in Table 4.1 and illustrated below using computer-simulated images.

Table 4.1: Characteristics of Δw Fringes

	BRIGHT FIELD		DARK FIELD	
	Top	Bottom	Top	Bottom
Δw ≥0	Bright	Dark	Bright	Bright
Δw < 0	Dark	Bright	Dark	Dark

The observed feature consists of fringes of alternate contrast running parallel to the intersection of the boundary plane with the foil surface. The fringe pattern is asymmetric in bright field (i.e. outer fringes display different contrast) and symmetric in dark field. This effect is illustrated in Fig 4.7 for positive and negative values of Δw. As the sign of Δw determines the nature of the top and bottom of the foil (i.e bright or dark), the boundary plane inclination can then be identified.

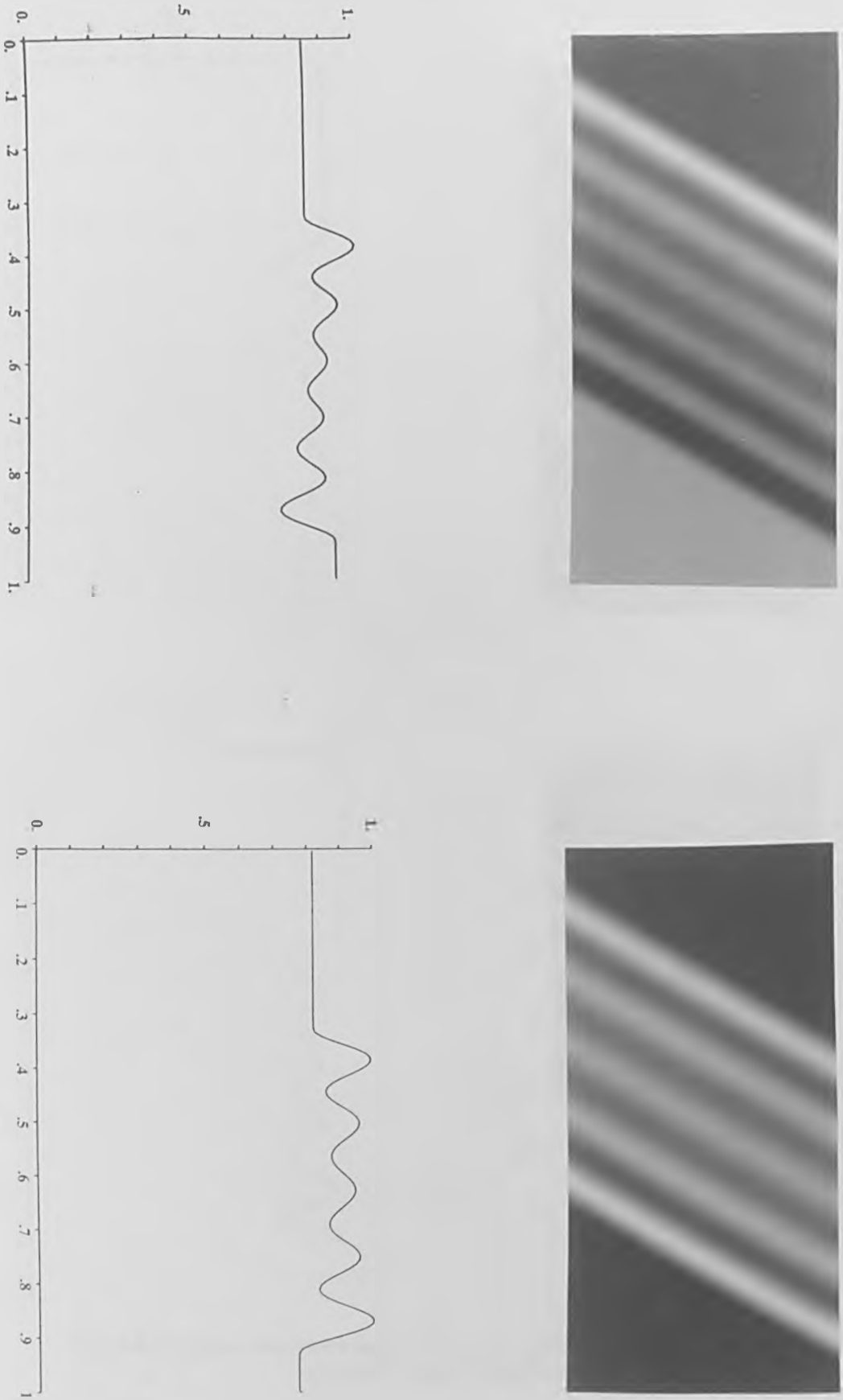

Fig 4.7: Computer-simulated images of Δw fringes and associated intensity profiles.
(a) Δw >0 BF; (b) Δw >0 DF

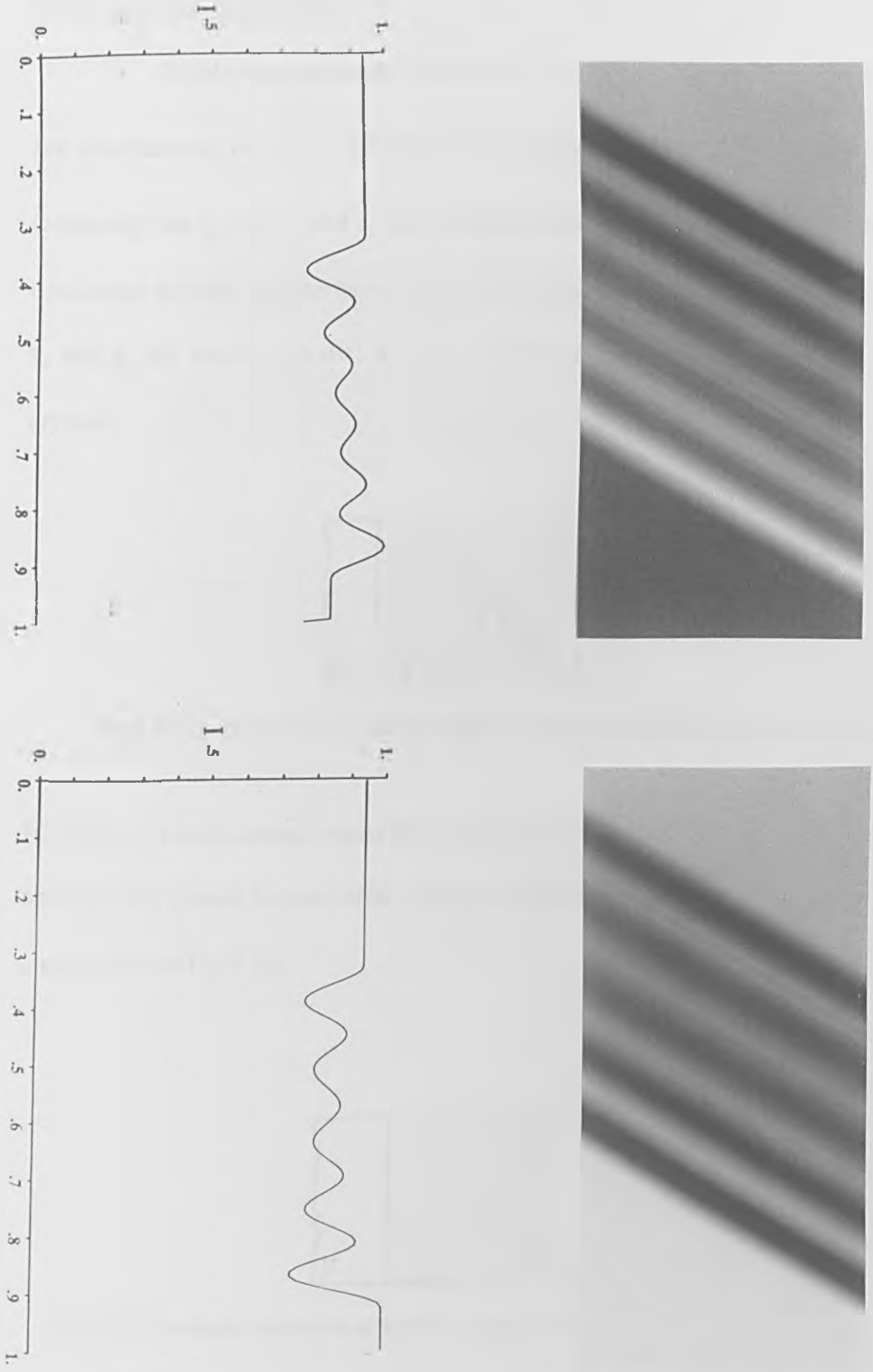

Fig 4.8: Computer-simulated images of Δw fringes and associated intensity profiles. (c) Δw<0 BF and (d) Δw<0 DF.

IV.6.3 Displacement fringes

Displacement fringes (also called α fringes) arise at interfaces oriented for simultaneous two-beam diffraction (see section IV.5.2) for which Δw is zero (assuming that $\xi_{g\lambda} = \xi_{g\mu}$ and $s_\lambda = s_\mu$). If the planes giving rise to the scattering are continuous through the interface (see Fig 4.9) no contrast will be observed provided $\mathbf{g}_\lambda$ and $\mathbf{g}_\mu$ are exactly parallel and have identical interplanar spacing in the two crystals.

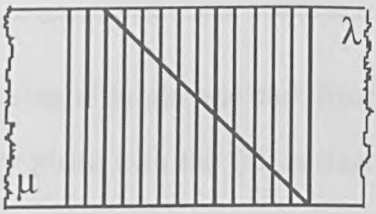

Fig 4.9: Illustration showing diffracting planes being continuous across the interface.

However, if a displacement vector **R** is associated with one of the crystal (the bottom one say) these planes become offset at the interface and a phase factor $\alpha = 2\pi\mathbf{g}_\mu . \mathbf{R}$ is introduced (see Fig 4.10).

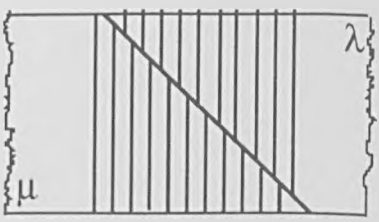

Fig 4.10: Schematic illustration of the offset created by the displacement **R** at the interface.

This factor takes values from zero to 2π, depending on the value **R,** and this alters the observed contrast. The properties of such fringes are very similar to the contrast

displayed by stacking faults and have been investigated by several authors [1]. The same approach as the one discussed in section 5.2 can be adopted to describe the features exhibited by displacement fringes and these are summarised in Table 4.2 and illustrated below.

Table 4.2: Characteristics exhibited by displacement fringes.

	BRIGHT FIELD		DARK FIELD	
	Top	Bottom	Top	Bottom
$\sin\alpha > 0$	Bright	Bright	Bright	Dark
$\sin\alpha < 0$	Dark	Dark	Dark	Bright

The contrast as a whole consists of bright and dark fringes which run parallel to the intersection of the boundary plane with the foil surface. In bright field, the fringe pattern is symmetrical (i.e. outer fringes are both dark or light) whereas it is asymmetric in dark field. This behaviour is illustrated in Figs.4.11and 4.12 for positive and negative values of $\sin\alpha$. The sign of $\sin\alpha$ determines the nature of the outer fringes and, again, this allows the boundary plane inclination to be determined. The set of fringes is invisible for $\mathbf{g}.\mathbf{R}=0$ and when $\mathbf{g}.\mathbf{R}=1/2$, the fringe pattern as a whole is symmetrical about its centre and the fringes are referred to as π fringes (see Fig 4.13). In this case only, the pattern is symmetric in both bright field and dark field.

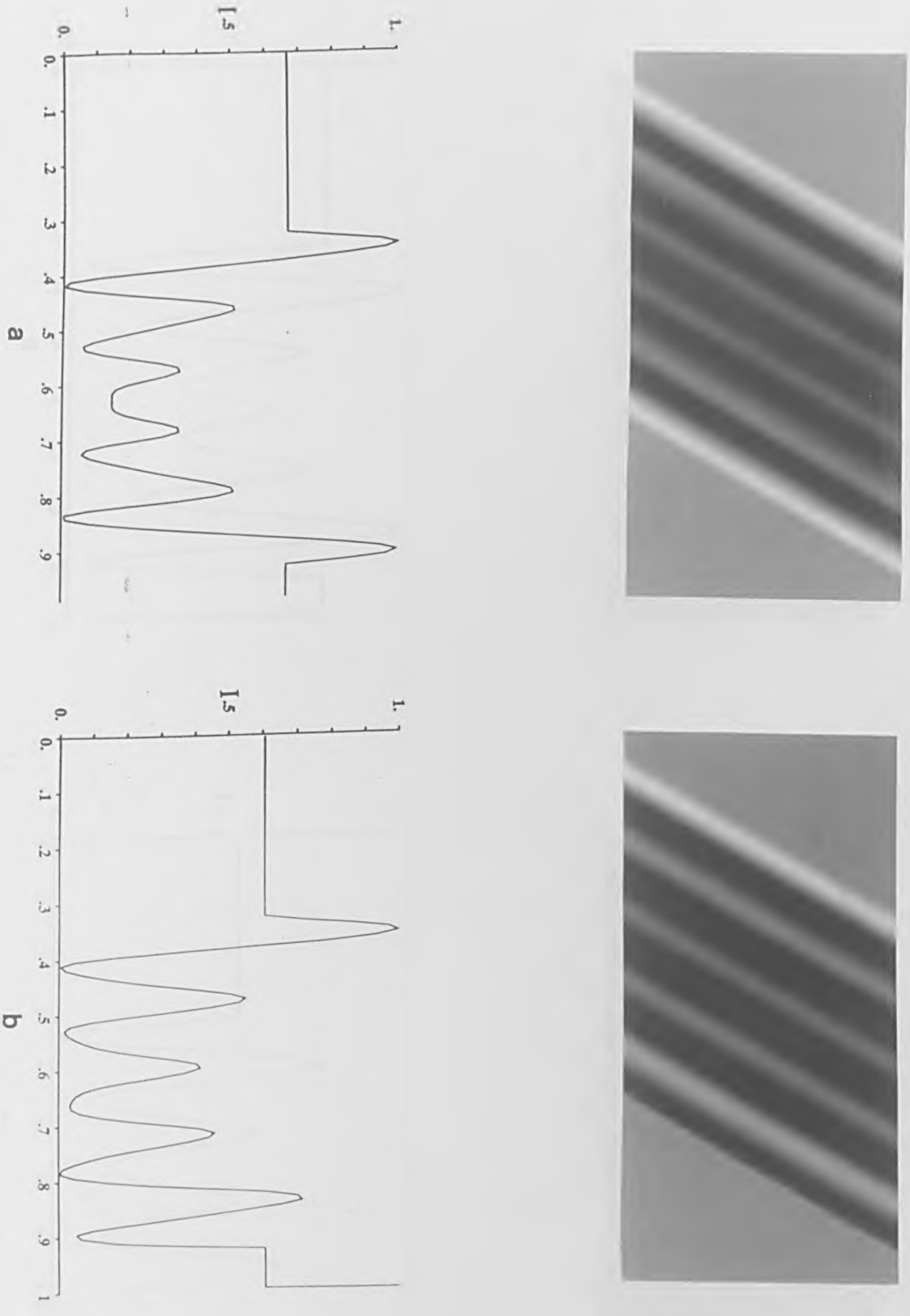

Fig 4.11: Computer-simulated images of displacement fringes and associated intensity profiles for g.R=2/3 and sinα >0. (a) Bright Field image and (b) Dark Field image

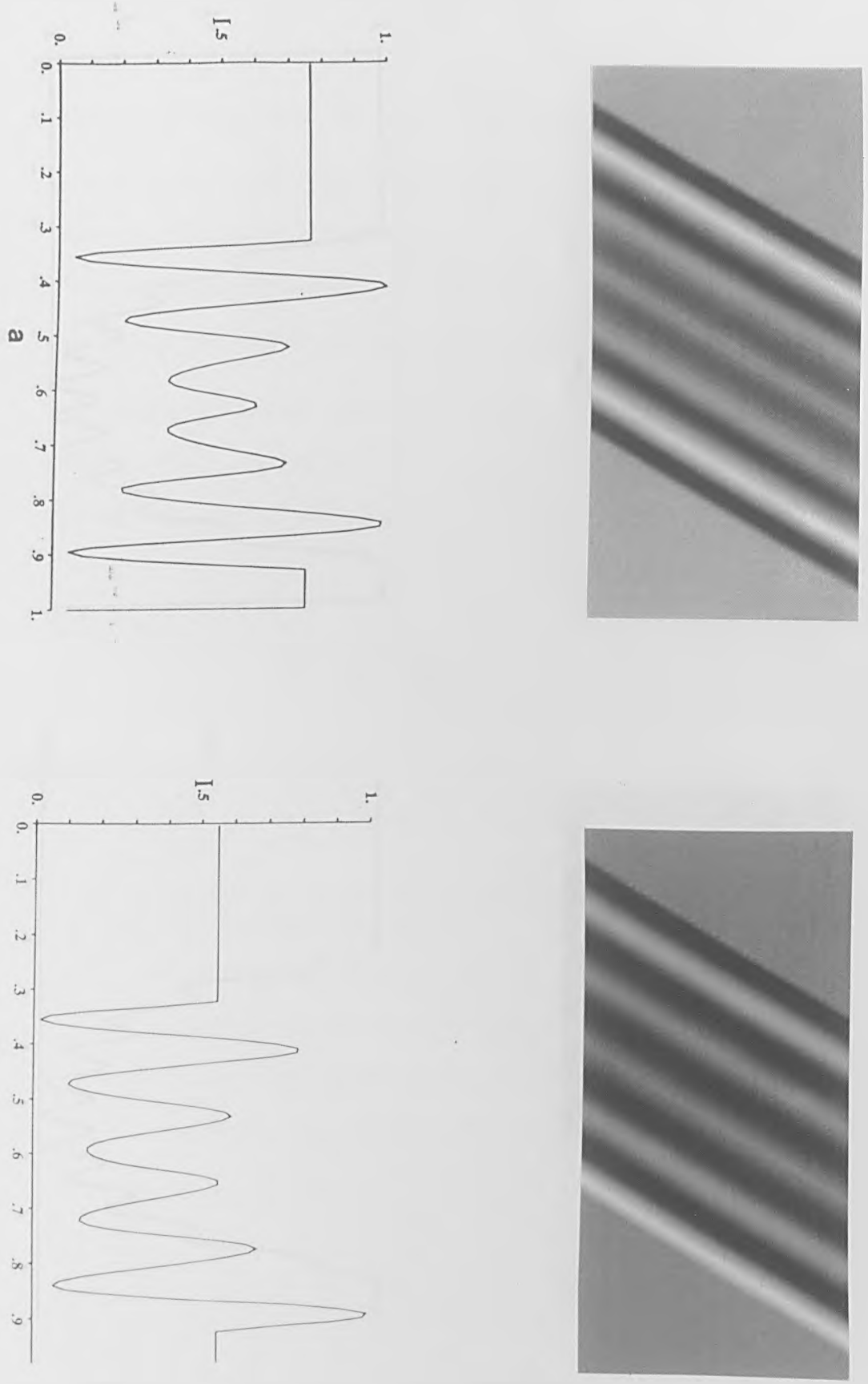

Fig 4.12: Computer-simulated images of displacement fringes and associated intensity profiles for g R=2/3 and sinα <0. (a) Bright Field image and (b) Dark Field image

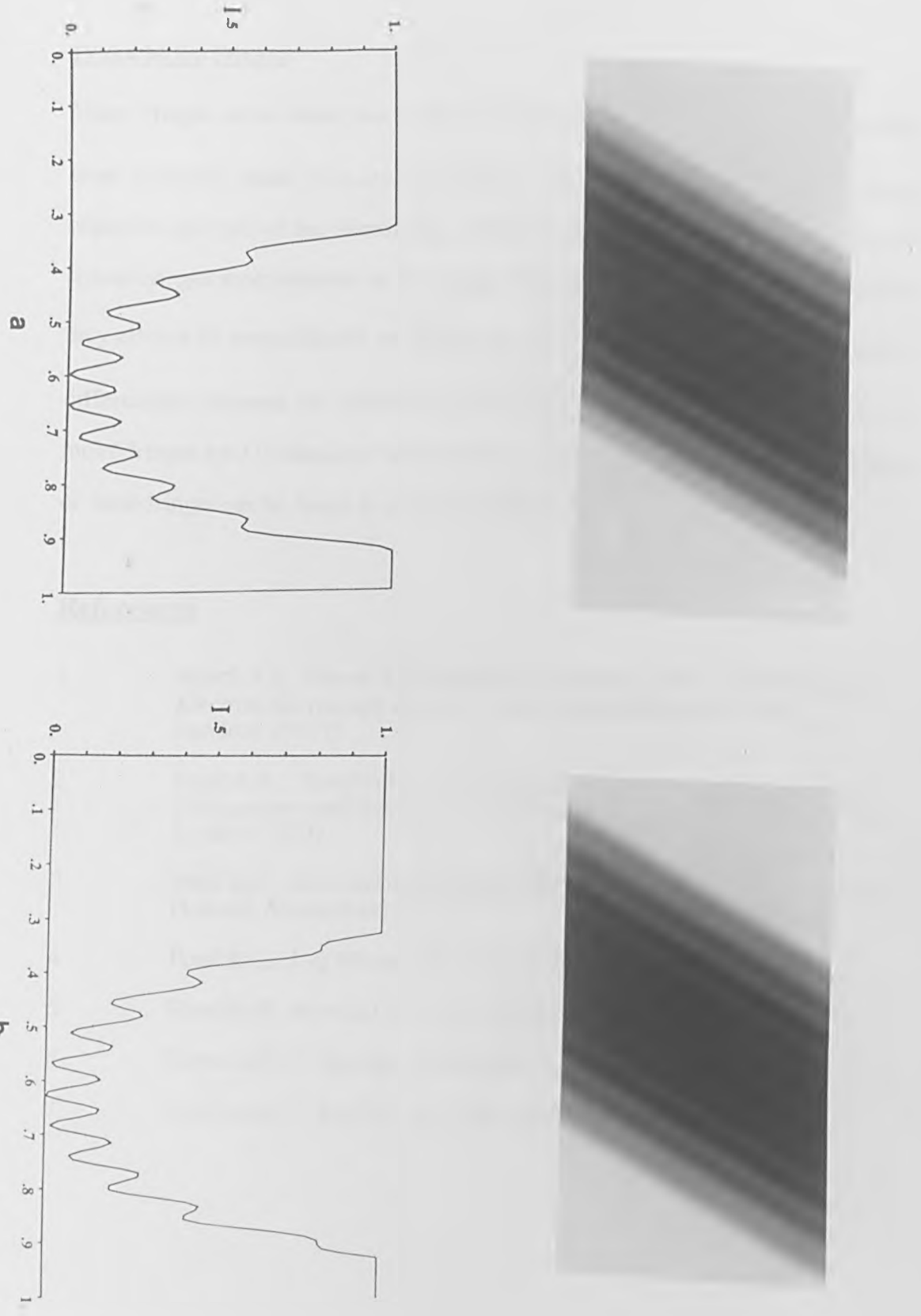

Fig 4.13: Computer-simulated images of π fringes and associated intensity profiles. (a) BF image and (b) DF image.

IV.6.4 Moire Fringes

Moiré fringes arise when two (or more) diffracted beams (g_λ and g_μ), originating from a region where two crystals overlap, are allowed to interfere within the objective aperture of the microscope. The contrast displayed consists of regularly-spaced fringes superimposed on the image. One characteristic of moiré fringes is that they always lie perpendicular to $\Delta g = g_\lambda - g_\mu$, and this feature allows the operator to differentiate between the different types of fringes and moiré fringes. Moreover, moiré fringes tend to disappear when imaging conditions change. A detailed analysis of these fringes can be found in elsewhere [1], [2], for example.

References

1 Hirsch P.B., Howie A., Nicholson R.B, Pashley DW, and Whelan M.J, *Electron Microscopy of Thin Crystals*, 2nd edn (Butterworths, London) (1977)

2 Head A.K., Humble P., Clareborough L.M., *Computed Electron Micrographs and Defect Identification*, North-Holland Publishing Co, London (1973).

3 Pond R.C., *Dislocations in Solids,* p8, (edited by F.R.N Nabarro, North-Holland, Amsterdam) (1989)

4 Pond R.C., *J. of Microscopy*, **135**, p213 (1984)

5 Humble P., Forwood C.T., *Phil. Mag.A*, **31**, p1011 (1975).

6 Forwood C.T., Humble P., *Phil Mag.A*, **31**, p 1025 (1975).

7 Amelinckx S., *Surf.Sci.*, **31**, p296 (1972)

Chapter 5

Experimental Techniques and Analytical Procedures

Overview

The first part of this chapter presents the main experimental techniques used for the preparation of both tungsten carbide and α-alumina thin films. As indicated in chapter one, the study of interfacial features in zinc oxide was carried out from specimens and observations made at the Institute of Crystallography, Russian Academy of Science.. Experimental techniques relevant to the successful preparation of zinc oxide bicrystals and determination of surface orientations can be found elsewhere [1].

The interpretation of interfacial features using the methods developed in earlier chapters necessitates prior knowledge of the boundary crystallography. It is therefore important to determine the orientation relationship between the constituent grains and also the boundary inclination and other crystallographic parameters accurately in order to perform a quantitative analysis. The necessary information may be obtained experimentally from observations made in the transmission electron microscope using the procedures outlined in this chapter. However, crystallographic calculations in the hexagonal system may be complicated unless a suitable coordinate frame is chosen. The four-dimensional framework in which all crystallographic calculations were performed facilitates vector manipulation and an outline of the method is therefore presented.

V.1 Specimen Preparation and Observation

Specimens of tungsten carbide and α-alumina were prepared in the following way. 3 mm WC discs were spark-eroded and subsequently mounted on a metal support. Each disc was ground to a thickness approximatively equal to 100 μm, and both surfaces were given a 1 μm polish. Individual specimen were then mounted on a copper grid. One face was then dimpled (see Fig 5.1) before thinning was carried out in a Gatan ion mill (model 691) at 8^0 until perforation. Further milling was subsequently carried out at shallower angles (typically between 2 or 5^0). The

preparation of thin specimens of α-alumina was found to be improved by dimpling both specimen faces, however, care should be taken during this procedure due to the brittleness of the samples.

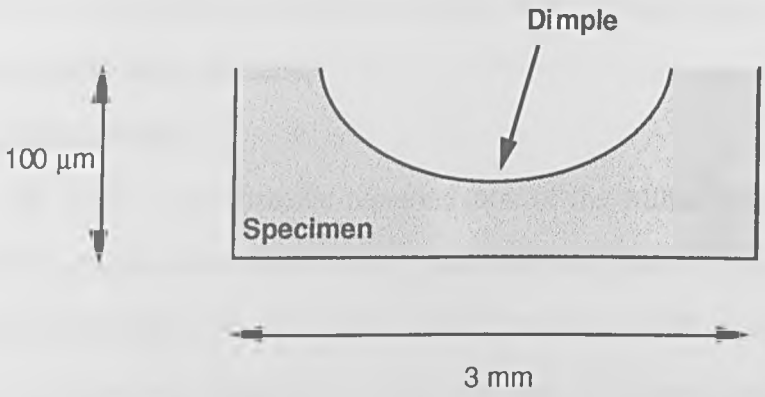

Fig 5.1: Schematic illustration of the specimen geometry befor ion-milling.

All specimens were observed in a JEOL 2000FX Transmission Electron Microscope (TEM) operating at 200 kv and grain boundaries were imaged using the diffracting conditions presented in chapter 4. Due to problems associated with charging of the specimens, α-alumina samples were carbon coated and observed using low spot sizes.

α-alumina grain boundaries were also imaged in a VG601UX field emission Scanning Transmission Electron Microscope (STEM) to determine the extent of interfacial segregation. The qualitative energy dispersive X-ray analysis data presented in chapter 6 was obtained as follows. First, a boundary was chosen as near as possible oriented parallel to the electron beam, in a reasonably thin area. The scan rotation control was used to align the boundary image parallel to the line scan (the horizontal direction on the screen). The microscope was operated at nominal magnification 1Mx, 2Mx or 5Mx, in the reduced-area mode and data was acquired by defining a box within the grain boundary area, and in the matrix for qualitative comparison.

V.2 Hexagonal Crystallography

The methods presented in this chapter involve numerous crystallographic manipulations performed in the four-dimensional frame introduced by Frank [2]. This approach presents several advantages over conventional indexing techniques and facilitates crystallographic calculations in the hexagonal system. An account of Frank's approach is given below together with a description of some of the hexagonal systems commonly encountered in the literature.

V.2.1 Miller notation

Fig 5.2(a) is a schematic representation of the Miller system. Three primitive vectors $\mathbf{a}_1$, $\mathbf{a}_2$ and $\mathbf{c}$ are used to define directions and planes (represented by [uvw] and (hkl) respectively). The main disadvantage associated with the application of this notation to hexagonal crystals lies in the fact that equivalent directions bear different indices. For instance, [211] and [111] represent equivalent directions but [111] and [111]do not. The Miller-Bravais notation makes the symmetry of the crystal apparent and is described below.

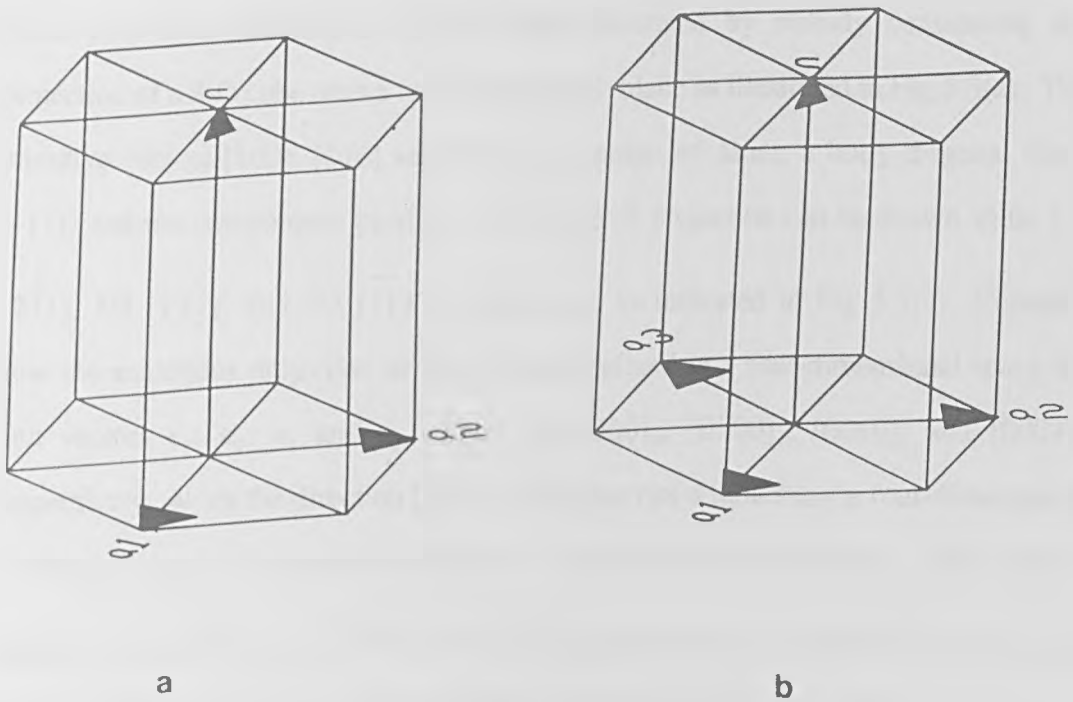

Fig 5.2: Schematic illustration of the (a) Miller notation and (b) the Miller-Bravais notation

V.1.2 Miller-Bravais notation

The Miller-Bravais notation uses four axes defined by the primitive vectors $\mathbf{a}_1$, $\mathbf{a}_2$, $\mathbf{a}_3$ and $\mathbf{c}$ (see Fig 5.2(b)) where $\mathbf{a}_1 + \mathbf{a}_2 + \mathbf{a}_3 = \mathbf{0}$. A direction is therefore represented by the four indices [uvtw] (also denoted [uv.w]) and a plane by (hkil) (or (hk.l)). Unlike in the cubic system where a plane and its normal are represented by the same set of indices, the normal to the plane (hkil) depends on the ratio c/a and is given by [hki $3/2(a/c)^2$l]. Although the Miller-Bravais scheme presents some advantages over the Miller description, commonly performed calculations are relatively complicated. The method developed by Frank [2] removes these complexities and allows such operations to be carried out readily.

V.2.3 Frank's method

Crystallographic calculations in materials belonging to the cubic system are facilitated by the use of a Cartesian set of axes. Frank [2] showed that if one imagines a conventional hexagonal cell as a three-dimensional projection of a four-dimensional cubic frame, the complexities associated with crystallographic calculations in the Miller-Bravais scheme are removed . The four-dimensional projection of a Cartesian frame in a three-dimensional space is best illustrated by initially considering the projection of a 3-D cube onto a two-dimensional plane as illustrated in Fig 5.3(a). The primitive vectors [100], [010] and [001] are projected along a body diagonal (here [111]) and the components parallel to the plane of projection can be shown to be 1/3 $[\bar{2}11]$, 1/3 $[1\bar{2}1]$, and 1/3 $[11\bar{2}]$ respectively, as indicated in Fig 5.3(a). Consider now the analogous projection of a hypercube defined in a four-dimensional space by unit vectors $\mathbf{e}_1$, $\mathbf{e}_2$, $\mathbf{e}_3$ and $\mathbf{e}_4$ equal to $[1000]_4$, $[0100]_4$, $[0010]_4$ and $[0001]_4$ respectively , along the direction $[1110]_4$ (the subscript 4 indicating a four-dimensional Cartesian frame). This projection defines a subspace cell represented by unit vectors equal to, 1/3 $[\bar{2}110]_4$, 1/3 $[1\bar{2}10]_4$, 1/3 $[11\bar{2}0]_4$, and $[0001]_4$ respectively as indicated in Fig 5.3(b). The conventional Miller-Bravais cell shown in Fig 5.2(b) can therefore be interpreted as the projection of the subcell described above providing the latter is scaled so that its dimensions correspond to the c/a ratio of the material investigated.

Frank showed that the scaling factor required, designated Λ, is equal to $c/e=(2/3)^{1/2}$ c/a. The transformation between directions indexed according to the Miller-Bravais scheme and the four-vector notation is relatively easy. A direction [uvtw] in Miller-Bravais notation for example, corresponds to the four-vector $[uvt\ \Lambda w]_4$ and the normal to the plane $(hkil)_{MB}$ is given by $[hki\ l/\Lambda]_4$.

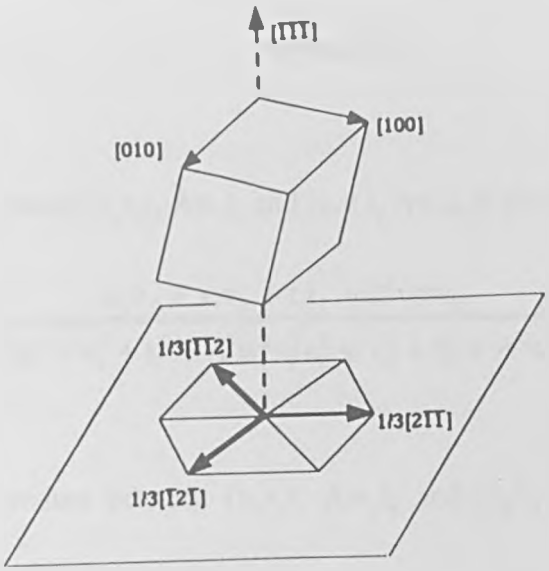

(a)

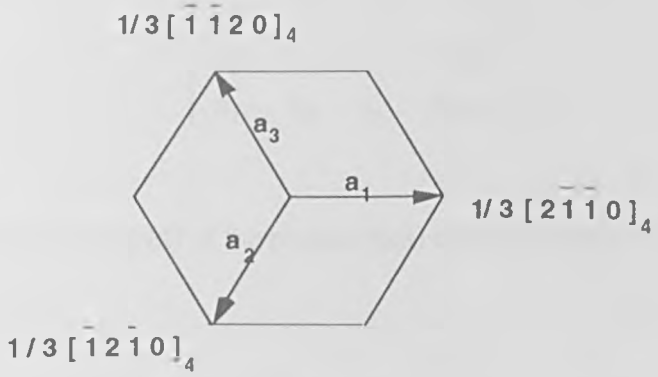

(b)

Fig 5.3: (a) Schematic representation of the projection of a cube along the <111> direction (after ref3) and (b) basal plane of the hexagonal structure in Frank's notation.

The most commonly used crystallographic entities defined in this space are described below.

(i) The magnitude of the vector $[uvt\ \Lambda w]_4$ is given by

$$\sqrt{u^2 + v^2 + t^2 + \Lambda^2 w^2} \qquad \text{in units of } \mathbf{e} \text{ (or } \sqrt{\frac{3}{2}}\ \mathbf{a}) . \tag{5.1}$$

(ii) The scalar product between $[u_1v_1t_1\ \Lambda w_1]_4$ and $[u_2v_2t_2\ \Lambda w_2]_4$ is equal to

$$u_1u_2+v_1v_2+t_1t_2+ \Lambda^2\ w_1w_2 \qquad \text{in units of } \mathbf{e}^2. \tag{5.2}$$

(iii) The angle between $[u_1v_1t_1\ \Lambda w_1]_4$ and $[u_2v_2t_2\ \Lambda w_2]_4$ is given by

$$\cos\theta = \frac{u_1u_2 + v_1v_2 + t_1t_2 + \Lambda^2 w_1w_2}{\sqrt{u_1^2 + v_1^2 + t_1^2 + \Lambda^2 w_1^2}\sqrt{u_2^2 + v_2^2 + t_2^2 + \Lambda^2 w_2^2}} \tag{5.3}$$

(iv) The vector product between $[u_1v_1t_1\ \Lambda w_1]_4$ and $[u_2v_2t_2\ \Lambda w_2]_4$ is obtained by expanding the following matrix [4]

$$\begin{bmatrix} e_1 & e_2 & e_3 & e_4 \\ \frac{1}{\sqrt{3}} & \frac{1}{\sqrt{3}} & \frac{1}{\sqrt{3}} & 0 \\ u_1 & v_1 & t_1 & \Lambda w_1 \\ u_2 & v_2 & t_2 & \Lambda w_2 \end{bmatrix} \tag{5.4}$$

(v) The interplanar spacing (d) of the planes (hkil) can be calculated from

$$d = \frac{1}{\sqrt{h^2 + k^2 + i^2 + \frac{l^2}{\Lambda^2}}} \qquad \text{in units of } \mathbf{e}. \tag{5.5}$$

V.3 Orientation Relationship

V.3.1 General procedure

The relative orientation between crystals abutting at a grain boundary is generally expressed mathematically by means of a matrix P representing a right-handed rotation θ about an axis r common to both crystals. The pair r/θ, referred to as the axis/angle pair, may be obtained experimentally by determining at least two sets of parallel directions in each crystal. Beam directions represent a convenient choice for such directions as they can be calculated with good accuracy using the method described in V.3.2. The orientation relationship is therefore determined by indexing parallel beam directions with respect to both crystals for several goniometer settings. The axis/angle pair may be derived using the methods outlined in V.3.3 and the rotation matrix calculated as described in section V.3.4.

V.3.2 Accurate determination of beam directions (**B**)

Several methods may be used for the determination of beam directions (see Von Heinmendahl et al [5], or Pumphrey and Bowkett [6] for example). A typical procedure consists of orientating the specimen so that three pairs of Kikuchi lines intersect to form a triangle as depicted in Fig 5.4. The direction of the electron beam with the pattern is denoted O and the trace of a plane is represented by a dotted line midway through the associated pair of Kikuchi lines. In addition, the diffraction vector $\mathbf{g}_j$, perpendicular to the plane $(h_jk_ji_jl_j)_{MB}$, is expressed as a reciprocal four-vector by $h_jk_ji_jl_j/\Lambda$ (with i= 1,2,3..n). Kikuchi lines can be indexed specifically by measuring the spacings p_1, p_2, p_3 (proportional to the Bragg angle) and the angles between the diffraction vectors involved. Once the Kikuchi lines have been indexed, the poles A, B

and C may be obtained by taking the respective cross products, for example, $A = [h_2k_2i_2l_2/\Lambda]_4 \times [h_1k_1i_1l_1/\Lambda]_4$ (A pointing into the page).

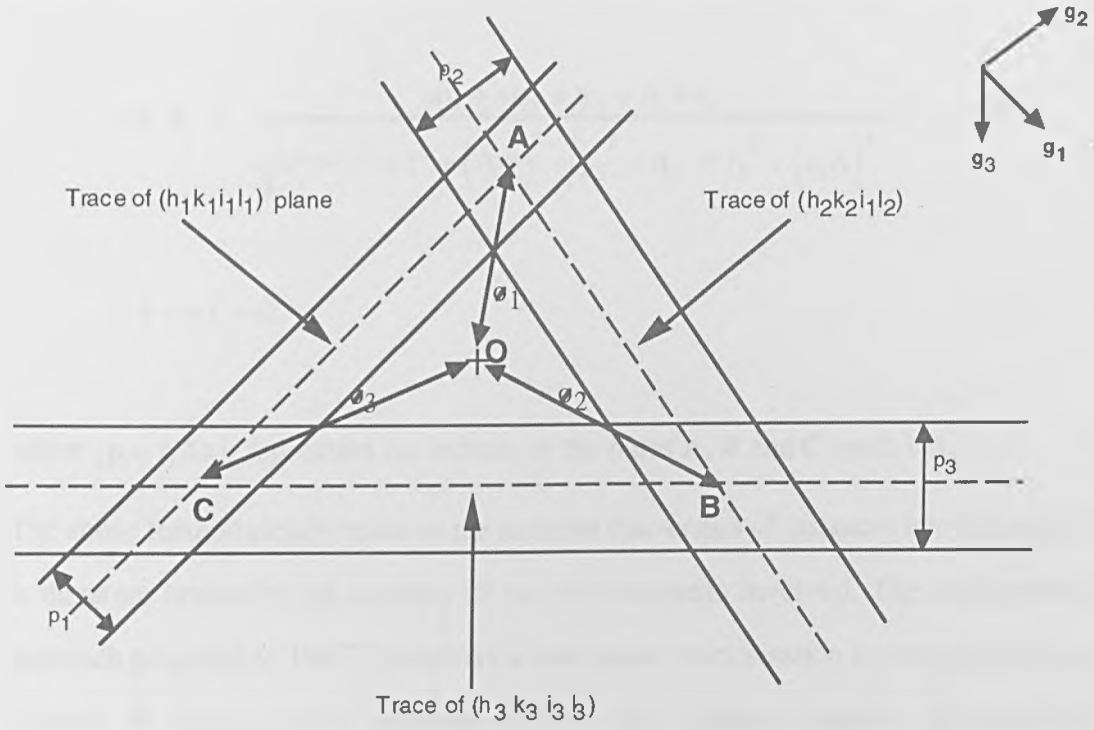

Fig 5.4: Schematic illustration of the indexing of a Kikuchi pattern.

The calculation of the beam direction from such a pattern is based on the angular position of the Kikuchi lines with respect to O. The pattern can therefore be calibrated so that the distances OA, OB and OC are converted into angles ϕ_1, ϕ_2 and ϕ_3 respectively by calculating the angles separating the poles A, B and C using (5.3) and measuring the corresponding distances AB, BC and AC. If the beam direction is represented by $[uvt\Lambda\omega]_4$, the latter may then be calculated by solving the following system of equations

$$\cos\phi_1 = \frac{up_1 + vq_1 + tr_1 + \Lambda^2 ws_1}{\sqrt{u^2 + v^2 + t^2 + (\Lambda w)^2}\sqrt{p_1^2 + q_1^2 + r_1^2 + (s_1\Lambda)^2}}, \qquad (5.6)$$

$$\cos\phi_2 = \frac{up_2 + vq_2 + tr_2 + \Lambda^2 ws_2}{\sqrt{u^2 + v^2 + t^2 + (\Lambda w)^2}\sqrt{p_2^2 + q_2^2 + r_2^2 + (s_2\Lambda)^2}}, \quad (5.7)$$

$$\cos\phi_3 = \frac{up_3 + vq_3 + tr_3 + \Lambda^2 ws_3}{\sqrt{u^2 + v^2 + t^2 + (\Lambda w)^2}\sqrt{p_3^2 + q_3^2 + r_3^2 + (s_3\Lambda)^2}}, \quad (5.8)$$

$$u + v + t = 0, \quad (5.9)$$

where $[p_i q_i r_i \Lambda s_i]_4$ represents the indices of the poles A, B and C (with i=1,2,3).

The above method clearly relies on the accurate conversion of distances into angles and is therefore limited by the accuracy of the measurements involved. The mathematical approach proposed by Ball [7] employs a least square minimisation to compute the best value of **B** from a set of experimental data. The method optimises the problems described above and was therefore used throughout this work. Although Ball's algorithm was developed for cubic crystals, MacLaren [8] showed it is valid in the hexagonal system provided the 4-D cubic reference frame proposed by Frank was used throughout. An outline of the principles of the modified method is now presented.

Ball's derivation assumes that the centre of the Kikuchi pattern (point designated O in Fig 5.4) has been located and that Kikuchi lines have been identified and indexed.

For a Kikuchi line j, a unit vector $\mathbf{g}_j$, can be found so that

$$\mathbf{g}_j \cdot \mathbf{B} = \sin\theta_j , \quad (5.10)$$

where θ_j is the Bragg angle and **B** the beam direction corresponding to this condition.

Taking experimental errors into account, a parameter f_j is defined so that

$$f_j = \mathbf{g}_j \cdot \mathbf{B} - \sin\theta_j , \quad (5.11)$$

or

$$f = \mathbf{g} \cdot \mathbf{B} - \sin\theta \text{ for simplicity.} \quad (5.12)$$

Let the diffraction vectors **g** and **B** be defined by the general indices hkil/Λ and $[uvt\Lambda w]_4$ respectively. Substituting for the indices of **g** and **B** in equation 5.12 gives

$$f = hu + kv + it + lw - \sin\theta, \qquad (5.13)$$

and since **B** is a unit vector we also have

$$w = \frac{\sqrt{\left(1-\left(u^2+v^2+t^2\right)\right)}}{\Lambda}, \qquad (5.14)$$

which yields

$$f = hu + kv - i\left(u+v\right) + \frac{1}{\Lambda}\sqrt{\left(1-2\left(u^2+v^2+t^2\right)\right)} - \sin\theta, \qquad (5.15)$$

with u+v =-t.

Ball defined two parameters F_u and F_v minimising the sum of the squares of f as follows

$$F_u = \frac{\partial_f}{\partial_u} = \frac{1\left(2u+v\right)}{\lambda\left(1-2\left(u^2+uv+v^2\right)\right)^{1/2}}, \qquad (5.16)$$

and

$$F_v = \frac{\partial_f}{\partial_v} = k - i - \frac{1\left(2v+u\right)}{\lambda\left(1-2\left(u^2+uv+v^2\right)\right)^{1/2}}, \qquad (5.17)$$

where $\frac{\partial_f}{\partial_u}(\frac{\partial_f}{\partial_v})$ is the derivative of F_u (F_v), and showed that if $|u_o, v_o, t_o, \Lambda w_o]_4$ is a good approximation for **B**, then a better solution is given by $|(u_o-U), (v_o-V), -(u+v), (1-(u^2+v^2+t^2)^{1/2}]$, where $u = u_o-U, v = v_o-V$ and $t = -(u+v)$ and both U and V are solutions of the following simultaneous equations

$$\sum \left(F_u\right)^2 U + \sum \left(F_u F_v\right) V = \sum F_u f, \qquad (5.18)$$

and

$$\sum \left(F_u F_v\right) U + \sum \left(F_v\right)^2 V = \sum F_v f. \qquad (5.19)$$

The summations designated by Σ are made over all the pairs of Kikuchi lines identified on the micrograph and a minimum of seven should be selected to achieve reasonable accuracy. As a first approximation for **B**, the indices of poles such as A,B and C in Fig 5.4 are used; i.e $[p_i\ q_i\ r_i\ \Lambda s_i]_4 = [u_o,\ v_o, t_o, \Lambda w_o]_4$. In practice, the solutions for **B** converge rapidly (typically after five iterations) unless the first approximation is very poor . All the calculations can be performed on a personal computer in a very short time. A Kikuchi pattern, showing the Kikuchi lines selected for a typical calculation is presented in Fig 5.5.

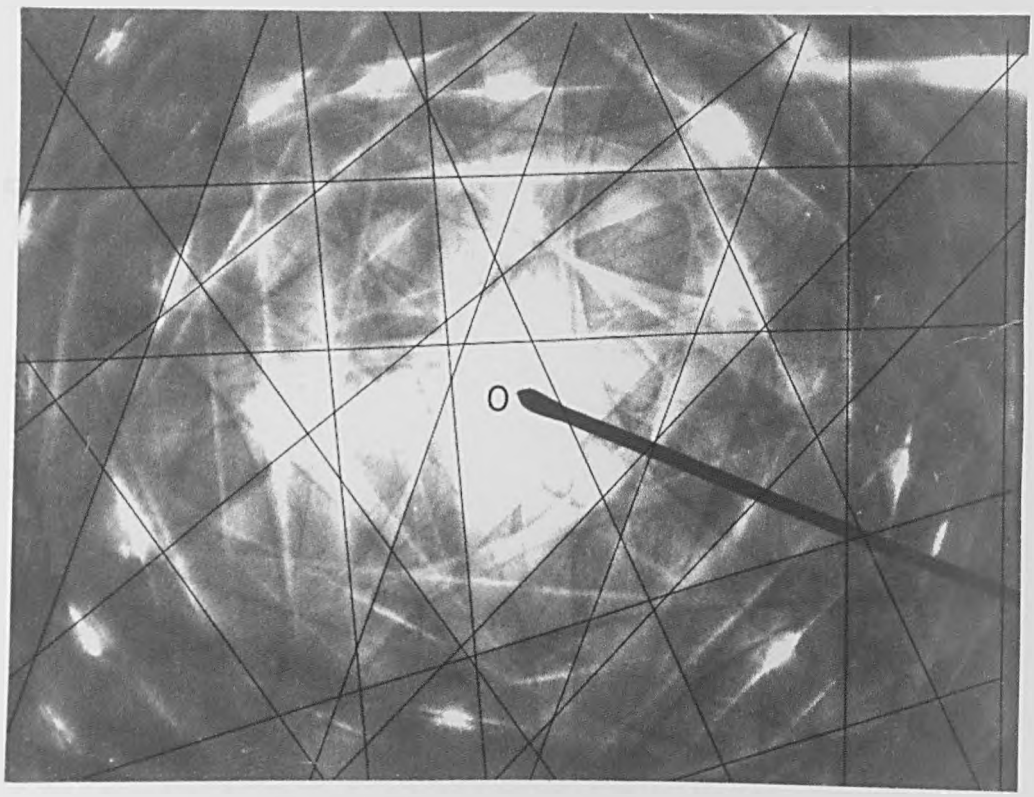

Fig 5.5: Micrograph showing a typical Kikuchi pattern

V.3.3 Determination of the Angle/axis pair (R/θ)

As stated earlier, the angle/axis pair can be determined from the knowledge of at least two sets of parallel directions in each crystal. Several methods are available for such a calculation and the technique due to Forwood and Clareborough [9], presented below, involving simple crystallographic calculations is used throughout this work . Let **p** and **q** be a pair of parallel beam directions specified by the unit vectors $\mathbf{x}_p$, $\mathbf{y}_p$ and $\mathbf{x}_q$, $\mathbf{y}_q$ respectively as shown in Fig 5.6.

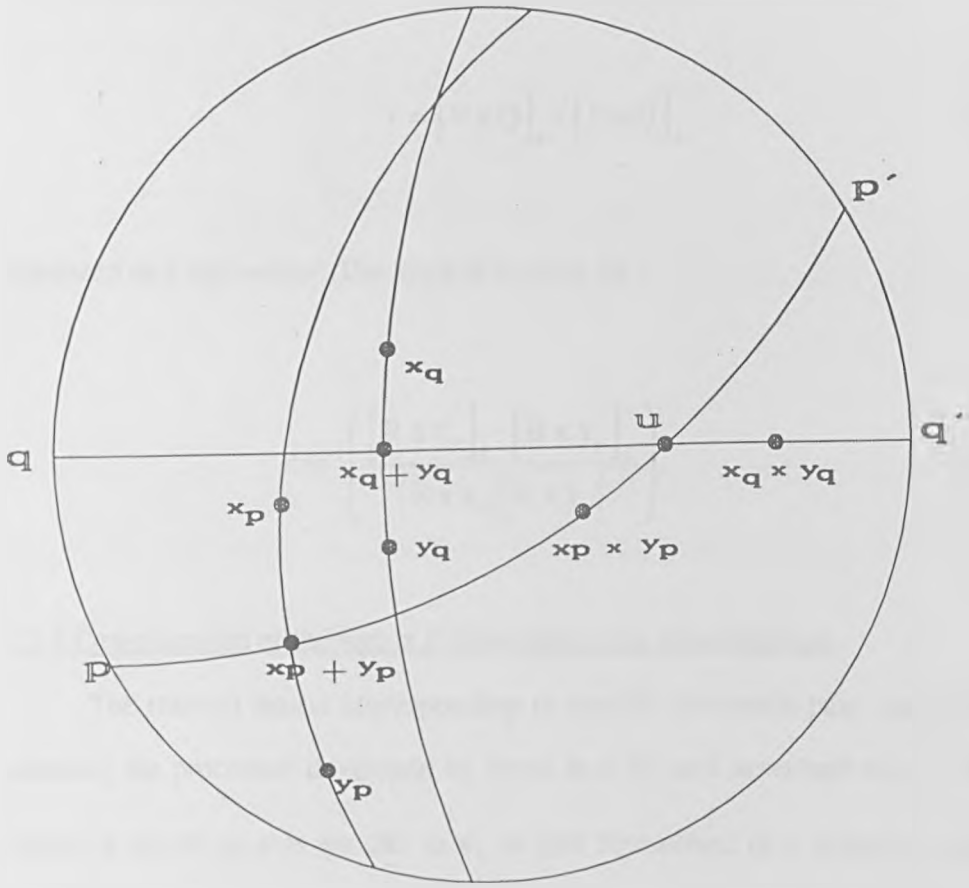

Fig 5.6: Schematic representation of the determination of the axis/angle pair r/θ.(after ref 9)

It can be shown that for the beam direction **p** the rotation axis, R , lies on the zone PP' given by

$$P = \left[x_p + y_p\right]_4 \mathbf{x} \left[x_p \mathbf{x}\ y_p\right]_4 . \qquad (5.20)$$

Similarly with the beam direction **q**, r lies on the zone QQ' defined by

$$Q = \left[x_q + y_q\right]_4 \mathbf{x} \left[x_q \mathbf{x}\ y_q\right]_4 . \qquad (5.21)$$

The intersection of the zones PP and QQ represents the rotation axis R; i.e,

$$r = \left[P \mathbf{x} Q\right]_4 / \left[P \mathbf{x} Q\right]_4 , \qquad (5.22)$$

expressed as a unit vector. The angle θ is given by

$$\cos^{-1}\left(\frac{\left[R \mathbf{x} x_p\right]_4 \cdot \left[R \mathbf{x} y_p\right]_4}{\left|R \mathbf{x} x_p\right| \left|R \mathbf{x} y_p\right|} \right). \qquad (5.23)$$

V.3.4 Determination of the matrix P representing the misorientation

The rotation matrix corresponding to specific axis/angle pairs can be obtained following the procedure developed by Pond et al [4] and described below. A general rotation θ about an axis parallel to $\mathbf{e}_3$ is first formulated in a 4-space frame. This situation is illustrated schematically in Fig 5.7 where the axes before rotation are labelled $\mathbf{e}_1$, $\mathbf{e}_2$, $\mathbf{e}_3$ and $\mathbf{e}_1$,$\mathbf{e}_2$,$\mathbf{e}_3$ after rotation. It can be shown that the matrix represented such an operation is given by

$$R = \begin{bmatrix} \cos\theta & -\sin\theta & 0 & 0 \\ \sin\theta & \cos\theta & 0 & 0 \\ 0 & 0 & 1 & 0 \\ 0 & 0 & 0 & \pm 1 \end{bmatrix} \qquad (5.24)$$

The column vectors of **R** are four-vectors representing the rotated axes expressed in the initial coordinate frame.

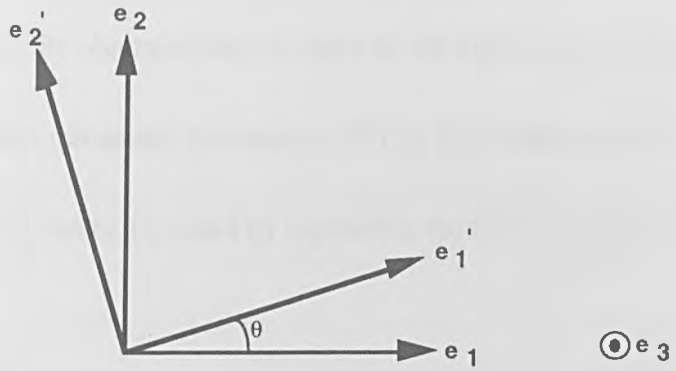

Fig 5.7: Schematic illustration of the derivation of the matrix R.

R may now be re-expressed as a rotation about a specific axis designated by its indices $[u_3,v_3,t_3,\Lambda w_3]_4$ in the coordinate frame of the reference crystal using the transformation $\mathbf{P} = \mathbf{TRT}^{-1}$, where the matrix T has the form

$$T = \begin{bmatrix} u_1 & u_2 & u_3 & \frac{1}{\sqrt{3}} \\ v_1 & v_2 & v_3 & \frac{1}{\sqrt{3}} \\ t_1 & t_2 & t_3 & \frac{1}{\sqrt{3}} \\ \Lambda w_1 & \Lambda w_2 & \Lambda w_3 & 0 \end{bmatrix} \qquad (5.25)$$

The matrix **T** is composed of four unit 4-vectors parallel to the unrotated axes of the initial frame but expressed in the reference crystal. The first column corresponds to an arbitrary direction perpendicular to $\mathbf{e}_3$ while the second column is obtained by taking the cross-product of $[u_3,v_3,t_3,\Lambda w_3]_4$ with $[u_1,v_1,t_1,\Lambda w_1]_4$. The fourth column corresponds to the unit vector parallel to the projection direction.

It is also convenient to be able to perform the reverse calculations, i.e. determining the axis/angle pair $[u_3,v_3,t_3,\Lambda w_3]_4 / \theta$, from a given rotation matrix P. The misorientation angle θ can be readily obtained from the trace of the matrix; it is equal to $(2+2\cos\theta)$ if P leaves the fourth dimension invariant or $(2\cos\theta)$ in other cases [4]. The rotation axis $[u_3,v_3,t_3,\Lambda w_3]_4$ can be obtained by expanding the following determinant

$$\begin{vmatrix} e_1 & e_2 & e_3 & e_4 \\ 1 & 1 & 1 & 0 \\ p(1,1)-1 & p(1,2) & p(1,3) & p(1,4) \\ p(2,1) & p(2,2)-1 & p(2,3) & p(2,4) \end{vmatrix}, \quad (5.26)$$

where p(i,j) represents the element in the i^{th} column and j^{th} row of P Pond et al [4]. Due to the symmetry exhibited by the constituent crystals, equivalent descriptions of the axis/angle pair and the rotation matrix P exist. These can be determined by combining the rotation matrix P with each of the proper symmetry operators contained in the spacegroup of the reference crystal in turn. In other words, if λ is taken as the reference frame, equivalent descriptions of P will be given by

$$\mathbf{P}W(\lambda)_i \quad (5.27)$$

where $W(\lambda)_i$ corresponds to the ith symmetry operation in white crystal's spacegroup. Equivalent descriptions of the axis/angle pair can then be determined from the set of equivalent matrices generated by (5.22) using the method described earlier. It is often

useful to describe experimental descriptions as the deviation from a reference structure. If $\mathbf{P}_{exp}$ and $\mathbf{P}_{ref}$ are the matrices corresponding to the experimental and reference orientations respectively, the deviation from the reference structure ($\mathbf{P}_{dev}$) is expressed as:

$$\mathbf{P}_{dev} = \mathbf{P}_{exp}\,\mathbf{P}_{ref}^{-1} \qquad (5.28)$$

V.4 Determination Of The Line Direction Of Interfacial Defects.

The method described here uses trace analysis to determine the true line direction **u** of discontinuities arising at interfaces . Images of the defects are taken in at least three different diffracting conditions $\mathbf{g}_i$ (and three beam directions $\mathbf{B}_i$) so as to obtain three corresponding projections of **u** denoted by $\mathbf{u}_i$ (where i =1,2,3). For each image, the angle θ_i that the projected line direction $\mathbf{u}_i$ makes with the diffracting vector $\mathbf{g}_i$ (in the direction $\mathbf{g}_i$') is measured (see Fig 5.8). The true crystallographic direction of the defect can then be determined using trace analysis as described below.

First, the great circles associated with each beam direction $\mathbf{B}_i$ are plotted on the stereogram and the corresponding diffraction vectors $\mathbf{g}_i$ are marked accordingly (see Fig. 5.9). Next, each projected line direction $\mathbf{u}_i$ is plotted at the corresponding angle from $\mathbf{g}_i$ and in the correct sense. The true line direction **u** lying in the plane containing both the beam direction and the projected line direction $\mathbf{u}_i$ for each of the operative reflections, the region where these planes intersect (U in Fig 5.9) represents the true line direction of the defect.

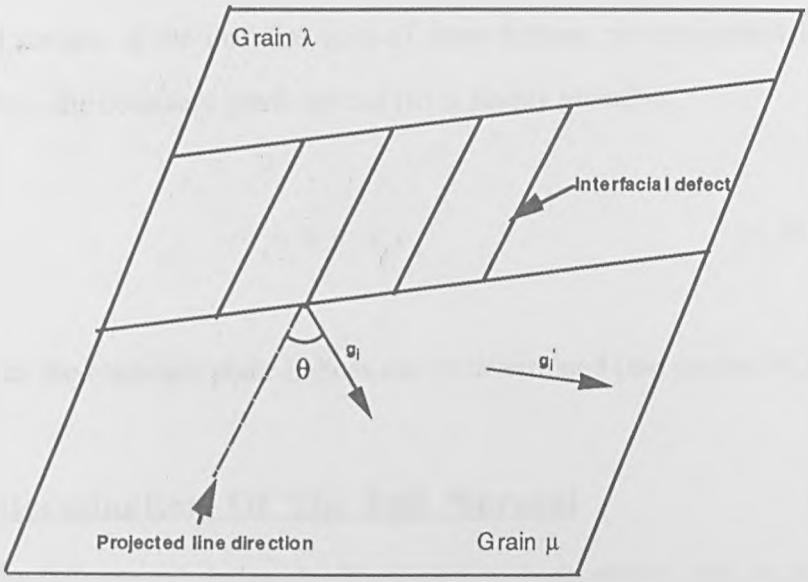

Fig 5.8: Schematic illustration of the measurement involved in the determination of the line direction.

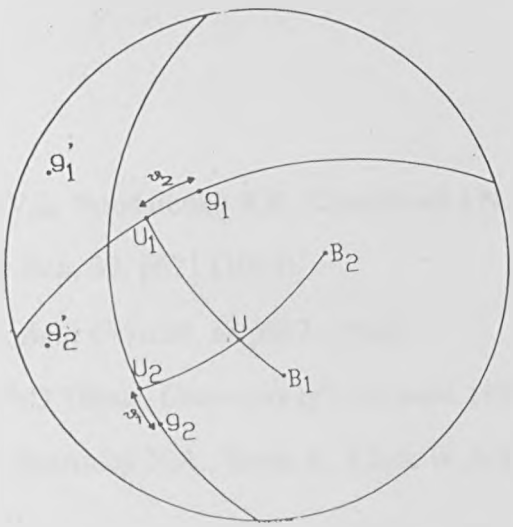

Fig 5.9: Schematic illustration of the determination of the true line direction

V.5 Determination Of The Boundary Plane

The boundary plane can be determined using the method presented in V.4 provided two features lying in the interface can be identified. These can be dislocations or any other linear feature such as the intersection of the boundary plane with the

specimen surface. If the line directions of these features are designated by u_1 and u_2 respectively, the boundary plane normal (**n**) is simply given by

$$\mathbf{n} = u_1 \times u_2 \qquad (5.29)$$

from which the boundary plane indices can be determined (see section V.2.3)

V.6 Determination Of The Foil Normal

The foil normal, indexed with respect to both grains, can be determined by stereographic techniques from the traces of features lying in the surface of the foil. However, a simpler method consists in determining the beam direction at zero degree tilt of the goniometer.

References

1 Solov'eva V.I., Bondarenko K.P., Bystrikova I.N., and Kheiser D.M., Crystallogr.Rep, **39**, p671 (1994)

2 Frank F.C., *Acta Crystall.* **18** p862 (1965)

3 Casey S., PhD Thesis, *University of Liverpool* (1994)

4 Pond R.C., McAuley N.A., Serra A., Clark W.A.T., *Scripta Metall.*, **21**, p971 (1987).

5 Von Heinmendahl M., Bell W., Thomas G., *J.Appl.Phys.* **35** p3614 (1964).

6 Pumphrey, P.H., Bowkett K.M., *Phys.Stat.Sol* (a) **2**, p239 (1970).

7 Ball C.J., *Phil. Mag.A.*, **44**, p1307 (1981).

8 MacLaren I., PhD Thesis, *University of Birmingham* (1995)

9 Forwood C.T., Clarebrough L.M., *Electron Microscopy of Interfaces in Metals and Alloys*, (Bristol:Adam Hilger/IOP publishing) (1991)

Chapter 6

Theoretical and Experimental Results

Overview

As discussed in III-4, the topological theory may be used to characterise interfacial features *a-posteriori* , and this approach is therefore particularly useful for the interpretation of observations made by high-resolution microscopy (HREM). Circuit mapping was used in the present work to study the structure of ZnO grain boundaries exhibiting predetermined misorientations. The first section of this chapter presents the crystallography and observations associated with two boundaries which may be described as belonging to the "special" category introduced in chapter 1 . The characterisation of these interfaces was carried out from supplied micrographs (see chapter 5) and the details concerning both the fabrication of ZnO bicrystals and the HREM image parameters used can be found elsewhere [1]. In the second section, experimental observations of three special high-angle grain boundaries are presented, and a detailed analysis of these observations can be found in chapter 7. Selected images, obtained under various diffracting conditions, are shown, and the crystallographic parameters describing each interface are given. Finally, a third section discusses the observation and analysis of grain boundaries in α-alumina (sapphire).

VI.1 Structure Of Grain Boundaries In ZnO

VI.1.1 Crystallographic considerations

A solid-phase method [2] was used to produce two bicrystals with specific target misorientations θ_t corresponding to rotations equal to 19 and 30^0 about the common [0001] direction. The [0001] axes were found to be aligned within experimental accuracy whereas measured rotation angles, θ_{exp}, deviated slightly from θ_t, as indicated in Table 6.1. As explained earlier, dichromatic patterns are useful as reference spaces for characterisation of the defect content of interfaces, and the most appropriate ones, with rotation angles θ_{ref} close to that observed experimentally, were

identified for each bicrystal. Table 6.1 shows the corresponding angular deviations $\Delta\theta$ from these reference orientations.

Table 6.1. Crystallographic parameters

λ *surface*	μ *surface*	θ_i	θ_{exp}	θ_{ref}	$\Delta\theta$
$(\bar{1}320)$	$(01\bar{1}0)$	19°	17.8 ± 0.1°	17.89°	0.09°
$(0\bar{1}10)$	$(11\bar{2}0)$	30°	31.5 ± 0.1°	32.2°	-0.7°

The orientation [0001]/ 17.8 $\pm 0.1^0$ corresponds within experimental accuracy, to that of the periodic dichromatic pattern with rotation angle $\theta_{ref} = 17.89^0$ shown in Fig 6.1(a). In CSL terminology, the orientation [0001]/17.89^0 is referred to as Σ=13. First, the white lattice (λ) was constructed in an orientation corresponding to that observed experimentally, i.e. with hexagons connecting ZnO atomic columns (dark honeycomb structure in Fig 6.2). The λ pattern was then copied and rotated by exactly 17.89^0 about [0001] to create the μ lattice. The superimposition of the two lattices corresponds to the configuration shown in Fig 6.1a. Similarly, the orientation [0001]/31.5$\pm$0.1^0 is very close to that of the periodic dichromatic pattern with $\theta_{ref} = 32.2^0$ (Σ=31) depicted in Fig 6.1 (b).

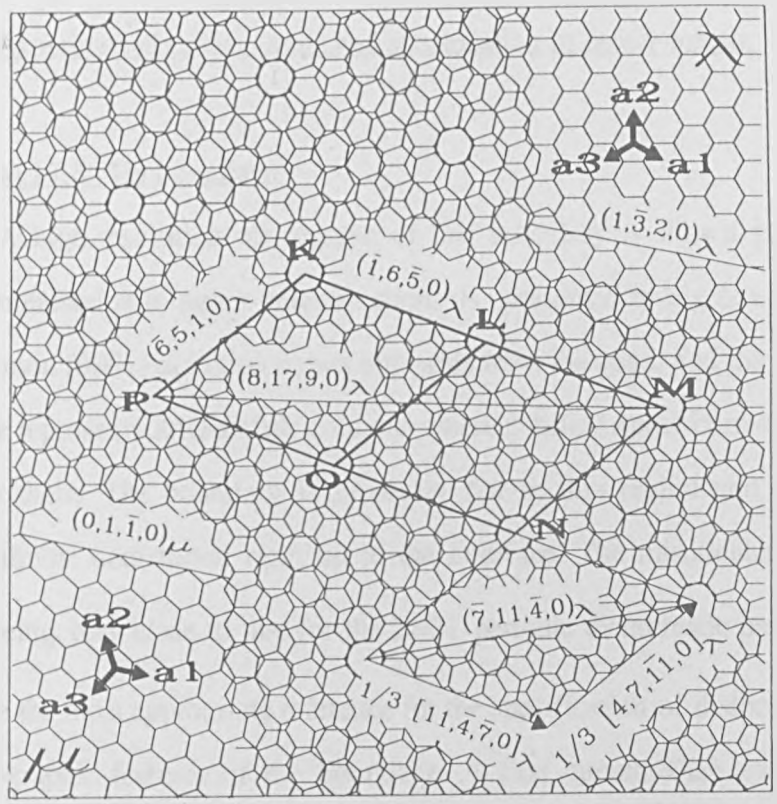

(*a*)

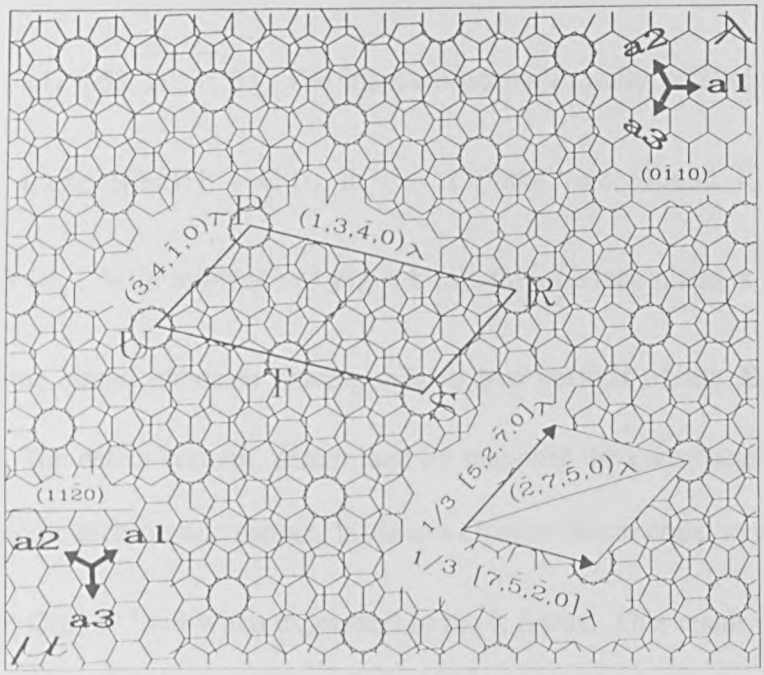

(*b*)

Fig 6.1: Dichromatic patterns formed by rotation of hexagonal lattices by (a) [0001] /17.89^0 (Σ=31) and (b) [0001]/ 32.2^0 (Σ=13)

VI.1.2 Experimental observations and specification of defect content

a) 17.8^0 Tilt boundary

A high-resolution micrograph of this boundary is shown in Fig 6.2 and an image, obtained at a higher-magnification, is presented in Fig 6.3. In both images, the common [0001] direction points outwards from the page, and the dark honeycomb structure represents ZnO atomic columns whereas bright spots correspond to channels between them. The boundary is relatively flat in this region and adjacent crystals appear almost undistorted right up to the interface. The misorientation between the grains being very close to that for the Σ=31 periodic dichromatic pattern, the latter is therefore the most appropriate reference for the specification of dislocation content and crystallographic features of the boundary. A first circuit SXF was constructed as shown in Fig 6.2, with segments $\mathbf{C}(\lambda)=\mathbf{SX}=1/3[\bar{5}2\ 2\ 50\ 0]_\lambda$ and $\mathbf{C}(\mu)=\mathbf{XF}=1/3[58\ \bar{2}0\ \bar{3}8\ 0]_\mu$. The interface normal, locally parallel to $\mathbf{C}(\lambda)$ x [0001] in the λ frame ([0001] x $\mathbf{C}(\mu)$ in the μ frame) was found to be $[\bar{8}\ 17\ \bar{9}\ 0]_\lambda$ /$[3\ 16\ \bar{1}3\ 0]_\mu$. With reference to Fig 6.1 (a), the interface plane is locally parallel to PM and the circuit indicated corresponds to two periods of the Σ=31 $(\bar{8}\ 17\ \bar{9}\ 0)_\lambda$ interface. The defect content, determined by mapping the constructed circuit into the Σ=31 periodic dichromatic pattern, leads to a closure failure equal to zero, i.e. $\mathbf{C}(\lambda,\mu) = \mathbf{C}(\lambda)+\mathbf{P}\,\mathbf{C}(\mu)\,\mathbf{P}^{-1} = \mathbf{0}$ when expressed in the λ frame. This result is consistent with the region of interface encompassed by the circuit being locally defect-free and periodic. The same procedure was followed for the characterisation of another region of this interface, shown in Fig 6.3.

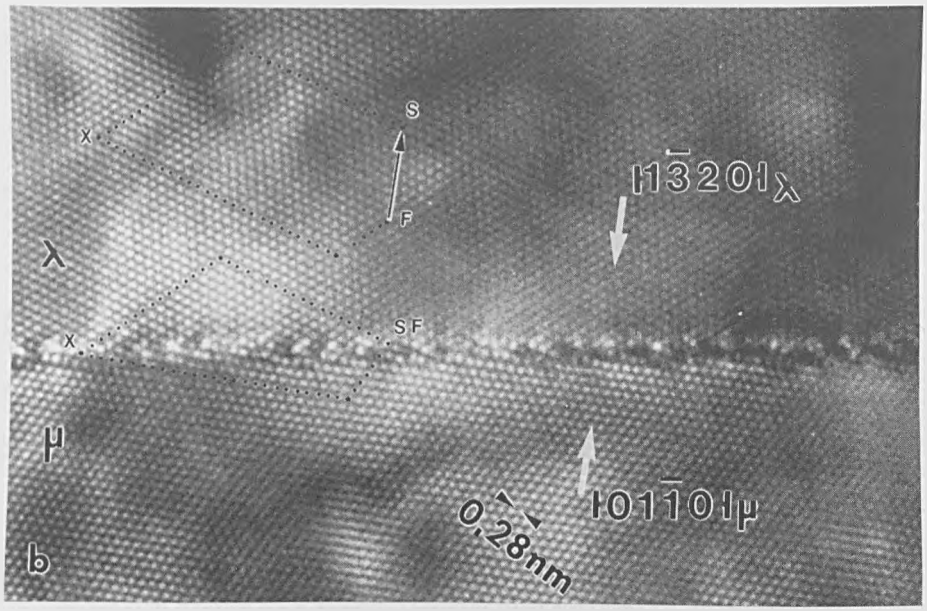

Fig 6.2: High-resolution micrograph of 17.8° tilt boundary. After ref [1]

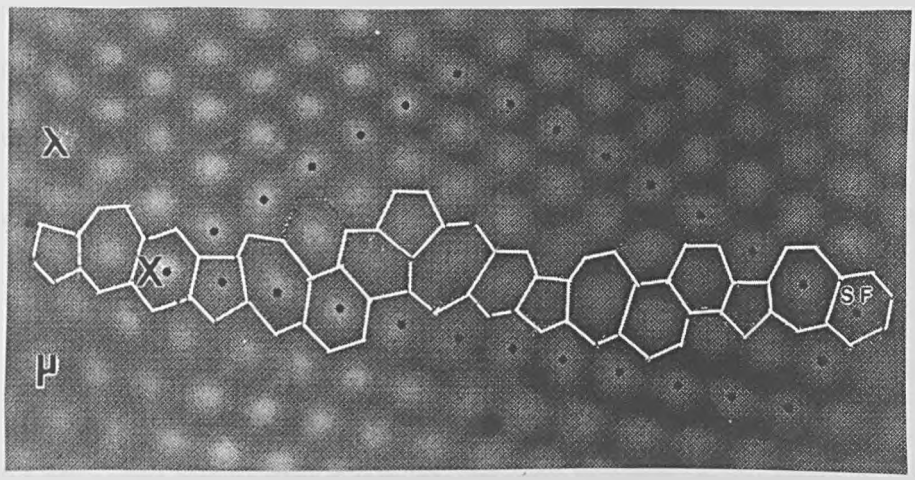

Fig 6.3: Another region of the 17.8° tilt boundary. After ref[1]

It is clear from Fig 6.3 that the boundary structure comprises a sequence of channels coordinated by fivefold, sixfold, and sevenfold arrangements of atomic columns and this will be discussed in more detail in chapter 7.

A circuit, labeled SXF, was constructed as illustrated, with $\mathbf{C}(\lambda)=\mathbf{SX}=1/3[\bar{2}2\ 2\ \bar{2}0\ 0]_{\lambda}$ and $\mathbf{C}(\mu)=\mathbf{XF}=[\ 8\ \bar{3}\ \bar{5}\ 0]_{\mu}$. When this circuit is mapped into Fig 6.1 (a), the closure failure is expressed as $\mathbf{C}(\lambda,\mu) = \mathbf{C}(\lambda)+\mathbf{P}\ \mathbf{C}(\mu)\ \mathbf{P}^{-1}$

= 1/93[$\bar{7}$ 11 $\bar{4}$ 0], and the total dislocation content has therefore a Burgers content equal to 1/93[7 $\bar{11}$ 4 0] which corresponds to an interfacial edge dislocation with minimum magnitude. Again, this will be discussed further in chapter 7.

b) 31.5^0 tilt boundary

A low-magnification image of the studied 31.5^0 tilt boundary is shown in Fig 6.4. In contrast to the 17.8^0 tilt boundary, this interface is not planar and exhibits several facets, labeled facets A to E in Fig 6.4, in the [0001] zone. The pairs of facets A and C, and B and D, have similar orientations and are described in more detail. As discussed earlier, the observed misorientation between the adjacent grains corresponds to that for the periodic Σ=13 dichromatic pattern illustrated in Fig 6.1 (b) . The latter is therefore a suitable reference space for the specification of defect content and crystallographic features associated with this boundary. Circuits encircling the observed facets were constructed and the orientation of facets D and C were found to be close to the $(\bar{2}\ 7\ \bar{5}\ 0)_\lambda$ and $(1\ 3\ \bar{4}\ 0)_\lambda$ boundaries labeled TR and PR respectively in Fig 6.1 (b).

Fig 6.4: Low- magnification image of 31.5^0 tilt boundary exhibiting faceted structure. After ref[1]

Filtered images of these facets, obtained at a higher magnification, are presented in Fig 6.5 (a) and Fig 6.5 (b) respectively (note that the tunnels between atomic columns appear in dark contrast in Fig 6.5 (b)). It is clear from these images that the structure of both these facets can be described in terms of arrangements of fivefold, sixfold- and sevenfold-coordinated channels, similarly to the 17.8^0 boundary.

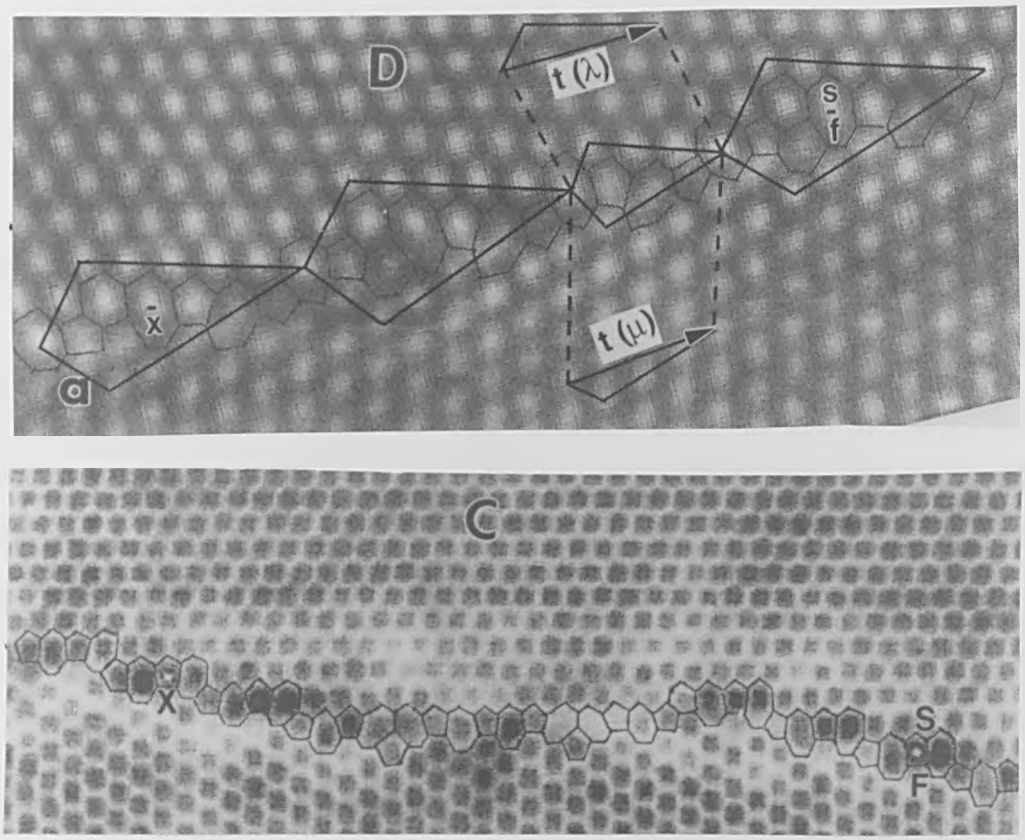

Fig 6.5: Filtered images of (a) facet D and (b) facet C of the 31.5^0 boundary. After ref[1]

The defect content of both facet D and C was characterised by circuit mapping as explained in section III.4. A circuit was constructed around facet D, as illustrated in Fig 6.5 (a), with segments $\mathbf{C}(\lambda)=\mathbf{SX}=[\bar{3}1\ 8\ \bar{2}3\ 0]_\lambda$ and $\mathbf{C}(\mu)=\mathbf{XF}=1/3[31\ \bar{2}3\ 8\ 0]_\mu$, and subsequently mapped into Fig 6.1(b) to give a closure failure $\mathbf{C}(\lambda,\mu)=1/39[\bar{2}\ 7\ \bar{5}\ 0]_\lambda$. Thus, the circuit encompasses an interfacial dislocation with $\mathbf{b}= 1/39[2\ \bar{7}\ 5\ 0]_\lambda$. The topological significance of this result is explained in detail in chapter 7. A second circuit was constructed in a similar way

around facet C (see Fig 6.5 (b)) with segments $\mathbf{C}(\lambda)=\mathbf{SX}=[\bar{1}9\ 11\ 8\ 0]_{\lambda}$ and $\mathbf{C}(\mu)=\mathbf{XF}=1/3[46\ \bar{5}3\ 7\ 0]_{\mu}$. When mapped into the dichromatic pattern shown in Fig 6.1 (b), this circuit gives a closure failure $\mathbf{C}(\lambda,\mu)=1/39[5\ 2\ \bar{7}\ 0]_{\lambda}$. Again, the dislocation content of this facet has a total Burgers vector equal to $\mathbf{b}= 1/39[\bar{5}\ \bar{2}\ 7\ 0]_{\lambda}$, and this is discussed further in chapter 7.

VI.2 Structure Of Grain Boundaries In Tungsten Carbide

The vast majority of high-angle grain boundaries observed in this work were planar with no resolvable features in them. However, some planar and non-planar interfaces, both containing dislocation networks, were imaged and these are presented below. A brief description of the symmetry and grade of material used can be found in appendix 1.

VI.2.1 Example of a non-planar grain boundary (grain boundary 1)

(a) Observations

Fig 6.6 (a-d) are micrographs of this non-planar boundary, taken under three different diffracting conditions using a JEOL 2000 FX microscope operating at 200kv. Two sets of closely-spaced dislocations (denoted set *a* and *b*) are clearly visible on some of these images, however, it is interesting to note that the contrast displayed by both sets in Fig 6.6(d) is very weak. A schematic illustration of the boundary, showing the non-planar nature of this interface together with a schematic arrangement of the dislocation network, is represented in Fig 6.7. The orientation and

crystallographic parameters describing this interface were calculated using the experimental methods described in chapter 5, and are summarised below.

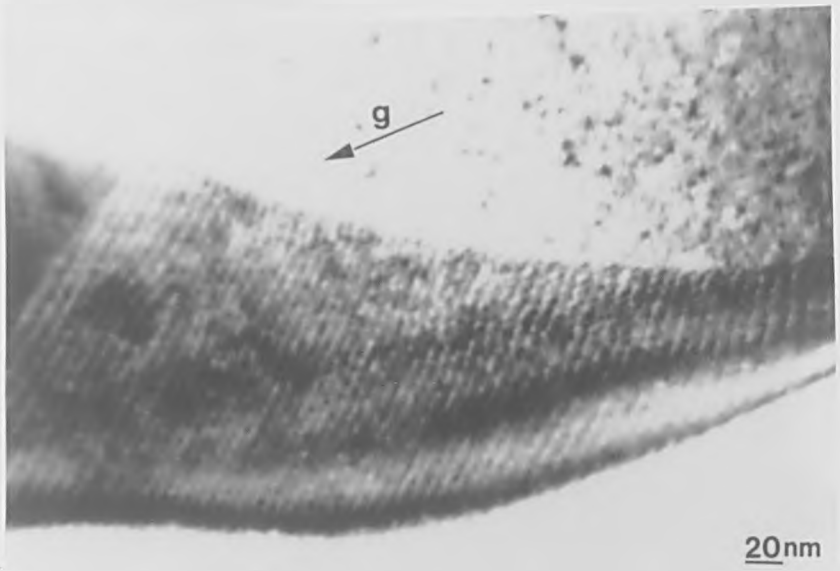

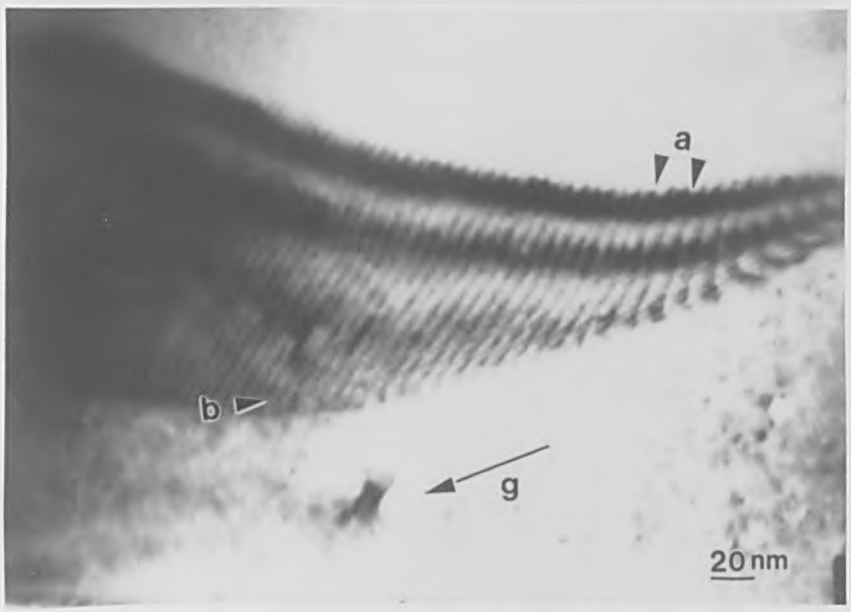

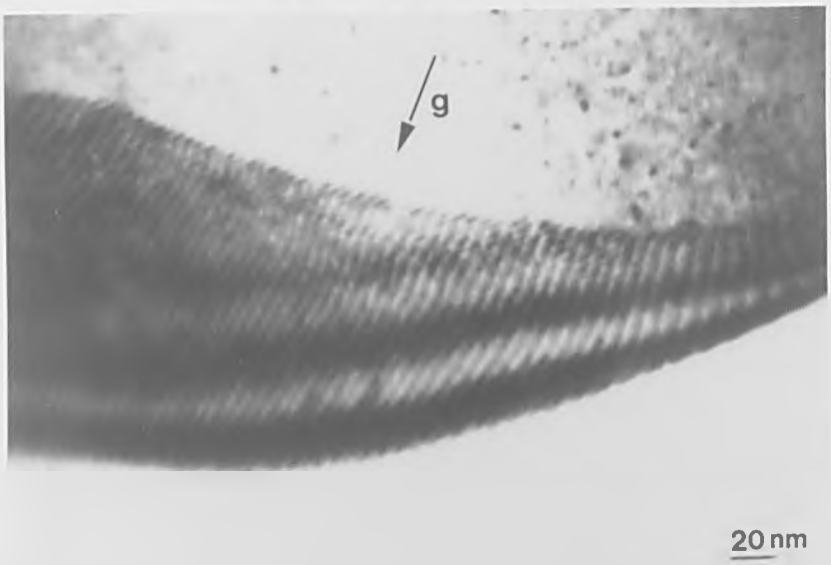

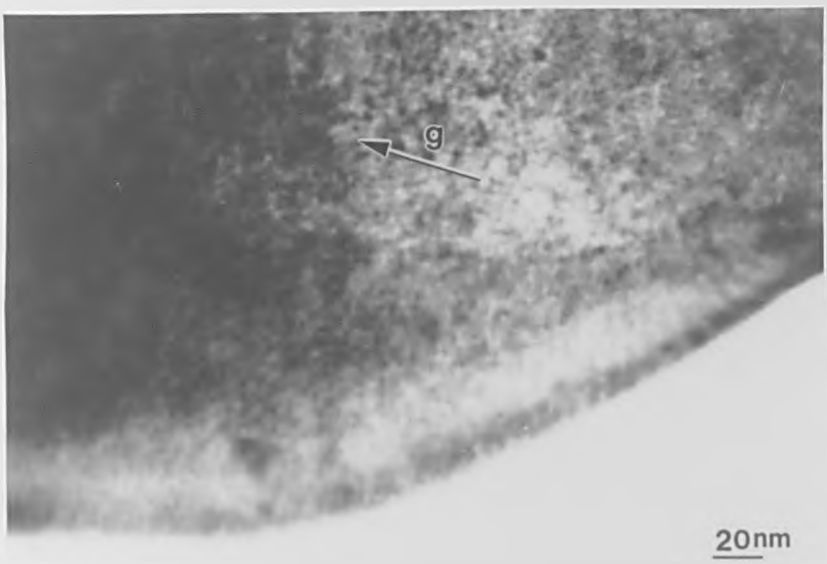

Fig 6.7: Bright field micrograph of grain boundary 1 imaged with (a) $g_{\mu}=0\bar{1}11$ and (b) $g_{\lambda}=10\bar{1}1$ (c) $g_{\lambda}=1\bar{1}01$ and (d) $g_{\lambda}=12\bar{1}2$.

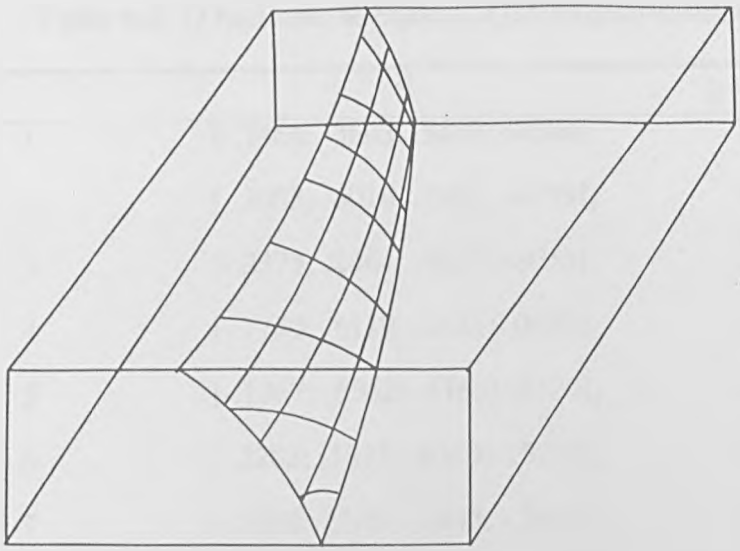

Fig 6.7: Schematic illustration of grain boundary 1 showing its non-planar nature.

(b) Grain boundary crystallography

The method presented in 5.2.3 gives one description of the relative orientation between the grains abutting at the interface. However, due to the symmetry exhibited by the constituent crystals, 12 equivalent descriptions can be derived using equation (5.27), and these are given in Table 6.2.

Due to the non-planar nature of this interface, the boundary plane normal, **n**, was determined in regions where the line direction of the observed defects appeared invariant. Such a region is denoted by arrows in Fig 6.6(a), and the boundary plane normal in this area is given by $\mathbf{n} = [0.0286; 0.6870; -.7156; 0.1218]_4$. The spacing of dislocations in set *b* could not be determined accurately from observations but is considerably smaller than that of dislocations in set *a* ($\approx$ 6.5 nm).

Table 6.2: 12 Equivalent descriptions of R/θ for grain boundary 1.

	R	θ (Degrees)
1	$[-.7466; .3663; .3803;-.4044]_4$	79.503
2	$[.3065;-.6016; .2951;-.6759]_4$	105.05
3	$[-.2373; .2464; .4837;-.8055]_4$	161.53
4	$[-.7740; .6119; .1621;-.0659]_4$	108.42
5	$[-.1367; .6552;-.5185;-.5320]_4$	146.65
6	$[.5203; .1371;-.6575;- .5272]_4$	145.33
7	$[-.5068;.7513; -.2443; -.3447]_4$	119.56
8	$[.7547;-.2453;-.5089; -.3333]_4$	118.72
9	$[.2111; .4380; -.6492; -.5848]_4$	179.50
10	$[.6862;-.6775;-.0848; -.2644]_4$	74.66
11	$[-.4869;-.0614; .4930; -.7209]_4$	115.10
12	$[-.0536; .4305; -.4258;-.8549]_4$	150.10

VI.2.2 Example of a planar grain boundary (grain boundary 2)

(a) Observations

Several micrographs of this planar boundary, imaged under different 2-beam diffracting conditions, are presented in Fig 6.8 (a-c). Although one set of dislocations is only visible on each of the micrographs, the presence of at least one other non-resolvable set is very likely. The orientation relationship and the crystallographic parameters representing the boundary are presented below.

(b) Grain boundary crystallography

The 12 equivalent descriptions associated with the boundary orientation are given in Table 6.3. The boundary plane normal, calculated using the methods introduced in 5.2.4, was determined with better accuracy in this case and was found to be

$[-0.5004;\ 0.0101;\ 0.4903;\ 0.7134]_4$. The spacing between the dislocations in the observed set was found to be ≈ 8.8 nm.

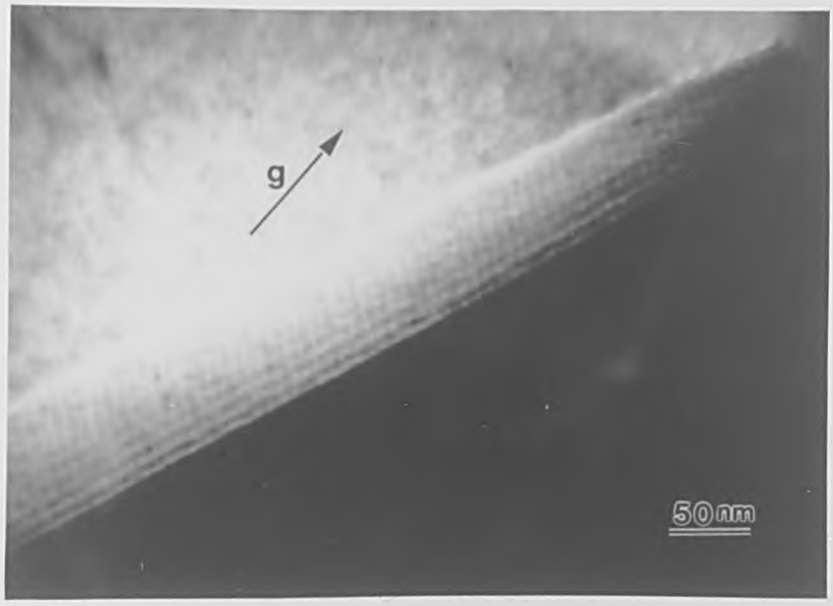

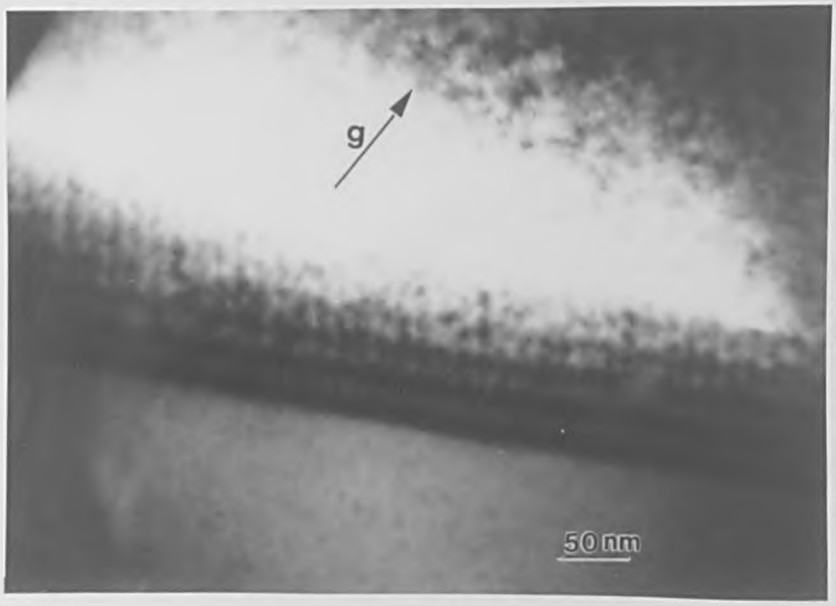

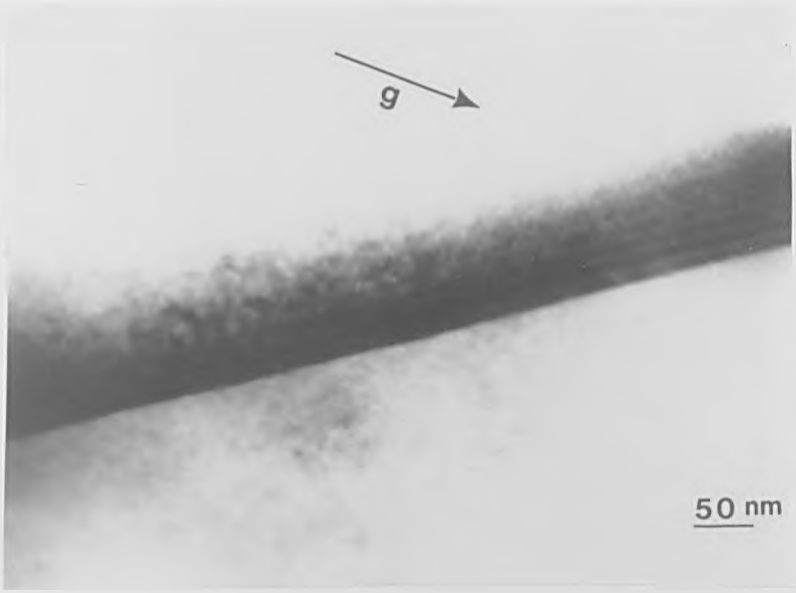

Fig 6.8: Bright field micrograph of grain boundary 2 imaged with (a) $g_{\mu}=0\bar{1}11$, (b) $g_{\lambda}=000\bar{1}$, (c) $g_{\lambda}=11\bar{2}0$.

Table 6.3: 12 Equivalent descriptions of R/θ for grain boundary 2

	R	θ (Degrees)
1	$[.6618;-.6832;.0213;-.3076]_4$	80.02
2	$[\ .0165;.5111;-.5277;-.6781]_4$	112.68
3	$[-.4494;.0140;.4353;.7799]_4$	155.55
4	$[-.7327;.5302;.2025;-.3753]_4$	117.17
5	$[-.2050;-.7418;.5368;-.3455]_4$	114.90
6	$[\ -.4526;-.1728;.6254;-.6116]_4$	178.03
7	$[-.5828;.7863;-.2034;-.0222]_4$	104.60
8	$[\ -.6505;.1687;.4817;-.5623]_4$	146.14
9	$[\ -.1704;-.4864;.6569;-.5501]_4$	142.63
10	$[\ .2668;.2424;-.5093;-.7814]_4$	157.18
11	$[-.3842;.7655;-.4010;-.3247]_4$	80.68
12	$[.6048;-.3168;-.2879;-.6714]_4$	111.27

VI.2.3 Example of a faceted Grain boundary (grain boundary 3)

(a) Observations

Images of this faceted boundary are presented in Fig 6.9 (a-b) for two operating diffracting vectors. Two sets of facets *a*, *c*, *e*, (set 1) and *b*, *d*, *f* (set 2) are clearly visible on these micrographs but no resolvable dislocation network was observed.

(b) Grain boundary crystallography

The orientation relationship between the constituent crystal was calculated as stated in section 5.2.4 and the 12 equivalent descriptions of the angle/axis pair representing this relationship are given in Table 6.4.

Table 6.4: 12 Equivalent descriptions of R/θ for grain boundary 3.

	R	θ (Degrees)
1	$[.6344;-.1612;-.4731;-.5895]_4$	30.04
2	$[-.1334;.1666;-.0331;-.9763]_4$	105.12
3	$[.0299;.1141;-.1440;-.9824]_4$	134.40
4	$[.8052;-.4870;-.3279;-.0829]_4$	155.32
5	$[.2767;-.7337;.4570;-.4197]_4$	179.98
6	$[-.4974;-.2900;.7832;-.2203]_4$	161.52
7	$[.6071;-.7112;.1040;-.3386]_4$	171.26
8	$[-.7571;.1440;.6130;.1734]_4$	152.71
9	$[-.1089;-.5918;.7007;-.3831]_4$	179.81
10	$[.1501;.0726;-.2209;.9610]_4$	78.58
11	$[-.3370;.2205;.1164;.9078]_4$	50.46
12	$[-.0460;.1395;-.0934;-.9847]_4$	158.29

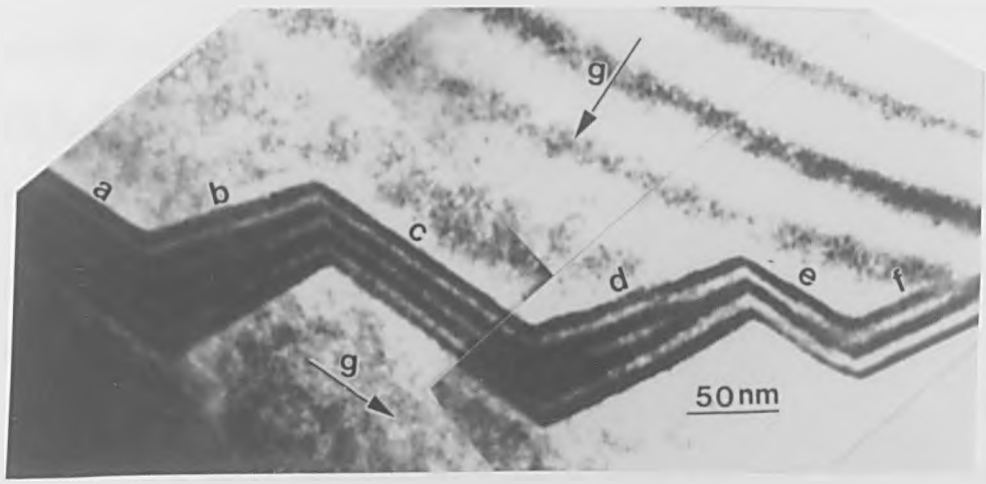

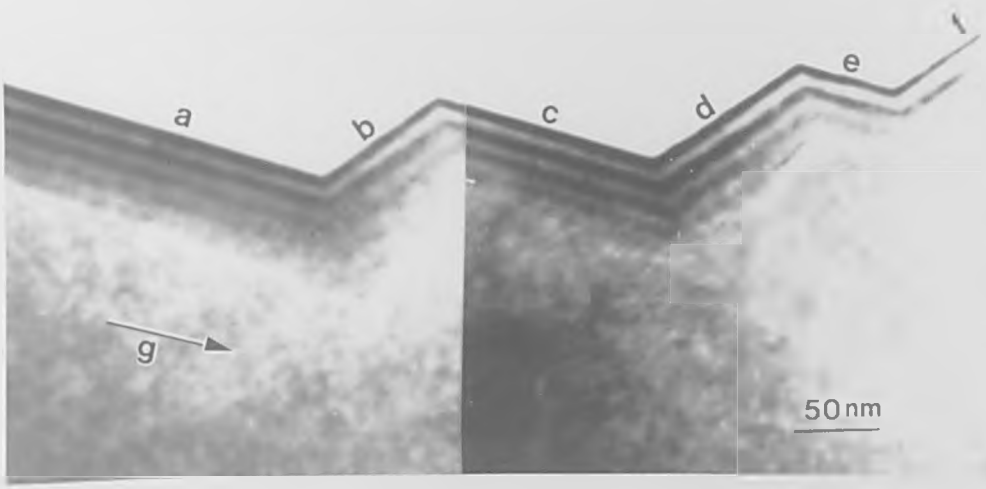

Fig 6.9: Bright field micrograph of grain boundary 3 imaged with (a) $g_{\mu}=0111$, (b) $g_{\lambda}=1011$

The intersection that the boundary plane makes with the specimen surface was used to calculate the normals $\mathbf{n}_1$ and $\mathbf{n}_2$ to set 1 and set 2 respectively. Using trace analysis, $\mathbf{n}_1$= [-.0.4503; 0.8056; -0.3551; 0.1480]$_4$ and $\mathbf{n}_2$= [0.1536; -0.1139; -0.0397;

$0.9807]_4$ and these directions are 0.83^0 and 3.31^0 away from the normals to $(\bar{4}731)$ and $(\bar{1}105)$ respectively.

VI.3 Analysis of Grain Boundaries in α-Alumina (sapphire)

Two discs of sintered α-alumina were obtained from the University of Birmingham, both had been heat treated at 1600° C for different cycle periods. Basic metallographic preparation and optical microscopy revealed numerous grain boundaries in both samples. X-ray diffraction was carried out on the as-received materials to confirm that no other phases were present. Numerous thin specimens were prepared from both discs following the method described in chapter 5, and a large number of boundaries were carefully imaged. However, none of the grain boundaries observed appeared to contain resolvable dislocation networks, and this result was thought to be associated with the presence of impurities segregated to grain boundaries. Samples containing high-angle grain boundaries were carbon-coated and imaged using scanning transmission microscopy (STEM) in order to determine segregant levels. Quantitative measurement of grain boundary segregation using STEM has historically been difficult and a method developed by Hunt and Seah [3] was used to obtain such information for boundaries appropriately oriented with respect to the electron beam (see chapter 5). The X-ray spectrum presented in Fig 6.10 is representative of the other boundaries studied. Peaks characteristic of the elements present in the matrix are represented by a dots and are compared with those corresponding to elements detected only in the grain boundary area . This spectrum clearly shows that significant levels of calcium and silicon segregated to the grain boundaries in both the materials studied, probably as CaO and SiO, as suggested by previous workers [4]. An estimation of the number of atoms of segregants detected per unit area of grain boundary suggested that these levels were consistent with a thick layer of contaminants at the grain boundary. Segregation plays an important role in the determination of grain boundary properties but is not the main objective of this work. Consequently, further investigation into the reasons associated with the absence of resolvable dislocation networks in the as-received

material was not pursued. However. it is suggested that the high concentration of segregants observed in the grain boundaries studied is directly linked to this result.

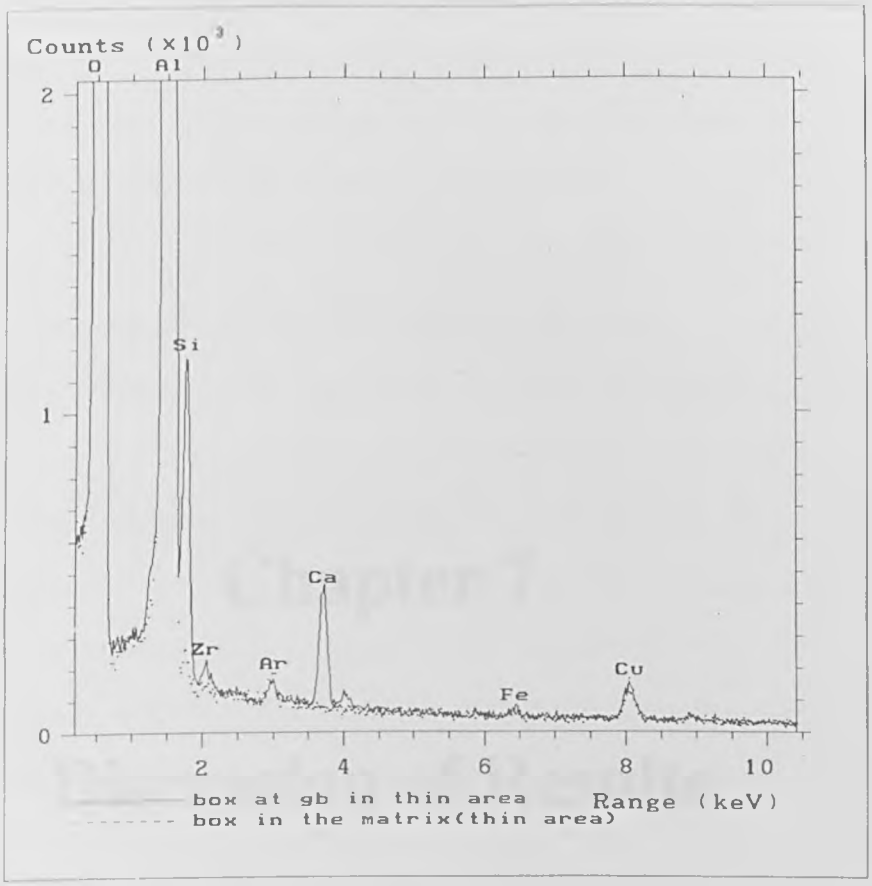

Fig 6.10: Energy Dispersive X-ray spectra from the matrix (dotted line), and from a region in the grain boundary.

References

1 Kiselev A.N., Sarrazit F., Stepantsov E.A., Olsson E., Claeson T., Bondarenko V.I., Pond R.C., Kiselev N.A., *Phil. Mag. A.*, **76**, p633 (1997).

2 Stepantsov E.A., USSR Patent N 1116100 cL C30B33100., *Bull. Isobretenii.* **36** (1986).

3 Hunt C.P., and Seah M.P., *Mat.Sci.Techn.*, **8**, p1023 (1992)

4 Susnitzky D.W. and Carter C.B., J.Am.Ceram.Soc., **69**, C-217 (1986)

Chapter 7

Discussion of Results

Overview

This chapter discusses the observations and results presented in chapter 6 in more detail. First, a complete topological analysis of the features observed in ZnO grain boundaries is presented and aspects of the structure adopted by such interfaces is discussed. The second part of this chapter focuses on the characterisation of interfacial features in WC, and describes the suitability of specific reference structures for the description of the grain boundaries observed in this study.

VII.1 Analysis Of Grain Boundaries In ZnO

Two bicrystals, with large interfacial areas and misorientations close to approximately 19^0 and 30^0 about [0001], were successfully prepared at the Institute of Crystallography (Russia) using the Solid-Phase Intergrowth (SPI) technique[1]. Surface orientations and their mutual alignment were first determined using an X-ray diffractometer technique [2], and experimental orientations were determined from selected area diffraction patterns. Successful preparation of bicrystals by SPI requires smooth surfaces of the component crystals to be prepared by cutting and polishing, followed by pressing these together at an elevated temperature (generally in the range 1200 -1800)^{0}C. The experimental orientation relationship between the adjacent crystals was found to be 17.8 ± 0.1^0 for the bicrystal with target misorientation angle $\theta_t=19^0$ and 31.5 ± 0.1^0 for the bicrystal with target $\theta_t=30^0$. Dichromatic patterns arise from the interpenetration of the lattices of the λ and μ crystals and are useful as reference spaces for the specification of defect content in experimentally observed interfaces. In the present work, the most appropriate ones were found to correspond to "special" misorientations represented by the periodic patterns $\Sigma=31$ and $\Sigma=13$ in CSL terminology (see chapter 6). In the following, the term "special", attributed to a boundary, refers to the fact that the measured experimental misorientation between the adjacent crystals is very close to that of a periodic CSL pattern. A detailed analysis of

the topological features observed in two of the ZnO boundaries imaged by the russian group is presented in the following sections.

VII.1.1 17.8° tilt boundary

The experimental misorientation for this boundary was found to be very close to that for the periodic pattern Σ=31 (17.89° /[0001]), as stated above, and the latter configuration was therefore chosen as the reference space for the characterisation of interfacial defects present in this boundary. The orientation of the interface is close to the plane PM in Fig 6.1b, that is close to the $(\bar{8}\ 17\ \bar{9}\ 0)_\lambda$-$(\ \bar{3}\ 16\ \bar{13}\ 0)_\mu$ periodic interface. This can be confirmed by using the circuit SXF indicated in Fig 6.2 for which **c**(λ)=**SX**=1/3[$\bar{52}$ 2 $\bar{50}$ 0]$_\lambda$ and **c**(μ)=**XF**=1/3[58 $\bar{20}$ $\bar{38}$ 0]$_\mu$. This interface is inclined by 8.9° to the target λ surface $(1\ \bar{3}\ 2\ 0)_\lambda$ and 10.2° to the target μ surface $(0\ 1\ \bar{1}\ 0)_\mu$. It is also interesting to note that this asymmetric interface, which exhibits a relatively long period does not facet into combinations of symmetric $(\bar{7}\ 11\ \bar{4}\ 0)_\lambda$ and $(\bar{1}\ 6\ \bar{5}\ 0)_\mu$ interfaces (PL and LM in Fig 6.1b). The region emcompassed by the circuit indicated in Fig 6.2 was found to be at the exact CSL orientation, i.e when mapped into the reference space, **c**(λ,μ)=**0**. However, occasional defects were detected in other parts of the boundary. Fig 6.3 is an example of such a region , where the Burgers content of the segment encircled by the circuit is **b**=1/93 [7 $\bar{11}$ 4 0].This value is consistent with **t**(λ)= 1/3[$\bar{4}$150] and **t**(μ)= 1/3[$\bar{5}$140], the shortest crystal translation vectors leading to the smallest-magnitude values of the Burgers vector of admissible defects according to equation (3.2). Thus, The circuit shown in Fig 6.3 encompasses an interfacial edge dislocation with minimum magnitude **b**. In order to fully characterise this dislocation topologically, the step heights associated with its

formation are now considered. The defect character of interfacial defects can be imagined to arise as a consequence of bonding together surfaces exhibiting incompatible steps. The height of these steps is given by $h(\lambda) = \mathbf{n}.\mathbf{t}(\lambda)$ and $h(\mu) = \mathbf{P}^{-1}\mathbf{n}.\mathbf{t}(\mu)$ in the white and black crystals respectively, where $\mathbf{n}$ is the normal to the interface locally, and $\mathbf{t}(\lambda)$ and $\mathbf{t}(\mu)$ are the translation vectors to be substituted in equation (3.2) . Experimentally, these heights are calculated from $h(\lambda) = \mathbf{n}.\mathbf{C}(\lambda)/d_{(hkil)}$ and $h(\mu) = \mathbf{P}^{-1}\mathbf{n}.\mathbf{C}(\mu)/d_{(hkil)}$, where $d_{(hkil)}$ is the interplanar spacing of the lattice planes parallel to the interface in either of the crystals, and $\mathbf{C}(\lambda) = \mathbf{SX}_{\lambda} = 1/3[\bar{2}2\ 2\ 20\ 0]_{\lambda}$ and $\mathbf{C}(\mu) = \mathbf{XF}_{\mu} = 1/3[\bar{8}\ \bar{3}\ 5\ 0]_{\mu}$ have their usual meaning (see chapter 3, section III-4). By comparing experimental and theoretical step heights with observations, the specific values of $\mathbf{t}(\lambda)$ and $\mathbf{t}(\mu)$ which characterise the defect can then be determined. The step heights associated with the defect above, expressed in units of $d_{(\bar{8}\ 17\ \bar{9}\ 0)\lambda}$, were found to be $h(\lambda) = -10$ and $h(\mu) = -7$ in the λ and μ crystals respectively. Again, these values are consistent with the vectors $\mathbf{t}(\lambda)_1 = [\bar{4}150]$ and $\mathbf{t}(\mu)_1 = [\bar{5}140]$ in equation (3.2), and a schematic diagram illustrating the defect formation is shown in Fig 7.1(a). Due to the sign of $\mathbf{t}(\lambda)_1$ and $\mathbf{t}(\mu)_1$, the configuration depicted in Fig 7.1(a) exhibits re-entrant steps which are not consistent with the observation shown in Fig 6.3. However, alternative configurations can arise due to the periodic nature of the interface, and the steps associated with these are obtained by adding translation vectors of the $\Sigma = 31$ dichromatic pattern to $\mathbf{t}(\lambda)_1$ and $\mathbf{t}(\mu)_1$. If a translation vector $\mathbf{t}$ equal to $1/3\ [26\ \bar{1}\ \bar{25}\ 0]_{\lambda}$ is added to both $\mathbf{t}(\lambda)_1$ and $\mathbf{t}(\mu)_1$ in Fig 7.1, a configuration consistent with the experimental observation is obtained as depicted in Fig 7.1(b). Indeed, the resulting

translation vectors $\mathbf{t}(\lambda)_2$ and $\mathbf{t}(\mu)_2$ in Fig 7.1 (b) correspond exactly to the vectors $\mathbf{Xs}_\lambda$ and $\mathbf{Xs}_\mu$ indicated in Fig 6.3, and the features observed in this region of interface are therefore consistent with the topological theory. The defect characterised here is a primitive interfacial edge dislocation exhibiting a long step riser ($\mathbf{Xs}_\lambda$ in Fig 6.3). A possible reason for this configuration as opposed to that depicted in Fig 7.1(a) is the minimisation of the interfacial area and reduction of the core and elastic energy of the dislocation.

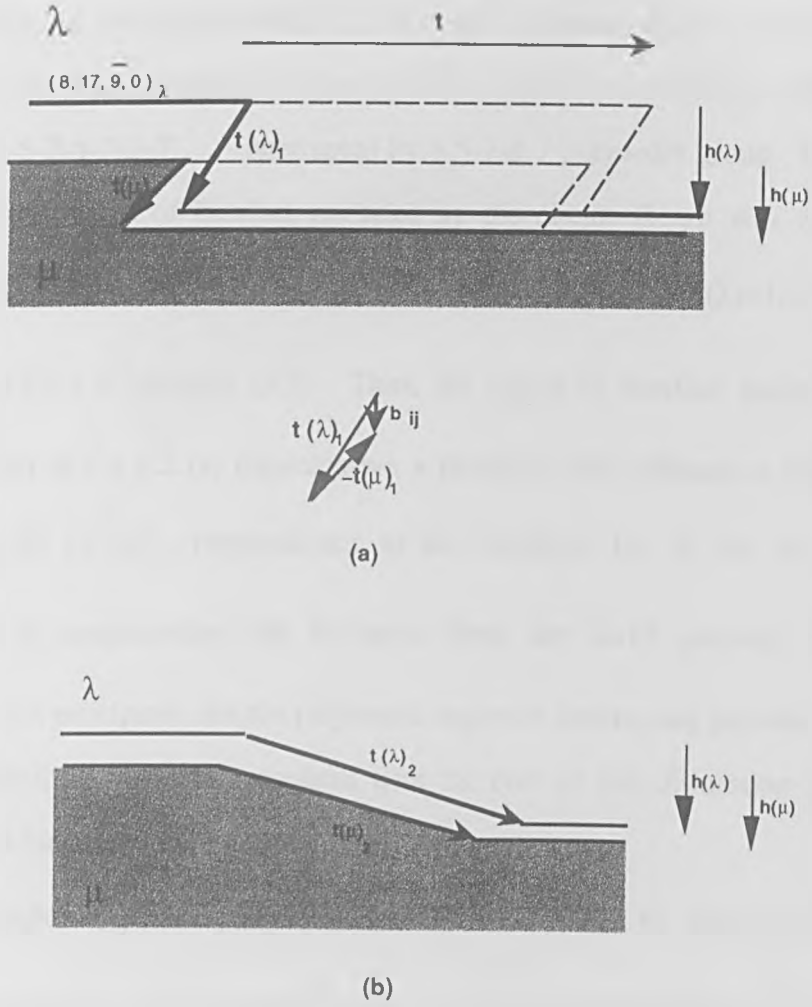

Fig 7.1: Schematic illustration of the formation of an interfacial defect with b= 1/93 [7 $\bar{11}$ 4 0] in the Σ=31, ($\bar{8}$ 17 $\bar{9}$ 0) interface, showing the incompatible steps on the adjacent crystal surfaces before bonding; (a) re-rentrant steps configuration and (b) alternative description.

VII.1.2 31.5^0 tilt boundary

An example of a 31.5^0 boundary exhibiting several facets is illustrated in Fig 6.4. Two pairs of facets, *A* and *C*, and *B* and *D*, with orientation close to the planes PR and TR in Fig 6.4 respectively, were observed. The structure of facets D and C are analysed separately below and the overall structure of this boundary is subsequently discussed.

(a) Facet D

A filtered image of facet D, showing several periods of the $(\bar{2}7\bar{5}0)_\lambda$ interface (TR in Fig 6.1 (b)), is presented in Fig 6.5 (a). As illustrated on the micrograph, the boundary comprises a sequence of five-, six- and seven-fold polyhedra with repeating pattern ...5-6-7-5-7-5-7...., interrupted by a 5-7-5-7 polyhedra group. The Burgers content of the region of interface encircled by the circuit shown was found to be $\mathbf{b}= 1/39\ [\bar{2}7\bar{5}0]_\lambda$, and this is consistent with translation vectors $\mathbf{t}(\lambda)=1/3[\bar{7}\bar{2}\bar{5}0]$ and $\mathbf{t}(\mu)=1/3\ [\bar{7}\bar{5}\bar{2}0]$ in equation (3.2) . Thus, the region of interface encircled by the circuit shown in Fig 6.5 (a) encompasses a primitive edge dislocation with Burgers vector $\mathbf{b}=1/39\ [\bar{2}7\bar{5}0]_\lambda$, perpendicular to the interface, i.e. in the most efficient orientation to accommodate the deviation from the $\Sigma=13$ periodic orientation. Moreover, it is anticipated that the polyhedral sequence interrupting periodic regions of interface identified above is associated with the core of this dislocation and this is investigated further below.

The step heights $h(\lambda)$ and $h(\mu)$ associated with the defect can be determined following a procedure similar to that described in VII.1.1.Using the values of $\mathbf{t}(\lambda)$ and $\mathbf{t}(\mu)$ given above leads to values consistent with experimental step heights and equal to $h(\lambda)=-1$ and $h(\mu)=1$ in units of $d_{(\bar{2}7\bar{5}0)}$. A schematic illustration of the topological significance

of this result is shown in Fig 7.2 (a), together with its equivalence with the polyhedron model discussed earlier (Fig 7.2(b)). As anticipated earlier, the 5-7-5-7 polyhedral group is directly associated with the vectors $\mathbf{t}(\lambda)$ and $\mathbf{t}(\mu)$ given above and this localised region of interface is therefore associated with the the core of the discontinuity.

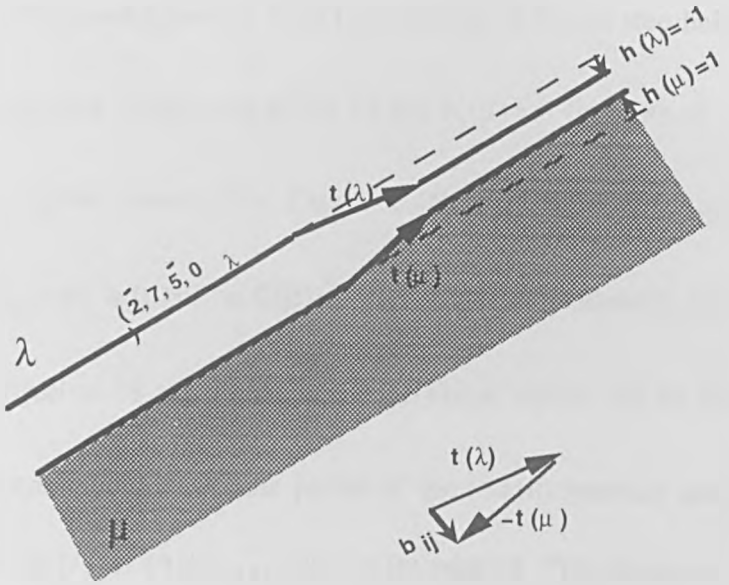

(a)

Fig 7.2: Schematic illustration of the incompatible surface steps on the λ and μ crystals before bonding in the Σ=13, $(2\,7\,5\,0)$ interface and (b) core structure of the defect defined in terms of topological parameters and polyhedral units.

(b) Facet C

A circuit was constructed around facet C as illustrated in Fig 6.5, and subsequently mapped into the Σ=13 dichromatic pattern. This led to the characterisation of a primitive interfacial defect with Burgers vector **b**= 1/39[$\bar{5}\bar{2}70$]; i.e. inclined by 60^0 to the main $(13\bar{4}0)_\lambda$ facet orientation. This result is consistent with the shortest translation vectors **t**(λ)=[$10\bar{1}0$] and **t**(μ)=1/3[$4\bar{2}\bar{2}0$] in equation (3.2) and step heights calculated from these values were found to be $h_1(\lambda)=5$ and $h_1(\mu)=6$ (in units of $d_{(13\bar{4}0)}$) in the white and black crystal respectively. Experimental step heights, calculated from $h_2(\lambda)$ $=\mathbf{n}.\mathbf{C}(\lambda)/d_{(13\bar{4}0)\lambda}$ and $h_2(\mu)=\mathbf{P}^{-1}\mathbf{n}.\mathbf{C}(\mu)/d_{(13\bar{4}0)\mu}$, were considerably larger than $h_1(\lambda)$ and $h_1(\mu)$ and equal to 18 and 19 respectively. These values can be understood if a defect-free step corresponding to one period of the $(\bar{3}\bar{4}10)$ interface and characterised by $h_3(\lambda)=h_3(\mu)=\mathbf{n}.1/3[5\bar{2}70]/d_{(13\bar{4}0)}=13$, is introduced. This situation is represented schematically in Fig 7.3(a). Based on this description, $h_2(\lambda)$ may be regarded as the combination of $h_1(\lambda)$ and $h_3(\lambda)$ in the white crystal, and similarly, $h_2(\mu)$ may be regarded as a combination of $h_1(\mu)$ and $h_3(\mu)$ in the black. Although the arguments advanced above are in good agreement with the topological analysis of the defect, the resulting configuration depicted in Fig 7.3(a) does not correspond to the experimental observation shown in Fig 6.5 (b). Indeed, this image clearly shows a horizontal segment separating $(13\bar{4}0)$ periodic regions of interface. Its orientation was found to correspond exactly to the abutment of the target $(0\bar{1}10)_\lambda$ and $(1\bar{1}20)_\mu$ crystal surfaces and a schematic illustration of this situation is shown in Fig 7.3 (b). It is therefore

anticipated that the boundary structure has transformed locally from the configuration depicted in Fig 7.3 (a) to that in Fig 7.3 (b) and this issue is discussed further below.

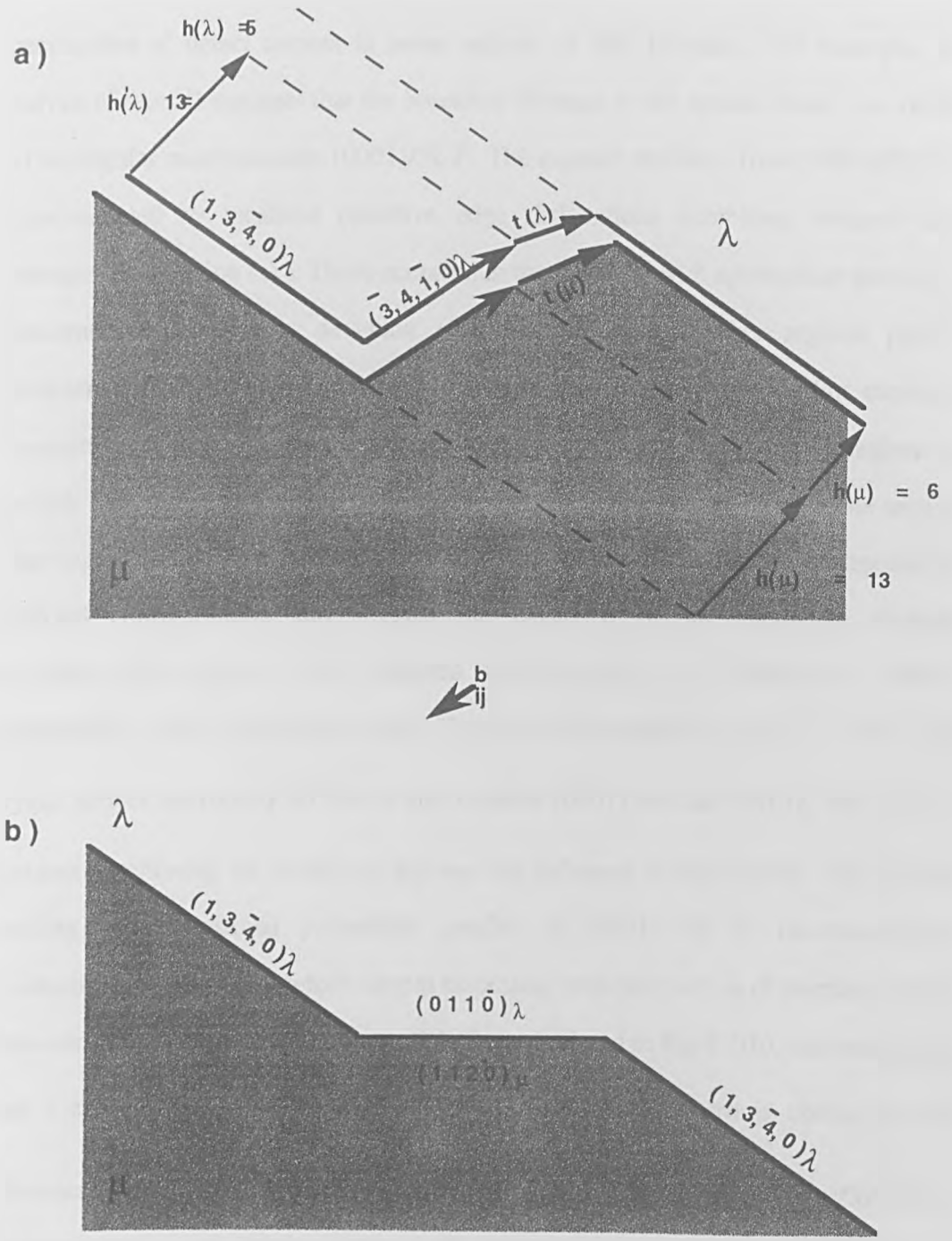

Fig 7.3: Schematic illustration of (a) the total step height and Burgers vector of a combined defect-free step (one period of the $(\bar{3}410)$ interface) and primitive interfacial dislocation with $\mathbf{b}=1/39[\bar{5}270]$. (b) the observed configuration including the $(0\bar{1}10)_\lambda$ - $(\bar{1}120)_\mu$ horizontal interface.

(c) General discussion on the structure of the 31.5^0 boundary

As discussed in (b), the overall boundary orientation is very close to that for the dichromatic pattern Σ=13, and this reference space is therefore very useful for the specification of defect content in some regions of this interface. For example, the analysis of facet D suggests that the boundary belongs to the special class, i.e. vicinal to the singular misorientation [0001]/32.2^0. The angular deviation from [0001]/32.2^0 is accommodated by localised primitive edge dislocations exhibiting compact core structures (see section (a)). These occurred in the interface with appropriate spacing to accommodate the angular deviation efficiently. However, other regions present characteristics which do not conform to this special-boundary model. For example, examination of facet C shows a horizontal segment of interface separating regions of periodic structure. More extensive portions of horizontal segments can also be seen in other regions, such as facet E in Fig 6.4. These observations do not correspond to expected configurations and suggest the existence of an alternative singular misorientation close to that observed experimentally. A dichromatic pattern characteristic of the horizontal portion of interface is represented in Fig 7.5 . Here, the crystal lattices are rotated 30^0 about the common [0001] and the $(0\bar{1}10)_\lambda$ and $(\bar{1}120)_\mu$ surfaces constituting the horizontal segment are indicated in each crystal. This pattern exhibits one-dimensional periodicity parallel to [0001] but is incommensurate perpendicular to this. The defect content associated with this portion of interface can be determined by constructing a circuit **S'X'F'** as depicted in Fig 6.5(b), and mapping it into a chosen reference space. If the Σ=13 dichromatic pattern is chosen as this reference, the circuit encompasses a dislocation with Burgers vector **b**=1/39[$\bar{5}\bar{2}70$] (see section b), and, on the basis of the observed step heights, the configuration depicted in Fig 7.3 (a) is expected. On the other hand, when mapped into the incommensurate pattern, the circuit closes, indicating that the defect content relative to this reference is zero and that the orientation adopted by this segment is exactly that of the [0001]/30^0 pattern. It is therefore suggested that the boundary structure exhibits

two coexisting but distinct structural forms. One form designated "special" which comprises localised dislocations superimposed on two-dimensionally periodic facets, and one which is planar, periodic in one direction but incommensurate perpendicular to this, and does not exhibit localised defects in the segments observed. It is anticipated that the relative proportion of the two structural forms would vary systematically with changing misorientation, comprising entirely the special form for [0001]/32.5^0 and correspondingly the incommensurate form for [0001]/30^0. In addition, it is suggested that the planar facet has transformed locally from the special configuration shown in Fig 7.3 (a) to the incommensurate form illustrated in Fig 7.3 (b). It is also suggested that the driving force for this transition reflects both the relative free energies of the two forms and geometrical factors. These aspects are discussed further below.

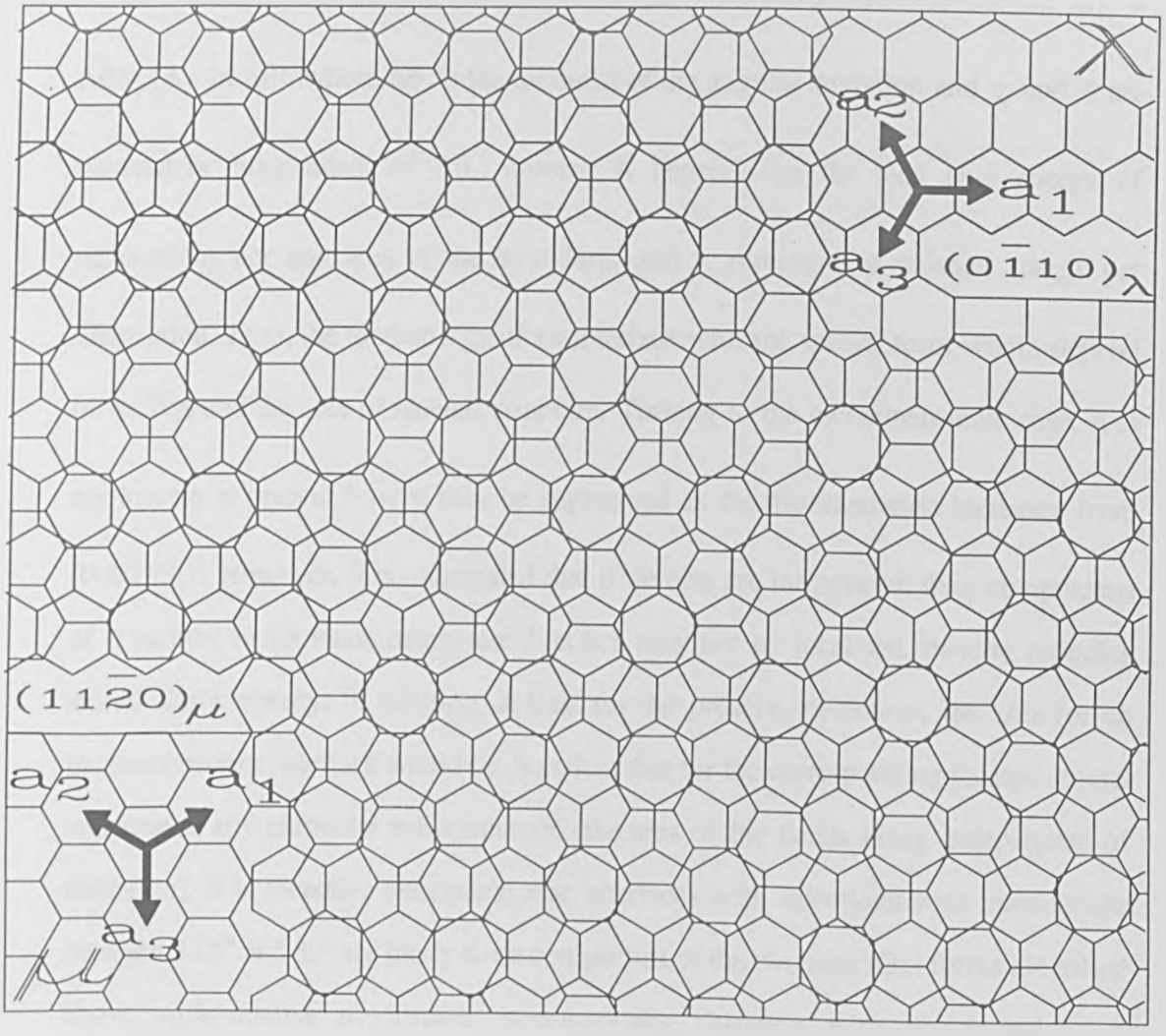

Fig 7.5: Dichromatic pattern formed by rotation of hexagonal lattices by 30^0 about [0001].

The systematics of grain boundary energies have been extensively studied (see [3] for a review) and it emerged that such interfaces tend to adopt low-energy configurations which depend on the misorientation between the adjacent crystals [4]. On the basis of this argument, and if the free energy per unit area of the special form (γ_s) is taken to be less than that for the incommensurate configuration (γ_i) at their respective singular misorientations, the formation of the special form will then be favoured at misorientations close to [0001]/32.5^0. However, due to the introduction of dislocations at lower disorientations, γ_s will be augmented by $\Delta\gamma_s$ and progressively the formation of the incommensurate form will be favoured. It is reasonable to expect $\Delta\gamma_s$ to be given by an expression resembling that for the energy of low-angle boundaries, i.e. $\Delta\gamma_s = \Delta\theta\ \gamma_o\ (A - \ln \Delta\theta)$, where $\Delta\theta$ is the modulus of the angular deviation and γ_o and A are parameters independent of $\Delta\theta$. Indeed, A depends on the total core energy of dislocations per unit area of the boundary, and γ_o represents a constant energy per dislocation. Thus, the total energy of an interface with the special form would depend on γs, $\Delta\gamma$s and the area of faceted structure. Turning to the incommensurate case, it is not known at present how γ_i may be augmented as the misorientation increases from [0001]/30^0. However, it is anticipated that if defects are introduced, their components of **b** parallel to the incommensurate direction may not be localised, thereby reducing stored elastic energy. In addition, at least for the present specimens, the area for an incommensurate interface would be less than that for the corresponding faceted special structure at any particular misorientation (the area of the facets being independent of their size). It is therefore anticipated that interfaces with misorientations intermediate between 32.5^0 and 30^0 are likely to be composites of the two structural forms identified above with relative proportions systematically changing with disorientation. A schematic illustration of the singular and composite structural forms in this

misorientation range is shown in Fig 7.6. The exact proportions of the two structural forms in a composite interface will depend on the energy and geometrical factors outlined above, and also on other thermodynamic variables such as temperature, stress and impurity segregation. The transition is thermodynamically irreversible, and there is probably hysteresis between transformations from special to incommensurate and vice-versa. It is also interesting to note that the abutting facets of the incommensurate segment of interface, schematically represented in Fig 7.3, correspond to low-index planes in the adjacent crystals. This would suggest a correlation between the atomic density of the planes comprising the grain boundary and the grain boundary energy, with widely spaced low-index planes displaying lower grain boundary energies. Previous work by Wolf and Merckle [5], who performed an extensive comparison between atomistic modeling and HREM observation of grain boundary structures, indicate that deep cusps corresponding to low energies exist for those configurations exhibiting low-index planes parallel to the grain boundary. This result is therefore consistent with the observation presented in this work. it is proposed that this observation (thought to be the first) suggests a mechanism whereby special boundaries transform into more general types as the crystallographic parameters pertaining gradually change.

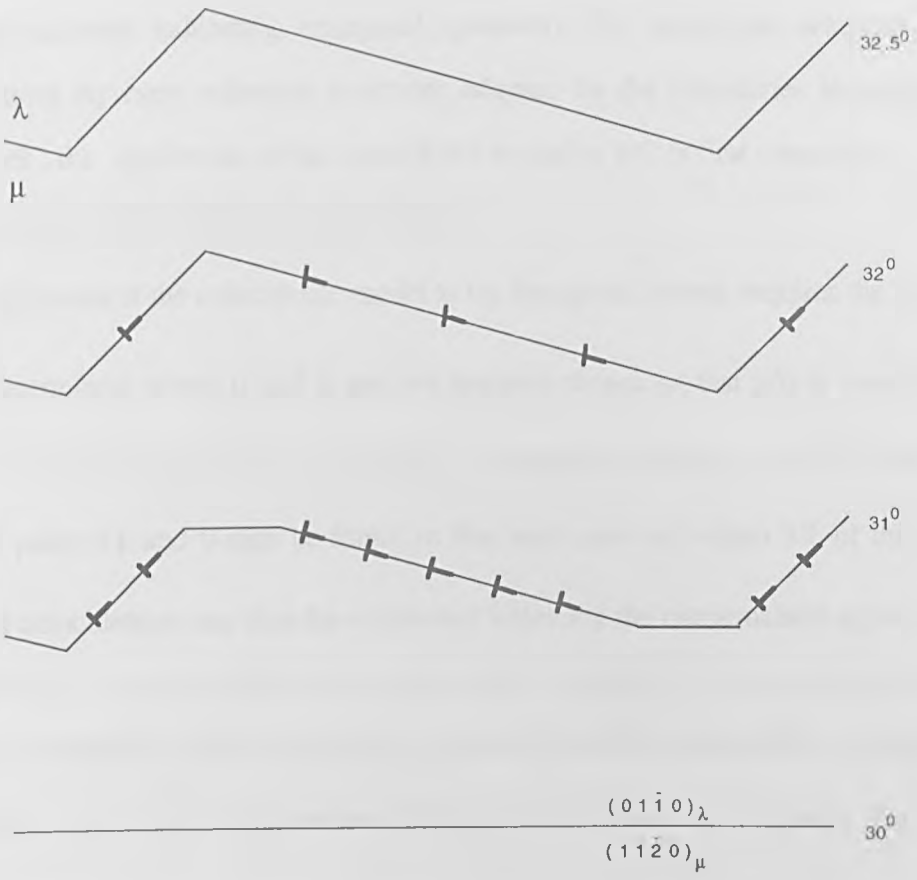

Fig 7.6 : Schematic illustration of the composite structural form of boundaries with misorientations intermediate between the singular values [0001]/32.50 (special) and [0001]/30^0 (incommensurate).

VII.2 Analysis Of Grain Boundaries In WC

This section discusses the structure of three grain boundaries in a grade of WC sintered in the absence of a binder phase. Observations of these boundaries are presented in chapter 6, together with the crystallographic parameters relevant to this analysis. As discussed in the previous section, it is useful to identify a singular orientation acting as a reference in order to interpret the experimental features observed at interfaces. There is much experimental and theoretical evidence that periodic structures corresponding to special orientations are suitable references, especially in cubic materials (see [6] for a review), however, there is less evidence that this is the

case in materials exhibiting hexagonal symmetry. To investigate whether special orientations represent reference structures adopted by the boundaries investigated in this work , the application of the coincidence model to WC is first considered.

VII.2.1 Coincidence Models applied to WC

The application of the coincidence model to the hexagonal system requires the ratio μ/υ to be determined; where μ and υ are two integers chosen so that μ/υ is very close to $(c/a)^2$ for the material under investigation. For tungsten carbide, $(c/a)^2=(0.976)^2$ and several pairs of μ and υ may be found so that their ratio fall within 3% of this value. Lists of coincidences may then be established following the mathematical approach due to Bleris [7], and these have been published by Hagege [8]. In most cases, these tables are limited to a few coincidences, and experimentally-determined misorientations are rarely close to such orientations. However, for $\mu/\upsilon=1$ (i.e. c/a=1), the list of coincidences comprises 92 cases for which $\Sigma \leq 50$, and experimental data may then be matched to a specific orientation. The ratio c/a=1 was therefore used in the following to determine the possible vicinity of the boundaries studied to special orientations.

VII-2-2 Structure of a non-planar grain boundary.

Several images of this boundary, obtained under different diffraction conditions are presented in Fig 6.6 (A to D). As discussed in VI.2.1(a), at least two sets of dislocations labeled *a*, and *b*, indicated by arrows, are visible on some of the micrographs. The misorientation between the adjacent crystals was found to be $[-.7466, .3663; .3803; -.4044]_4$ and 12 equivalent angle/axis pairs describing this misorientation are given in Table 6.2. In order to determine whether any of these are close to special orientations, each description was converted to Miller-Bravais indices and compared with the list of coincidences obtained with c/a=1. Again, the term "special" relates to CCSL configurations which form at "special" misorientations between the lattices of the adjacent crystals. Following this procedure, description n°

11 (Table 6.2) was found to be close to $[\bar{1}01\bar{2}]_{MB}/115.10^0$, which, in CSL terminology is identified as a $\Sigma=10$ boundary . Both the CSL and experimental matrices corresponding to these orientations were determined by the methods described in V.2.4, and these are given below

$$\mathbf{R}_{csl} = 1/30 \begin{bmatrix} 11 & 26 & -7 & \frac{6}{\Lambda} \\ 2 & 2 & 26 & \frac{12}{\Lambda} \\ 17 & 2 & 11 & \frac{-18}{\Lambda} \\ \frac{18}{\Lambda} & \frac{-12}{\Lambda} & \frac{-6}{\Lambda} & 12 \end{bmatrix}_4 \text{ and}$$

$$\mathbf{R}_{exp} = \begin{bmatrix} .3882 & .8558 & -.2441 & .2389 \\ .1020 & .0505 & .8473 & .5186 \\ .5097 & .0935 & .3967 & -.7576 \\ .7609 & -.5060 & -.2548 & .3160 \end{bmatrix}_4,$$

where R_{csl} and R_{exp} represent the $\Sigma=10$ and experimental misorientations respectively and $\Lambda=(2/3)^{1/2}$. Assuming that the $\Sigma=10$ singular orientation is the reference structure adopted by this boundary, the experimental deviation from this configuration can be calculated as explained in v.2.4, and is given by

$$R_{dev}/\theta_{dev} = [0.7638; -.5853; -.1736; -.2091]_4/4.78^0.$$

This result suggests a relatively large deviation about an axis $\approx 73^0$ away from the boundary plane normal **n** calculated in section VI.2.1(b). Due to the relative difficulty in imaging the dislocations in set *b* , the characterisation of these defects was not attempted. However, dislocations in set *a* were strongly visible under all the diffraction conditions used, and the *a-priori* approach described in section III.3.1 was used to characterise them topologically. As discussed in this section, the Burgers vectors of admissible interfacial dislocations are given by equation (3.2), where the matrix **P** represents the matrix associated with reference misorientation ($\mathbf{R}_{ccsl}$ in this case), and $\mathbf{t}(\lambda)$ and $\mathbf{t}(\mu)$ are translation vectors in the λ and μ crystal respectively.

Theoretically speaking, any translation vectors belonging to the space group $P\bar{6}m2$ may be substituted in equation (3.2), resulting in a large number of possible values for **b**. Feasible values, however, are those with small magnitude ($|\mathbf{b}|<a$), obtained by the combination of relatively short $\mathbf{t}(\lambda)$ and $\mathbf{t}(\mu)$, and making an angle close to 90^0 with r_{dev} (hence accommodating the deviation in the most efficient way). A list of possible candidates for **b**, which all satisfy the specifications discussed above, is presented in Table 7.1. Based on the low contrast displayed when $\mathbf{g}=\bar{1}2\bar{1}2/\Lambda$, the most likely value for **b** would be $[.015;.424;.439;.334]_4$ (see section IV.3), and this should be checked using contrast simulation techniques. Unfortunately, such methods require further developments and it was therefore impossible to comment on the validity of the arguments advanced above.

Table 7.1: List of admissible Burgers vectors for the dislocations in set a .

t(λ)	t(μ)	**b** = **t**(λ)-**Pt**(μ)	Angle with R_{dev}
$[000\bar{2}\Lambda]_4$	$1/3[22\bar{4}0]_4$	$[.151;.242;\ 0.\bar{3}9\bar{3};\ .074]_4$	83.04^0
$[0\bar{1}1\Lambda]_4$	$[0\bar{1}10]_4$	$[.045;.272;0.318;.185]_4$	86.35^0
$[0\bar{1}10]_4$	$1/3[\bar{1}2\bar{1}0]_4$	$[.\bar{1}21;.393;.\bar{5}15;.222]_4$	90.04^0
$1/3[\bar{1}453\Lambda]_4$	$1/3[\bar{1}\bar{1}23\Lambda]_4$	$[.\bar{0}15;.424;.439;.334]_4$	82.70^o
$[\bar{1}012\Lambda]_4$	$1/3[\bar{4}\bar{1}56\Lambda]_4$	$[.\bar{0}75;.\bar{1}21;.196;.\bar{7}79]_4$	80.07^0
$1/3[\bar{2}\bar{1}13\Lambda]_4$	$1/3[\bar{4}\bar{1}56\Lambda]_4$	$[.045;.272;.\bar{3}188;.\bar{1}85]_4$	93.64^0

VII.2.3 Structure of a planar grain boundary.

Images of this boundary can be found in section VI.2.2 together with details of the experimental parameters associated with its crystallography. Although only one set of dislocations, indicated by arrows in Fig 6.8, displayed strong contrast under the range of diffraction conditions used here, it is believed that at least one other set of dislocations, not resolvable in the microscope, is present. The misorientation between adjacent grains was determined experimentally using the methods presented in V.2, and was found to be $[0.6618; -0.6832; 0.0213; -0.3076]_4$ / 80.02^0 and equivalent descriptions are given in Table 6.3. Description n° 3, being very close to the orientation $[\bar{1}\bar{0}\bar{1}2]_{MB}$ / 155.38^0 (Σ=22b in CSL terminology), was chosen as a possible reference structure for this boundary as no other description appeared to be close to alternative singular orientations. A schematic of the Σ=22b dichromatic pattern in that orientation is illustrated in Fig 7.7. The rotations matrices corresponding to the coincidence (R_{csl}) and experimental (R_{exp}) orientations are given below.

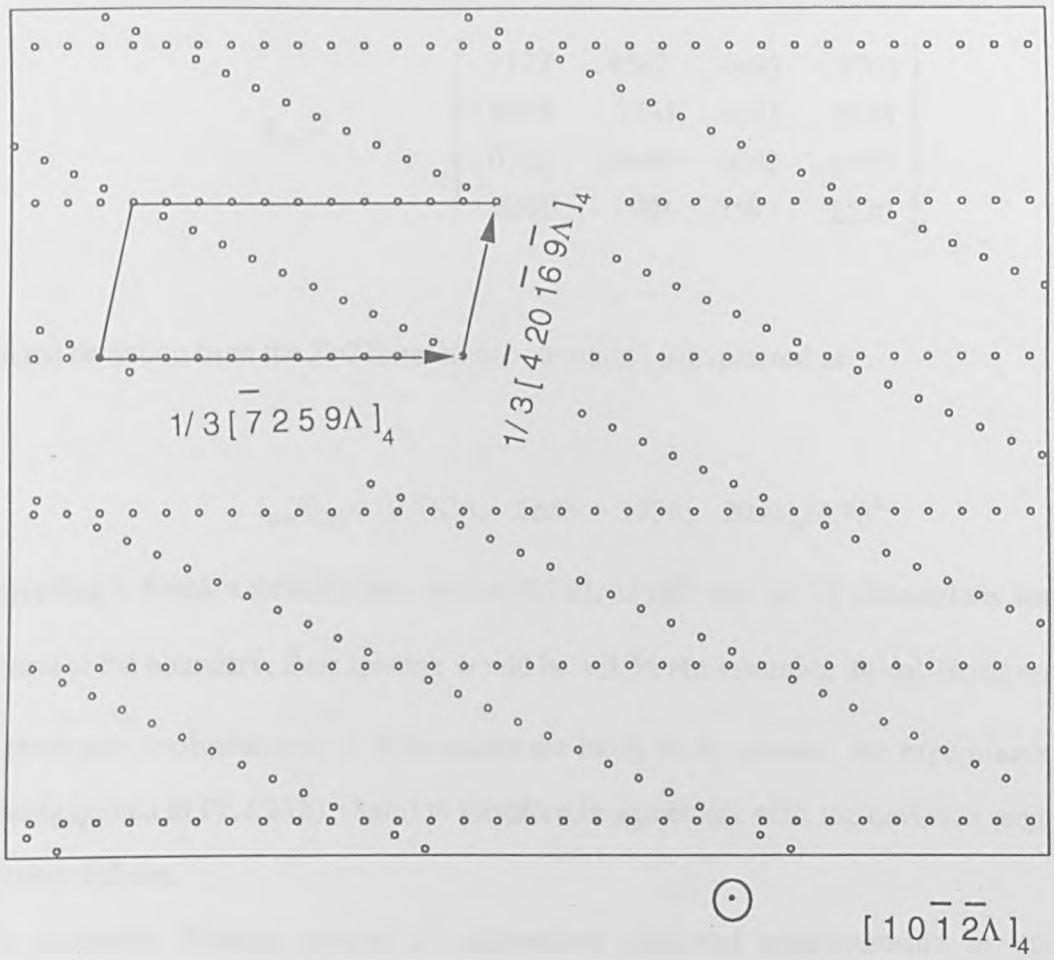

Fig 7.7: Shematic illustration of the Σ=22b dichromatic pattern

$$R_{ccsl} = 1/22 \begin{bmatrix} 3 & 10 & 9 & \frac{-14}{\Lambda} \\ 18 & -6 & 10 & \frac{4}{\Lambda} \\ 1 & 18 & 3 & \frac{10}{\Lambda} \\ \frac{-10}{\Lambda} & \frac{-4}{\Lambda} & \frac{14}{\Lambda} & 4 \end{bmatrix}_4 \qquad (\Lambda = \sqrt{\frac{2}{3}})$$

$$R_{exp}= \begin{bmatrix} .1122 & .4382 & .4495 & -.7702 \\ .8109 & -.2731 & .4621 & .2325 \\ .0768 & .8349 & .0882 & .5377 \\ -.5690 & -.1901 & .7592 & .2520 \end{bmatrix}_4$$

and the deviation from the Σ=22b reference structure , is expressed as

$$r_{dev}/\theta_{dev}= [0.7638; -.5853; -.1736; -.2091]_4/4.78^0.$$

According to Frank's formula (see section II.1.2), if only one set of dislocations was present at the boundary, their spacing would be ≈ 3.56 nm assuming |**b**|=|**a**|. However, as other non-resolvable sets of dislocations are likely to be present, the experimental spacing quoted in IV.2.2 (b) (8nm) is therefore in agreement with the deviation angle calculated above.

The admissible Burgers vectors of dislocations observed experimentally in this boundary were calculated from equation 3.2 and a shorlist of possible candidates can be obtained by following the procedure described in VII.2.2. However, the problem of selecting a specific value for **b** arises, as none of the diffracting conditions used led to the extinction of the contrast displayed by the main set of dislocations. An approach due to Shin and King [9], which uses the "O-lattice" equation to predict the line direction of defects arising at a boundary from a specific **b** and a given misorientation, was then used to try and determine the most likely value for **b** . The "predicted" line direction of the defects was calculated for every **b** given by equation (3.2) using Shin and King's approach, and compared with the line direction determined experimentally. Unfortunately, this approach was unsuccessful, as none of the "predicted" line directions fitted the experimental value indicated. As other authors reported inconsistencies with this approach [10], a geometrical approach developed by Wang [11] and predicting a value for **b** for was preferred. Following this method, values for

b were calculated using equation (3.2) and those closest to that predicted using Wang's approach are given in Table 7.2.

Table 7.2.

t(λ)	t(μ)	**b** =t(λ)-**Pt**(μ)	Angle with **b** given by Wang's method
$1/3[\bar{2}\bar{4}20]_4$	$[\bar{1}10\Lambda]_4$	$[.287;.060;.\overline{348};.185]_4$	19.92°
$1/3[\bar{1}\bar{1}20]_4$	$1/3[\bar{1}\bar{2}13\Lambda]_4$	$[.181;.091;.\overline{272};.074]_4$	12.55°

Again, simulation of the contrast should be used to compare the contrast displayed in each case with that observed experimentally . Not only would it be the best tool to determine the likely value for **b** , but it would also allow the proposition of Σ=22 as the reference structure adopted by this boundary to be confirmed or rejected.

VII.2.4 Analysis of a faceted grain boundary.

The faceted structure exhibited by this boundary is clearly visible on the micrographs presented in section VI.2.3. Two sets of facets were observed and their contours were best imaged using the "2-beam in one grain" condition described in IV.5.1. As mentioned in the previous chapter, no dislocation network was observed, and the present analysis therefore discusses other crystallographic features such as the facet orientations with respect to plausible reference structures. The experimental orientation relationship describing the misorientation between the component grains was found to be $[0.634; -0.161; -0.473; -0.585]_4$ /30.04°, and twelve equivalent descriptions were presented in Table 6.4, section VI.2.3 (b). As for the identification of possible reference structures adopted by the boundaries described earlier, each description was converted into Miller-Bravais indices and compared with the list of coincidences obtained for c/a=1. Following this procedure, description 5 was found to be close to the periodic orientation described by Σ=22c. The deviation from this proposed

reference was calculated as described in V.2.4 and expressed as R_{dev}= [-0.521, 0.291; 0.230; -0.7681]$_4$ / 3.38^0.

In cubic materials exhibiting faceted boundaries, the facet orientations often correspond to short period planes common to both grains . The analysis of the 31.5^0 grain boundary in ZnO described previously suggests that this is also the case in this material. As indicated in chapter VI, the facet orientations were found to be very close to $(\bar{4}731)_{\lambda MB}$ and $(\bar{1}105)_{\lambda MB}$ planes, and on the basis of the above argument, the latter were expected to correspond to specific planes of the proposed reference orientation (Σ=22c). However, this was not found to be the case, and alternative reference structures (CCSL's) for this boundary were sought using different values of c/a . Unfortunately, the facet orientations described earlier could not be associated with specific planes belonging to any of the alternative reference descriptions. This result suggests that the reference structure adopted by this boundary does not correspond to that of a periodic pattern, and emphasizes the difficulty associated with the determination of such structures in materials exhibiting hexagonal symmetry.

REFERENCES

1 Stepensov E.A., USSR Patent N1116100 cL C30B33100, *Bull. Isobretenii*, **36**, p77 (1986)

2 Solov'eva V.I., Bondarenko K.P., Bystrikova I.N., and Kheiser D.M., *Crystallogr.Rep*, **39**, p671 (1994)

3 Howe J.M., *Interfaces in Materials* (J.Wiley, Wiley-Interscience, New York), p309 (1997)

4 Goodhew P.J., in *Grain Boundary Structure and Kinetics* (edited by R.W.Balluffi , ASM, Metals Park, Ohio), p155 (1980)

5 Wolf D., and Merkle K.L., *in Materials Interfaces: Atomic-Level Structure and Properties* (edited by D.Wolf and S.Yip, Chapman and Hall, London), p87 (1992)

6 Smith D.A., *Ultramicroscopy*, **29**, p1 (1989)

7 Bleris G.L., Nouet G., Delavignette P., *Acta Cryst.*, **38**, p550 (1982)

8 Hagege S., Ph.D. thesis, *Universite de Caen* (1985)

9 Shin K., and King A.H., *Mater.Sci.Eng.*, **A113**, p121 (1991)

10 MacLaren I., and Aindow M., *Phil.Mag.Letters*, **76**, 1, p25 (1997)

10 Wang S., Mphil thesis, *University of Birmingham* (1996)

Chapter 8

General Conclusions

VIII - Conclusions

The objective of this work was to investigate the atomic structure of grain boundaries in materials exhibiting hexagonal symmetry. The topological analysis part of this study focused on the characterisation of high-angle grain boundaries in ZnO from high resolution images (HREM). Two boundaries, with misorientations close to those for periodic patterns designated by $\Sigma=31$ and $\Sigma=13$ respectively, were analysed using *the a-posteriori* method developed by Pond [1] and the main results emerging from these investigations are summarised below.

- Both boundaries displayed features characteristic of the special category ; however, some evidence was found in one boundary which did not conform to this model.
- Some regions of the 17.8^0 boundary were found to contain localised dislocations while other regions areas were oriented at the exact $\Sigma=31$ CSL orientation. A complete topological analysis was presented and the characterisation of the defects was found to be consistent with experimental observations.
- The 31.5^0 grain boundary exhibited a faceted structure. The analysis of facet D confirmed the special character of this boundary while facet D presented characteristics which did not conform to this model.
- The presence of an incommensurate segment of interface between periodic regions suggested a local transformation from the special configuration, and a model was proposed for the progressive structural transition between the two singular forms.
- The analysis made in this work is believed to be the first observation of the transition at a grain boundary from a structure in the special category to a more general form.
- The consistency obtained between theoretical predictions and observations demonstrates the usefulness of the topological theory for high resolution characterisation of interfacial defects in complex materials.

Another part of this thesis discussed the structure of high-angle grain boundaries in tungsten carbide (WC), analysed using conventional transmission electron microscopy (CTEM).

- The determination of reference structures is an important aspect in the characterisation of interfacial defects by CTEM, and instances exhibiting special orientations were taken as plausible reference structures in the observed boundaries (e.g. Σ=10).
- Candidate Burgers vectors for the observed defects were proposed, but comparison of these predicted values with the observed contrast was inconclusive and further development of contrast analysis techniques is required for a full analysis.
- Analysis of the faceted interface suggested that it was not associated with the proposed reference (Σ=22c), as the facet orientations did not correspond to periodic planes of this CSL . This emphasizes the difficulty involved in the determination of reference structures in hexagonal materials.
- Identification of the reference configurations adopted by boundaries is currently challenging using the crystallographic approach described in this work, but it is believed that improved image contrast simulation techniques would be beneficial in this regard.

Another aspect of this work dealt with understanding the role played by interfacial line-defects in interfacial processes.

- Several aspects such as defect motion and interaction were considered in a comprehensive analysis. Although a lot of work is required for an in-depth understanding, the analysis provided here represents a good introduction to more complex situations.

- The diffusional flux resulting from defect motion was described by an equation expressed in terms of the Burgers vectors and step heights of the associated line-defects, but also the defects' velocity and the concentration of each atomic species in the two adjacent crystals.
- The framework used to describe the material flux due to defect motion was then employed to derive an expression for the total diffusive fluxes associated with two interacting defects and was illustrated by an example.

[1] Pond R.C., in *Dislocations and properties of real materials*, Ed.M.H.Loretto (Inst.of Metals, London), p71 (1985)

Appendix 1

A.1 Hexagonal Crystal Structures

A.1.1 The HCP Structure

The hexagonal close-packed (hcp) structure consists of layers of closely packed atoms which, following Thompson's notation [1], are stacked in the sequence ABABABAB. The structure is said to be ideally close-packed when the axis ratio c/a =1.633. In most materials, however, c/a is never exactly equal to this value (e.g. c/a=1.588 for titanium and c/a =1.856 for zinc). The most closely packed planes in the ideal hcp structure are the basal planes, and a projection of sites onto this plane is represented schematically in Fig A1.

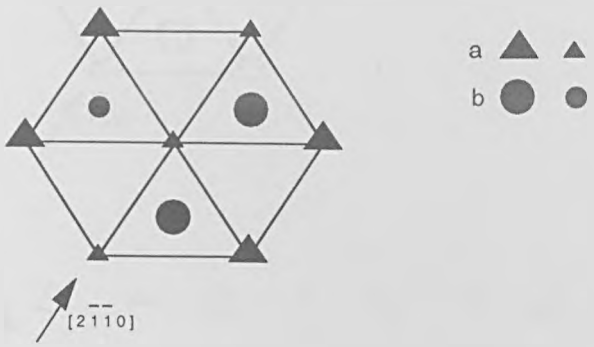

Fig A1: Schematic representation of the projection of atomic sites on the basal plane of the hexagonal structure.

As A and B types of atoms are not identical in the hcp structure, these are represented by circular and triangular symbols respectively. Large and small symbols represent the level of sites projected along [2 $\bar{1}$ $\bar{1}$ 0] direction and the latter projection is depicted in Fig A2.

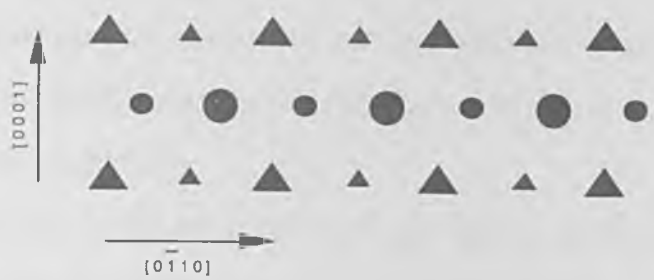

Fig A2: Schematic representation of the projection of sites along the [2 -1 -1 0] direction.

As a comparison, the face centered cubic (fcc) structure has the stacking sequence ABCABCA, and the most densely packed planes are of the type {111}. A schematic projection of sites in an FCC crystal along [111] and [$\bar{1}$10] is shown in Fig A3. Here, triangular, square and circular symbols represent the sequence of close-packed planes and large and small symbols represent the level of sites along [$\bar{1}$10].

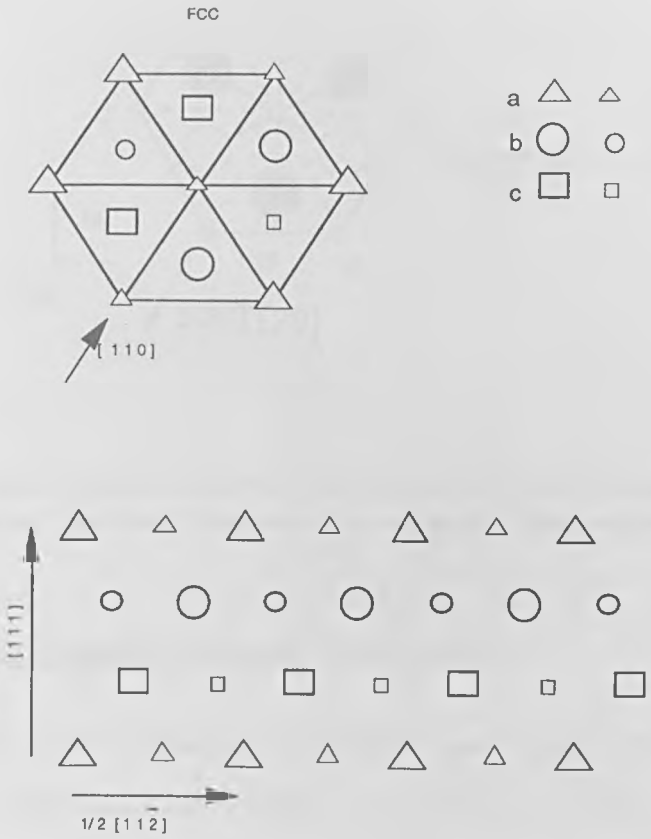

Fig A3: Schematic representation of the projection of atomic sites along a) [111] and b [$\bar{1}$10].

A.1.2 Symmetry

A review of crystallographic calculations and manipulations using both the Miller-Bravais system, and Frank's notation was described in section V.1. In the following, the former is used for simplicity.

A schematic projection of the hcp crystal along the [0001] direction showing type A and B atoms, together with symmetry elements is shown in Fig A.4. As mentioned earlier, A and B atoms are not identical in this structure and are not interrelated by

translations. However, their surroundings are crystallographically equivalent and may be related by c-mirror-glide operations for example (see Fig A4). The set of operations which leave the hcp crystal invariant is represented by the space group $P6_3/mmC$, and some of the principal symmetry elements are indicated in Fig A4.

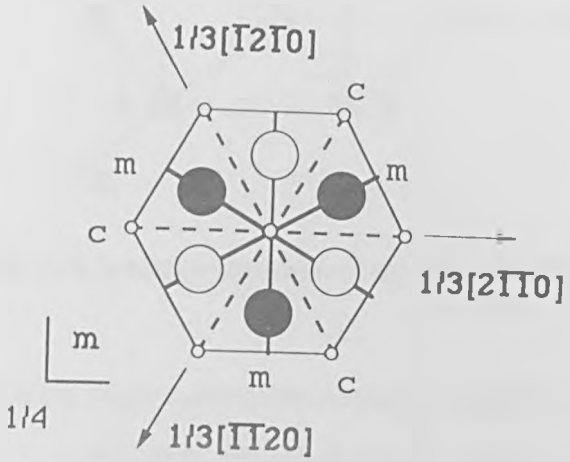

Fig A4: Schematic projection along [0001] of an hcp crystal showing some of the principal symmetry operations. Type A and B type atomic sites are distinguished by different shading.(after Ref2).

A.2 Tungsten Carbide Crystal Structure

Tungsten carbide exhibits hexagonal symmetry (space group $P\bar{6}m2$) with lattice parameters a = 0.2906 nm and c = 0.2837 nm (see Fig A.5). The c/a ratio is very close to 1 (c/a = 0.976), and this aspect has played a significant role in the geometric description of grain boundary structure in this material to date (see section VII.2.1, chapter 7).

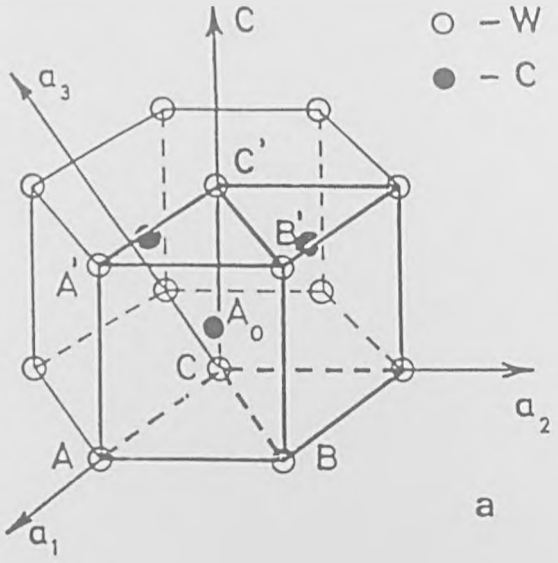

Fig A.5: Schematic illustration of the tungsten carbide unit cell

Tungsten carbide is the major constituent of most cemented carbides, e.g. WC-Co composite materials. In this grade, the cobalt acts as a binder between regularly-shaped prismatic WC grains. This specific microstructure, together with almost perfect wetting, often results in planar grain boundaries, characterised by special orientation relationships between WC crystals [3]. The grade investigated in this work (WC A100) was manufactured by hot sintering of WC powders with no binder phase, resulting in ≈ 5μm WC grains and a microstructure very different to that of WC-Co cemented carbides.

References

1 Thompson N., *Proc.Phys.Soc.* (London) **66B**, 481 (1953)

2 Pond R.C., *Interface Science*, 2, 4 (1995)

3 Benjir M., Ph.D. Thesis, *Universite de Caen* (France), (1991).